

**Interacting magnetic nanoparticles
in discontinuous $\text{Co}_{80}\text{Fe}_{20}/\text{Al}_2\text{O}_3$ multilayers and
in granular FeCl_2 -Fe heterostructures**
*(Wechselwirkende magnetische Nanopartikel
in diskontinuierlichen $\text{Co}_{80}\text{Fe}_{20}/\text{Al}_2\text{O}_3$ Viellagenschichten und
granularen FeCl_2 -Fe Heterostrukturen)*

Von der Fakultät für Naturwissenschaften
der Universität Duisburg-Essen
(Standort Duisburg)
zur Erlangung des akademischen Grades eines
Doktors der Naturwissenschaften (Dr. rer. nat.)
genehmigte Dissertation
von

Sarbeswar Sahoo
aus Fulabadi, Cuttack, Indien

Referent : Prof. Dr. Wolfgang Kleemann
Korreferent : Prof. Dr. Michael Farle
Tag der mündlichen Prüfung : 21. 07. 2003

Abstract

Nanometer scale magnetic materials have gained widespread interest both technologically and scientifically because of the novel effects arising in connection with the reduction of their spatial extension. New experimental techniques have made it possible to prepare and investigate magnetic systems on a nanometer scale. This leads to a growing theoretical interest to understand the properties of nanoscale magnetic systems. Especially, the dynamic behavior of an assembly of magnetic nanoparticles is a subject of considerable current investigation.

The aims of this experimental work can be divided into two parts. First, we investigate the magnetic properties of an ensemble of interacting nanoparticles embedded in an insulating matrix. The system is prepared as a discontinuous-metal-insulator multilayer $[\text{Co}_{80}\text{Fe}_{20}(t_n)/\text{Al}_2\text{O}_3(3\text{nm})]_{10}$, where t_n corresponds to the nominal thickness of CoFe layer. The CoFe forms well-separated and quasi-spherical nanoparticles in the Al_2O_3 matrix. The magnetic properties are investigated by means of *ac*-susceptibility, *dc*-magnetization and relaxation experiments. Dynamic and static criticality studies evidence spin glasslike cooperative freezing of magnetic moments $\mu \approx 10^3 \mu_B$ ("*superspins*") at low temperatures in the nanoparticle system with $t_n = 0.9$ nm. Non-equilibrium collective phenomena such as aging, memory, and rejuvenation are observed in the superspin glass phase. On the other hand, nanoparticle systems with $t_n = 1.3$ and 1.4 nm reveal pertinent features of a superferromagnetic state. This is evidenced by field dependence of *ac*-susceptibility in the $t_n = 1.3$ nm system and by a Cole-Cole analysis of the *ac*-susceptibility in the $t_n = 1.4$ nm system.

Second, we investigate the properties of a granular system consisting of ferromagnetic nanometric Fe particles in an antiferromagnetic FeCl_2 matrix. In this system the nanoparticle-matrix interaction is effective. Apart from direct exchange coupling at the interface between the Fe granules and the Fe^{2+} -ions of FeCl_2 matrix, the dipolar stray-fields of the granules play a key role in the magnetic properties of the system. Giant metamagnetic moments containing Fe granules as nucleation cores are observed under the combined effects of these two mechanisms.

Zusammenfassung

Magnetische Systeme auf der Nanometerskala sind in den letzten Jahrzehnten aufgrund ihrer technologischen sowie wissenschaftlichen Relevanz auf weit verbreitetes Interesse gestoßen. Die Verringerung ihrer räumlichen Ausdehnung birgt neuartige physikalische Effekte. Jüngste experimentelle Entwicklungen haben es möglich gemacht, nanometergroße magnetische Strukturen herzustellen und zu studieren. Dies führte zu einem wachsenden Interesse von Seiten der Theorie, ihre physikalischen Eigenschaften näher zu verstehen. Insbesondere die dynamischen Eigenschaften eines Ensembles von magnetischen Nanopartikeln sind Gegenstand von vielen aktuellen Untersuchungen geworden.

Die Ziele dieser Arbeit können in zwei Teile unterteilt werden. Erstens, untersuchen wir die magnetischen Eigenschaften von Ensembles von wechselwirkenden Nanopartikeln, die in eine isolierende Matrix eingebettet sind. Die Systeme werden als sogenannte diskontinuierliche Metall-Isolator-Vielfachschichten $[\text{Co}_{80}\text{Fe}_{20}(t_n)/\text{Al}_2\text{O}_3(3\text{nm})]_{10}$ hergestellt, wobei t_n der nominellen Dicke einer CoFe-Lage entspricht. Das CoFe bildet getrennte annähernd sphärische Nanopartikel in der Al_2O_3 -Matrix. Die magnetischen Eigenschaften werden mittels ac-Suszeptometrie-, dc-Magnetisierungs- und Relaxations-Messungen studiert. Aufgrund von Untersuchungen der dynamischen sowie statischen Kritikalität findet man kooperatives Spin-Glas-Einfrieren der magnetischen Momente ($\mu = 1000\mu_B$) („*superspins*“) bei niedrigen Temperaturen in den Proben mit $t_n = 0,9$ und $1,0$ nm. Kollektive Nichtgleichgewichts-Phänomene wie „Aging“, „Memory“ und „Rejuvenation“ werden in der Superspin-Glas-Phase beobachtet. Auf der anderen Seite zeigen Nanopartikelsysteme mit $t_n = 1,3$ und $1,4$ nm Eigenschaften eines superferromagnetischen Zustandes. Dies kann aus der Feldabhängigkeit der ac-Suszeptibilität und dem Cole-Cole-Plot der Systeme mit $t_n=1,3$ und $1,4$ nm geschlossen werden.

Zweitens, untersuchen wir die Eigenschaften eines granularen Systems, bestehend aus ferromagnetischen Fe-Nanopartikeln in einer antiferromagnetischen FeCl_2 -Matrix. Hier ist zusätzlich die Wechselwirkung zwischen Partikeln und Matrix relevant. Abgesehen von direkter Austauschkopplung der Oberflächen-Fe-Atome mit den Fe^{2+} -Ionen der Matrix, spielen dipolare Streufelder der Teilchen eine wesentliche Rolle bei den magnetischen Eigenschaften des Systems. Es werden aufgrund dieser beiden Mechanismen sehr große metamagnetische Momente beobachtet, wobei die Fe-Partikel als Nukleationskeime fungieren.

Contents

1. Introduction	1
2. Magnetism of nanoparticles	3
2.1. Generalities	3
2.2. Anisotropies in magnetic nanoparticles	5
2.3. Magnetization reversal: The Stoner-Wohlfarth model	8
2.4. Superparamagnetism and relaxation dynamics of magnetic nanoparticles	12
2.5. Effects of interparticle interactions	15
2.6. Phase diagram of interacting magnetic nanoparticle systems	19
3. Magnetism of spin glasses	21
3.1. Introduction	21
3.2. Order parameter and criticalities	24
3.3. Spin glass models	27
3.3.1. Edwards-Anderson model	27
3.3.2. Sherrington-Kirkpatrick model	28
3.3.3. Hierarchical model	29
3.3.4. Droplet model	31
4. Materials, sample preparation, and experimental techniques	35
4.1. Elemental properties of Fe, $\text{Co}_{80}\text{Fe}_{20}$, and FeCl_2	35
4.2. Preparation of Discontinuous-Metal-Insulator-Multilayers (DMIMs)	38
4.3. Preparation of granular thin films	41
4.4. Transmission electron microscopy	43
4.5. X-ray diffraction and small angle X-ray reflectivity	43

4.6. Superconducting Quantum Interference Device magnetometry	44
5. Properties of $\text{Co}_{80}\text{Fe}_{20}/\text{Al}_2\text{O}_3$ DMIMs	47
5.1. Structural properties	47
5.2. DMIMs in the superspin glass limit	52
5.2.1. High temperature properties: evidence of superparamagnetic features	52
5.2.2. Low temperature properties: individual blocking vs. cooperative freezing	55
5.2.2.1. Dynamic criticality	56
5.2.2.2. Static criticality	59
5.2.2.3. Cole-Cole analysis	62
5.2.3. Non-equilibrium dynamics of the superspin glass state	66
5.2.3.1. Magnetic aging	66
5.2.3.2. Memory imprint and rejuvenation effect	69
5.2.4. Effect of external magnetic field on the superspin glass transition	78
5.2.5. Conclusion	84
5.3. DMIMs in the superferromagnetic limit	85
5.4. Conclusion	98
6. Properties of a granular FeCl_2-Fe heterostructure	99
6.1. Introduction	99
6.2. Structural properties	100
6.3. Magnetic properties	102
6.4. Conclusion	112
7. Summary and Outlook	113
References	115
Acknowledgments	121

Chapter 1

Introduction

Recent research activities in the area of “Nanoscience and Nanotechnology” has been driven by the potential of nanometer scale materials. Firstly, nanoscale materials may exhibit dramatically different and even superior physical and chemical properties over their bulk counterparts making them attractive for applications. Secondly, they have opened new frontiers in basic physics, chemistry, material science, biology, medicine and in many other areas. The rapid advancement is further spurred by the developments in nanofabrication and measurement technology. Among others, nanostructured magnetic materials find special attention [1 – 4]. In particular, modern information technology is in an urgent need of nanostructured magnetic mass memories.

Magnetic materials on nanometer scale exhibit unique properties. Magnetic particles, for example, below a critical size become single-domained as opposed to multi-domain structure of bulk material [5 – 7]. They are ubiquitous in both naturally occurring and manufactured forms. On the one hand, the wide spectrum of applications of these systems is remarkable. They range from magnetic recording media, ferrofluids, magnetic refrigeration, magnetic imaging, to numerous biological and medical uses. On the other hand, the nanometric magnetic particles can be considered as model systems for studies of various basic physical phenomena. Among others, we can mention rotational Brownian motion in ferrofluid, thermally activated processes in multistable systems, mesoscopic quantum phenomena, dipole-dipole interaction effects, and the dependence of the properties of solids on their size.

Today’s magnetic hard disk drives may be viewed as an assembly of magnetic nanoparticles with a few hundreds of nanoparticles per bit. In order to meet the increasing density requirements in magnetic data storage industries, patterned arrays of isolated single-domain particles are recently under consideration. In this connection *single-particle-per-bit* or *quantum recording* has become the goal for the next generation magnetic storage [2,8]. It is aimed at producing single-domain particles with uniform switching properties. This can enhance the storage density from today’s 100 Gbit/inch² to

tens of Tbit/inch². However, there is an ultimate lower limit for the size of the particles, and consequently there is an upper limit for the storage density which is called the superparamagnetic limit. I.e., reducing the size of the particles makes them more susceptible to thermal instabilities, which leads to loss of data. Moreover, with increasing packing density interparticle interactions become more effective and exert sizable effects on the magnetization reversal. Hence, with the miniaturization of magnetic technology the need to understand magnetization on a nanometer length scale is becoming increasingly important.

The present work is intended to provide an insight into the phenomena encountered in an ensemble of ferromagnetic nanoparticles. Particular emphasis is laid on investigating the effects of interparticle interactions on the magnetic properties of an ensemble of superparamagnetic particles dispersed in an insulating matrix. There is strong evidence that these systems may undergo transition into either "superspin glass" or even "superferromagnetic" collective phases. In a second system we have studied the effects of mutual interaction between the ferromagnetic nanoparticles and their antiferromagnetic matrix. It is found that the ferromagnetic nanoparticles can modify the magnetic state of a soft antiferromagnetic matrix surrounding them.

The organization of the thesis is as follows. In Chapter 2 the general properties of fine magnetic particles will be described, and their magnetization reversal and relaxation dynamics will briefly be discussed within the framework of well-established models. In Chapter 3 we briefly discuss the basic concepts of spin glasses and introduce various spin glass models. In Chapter 4 we describe the elemental properties of the materials investigated in this work and various experimental techniques for their preparation and their structural and magnetic characterizations. In Chapter 5 we report on the experimental results obtained on discontinuous-metal-insulator multilayers (DMIMs) $[\text{Co}_{80}\text{Fe}_{20}(t_n)/\text{Al}_2\text{O}_3(3 \text{ nm})]_{10}$, where t_n corresponds to the nominal thickness of $\text{Co}_{80}\text{Fe}_{20}$ layer. New phenomena appearing due to interparticle interactions such as collective state and its non-equilibrium dynamics will be presented. In Chapter 6 experimental results on a granular FeCl_2 -Fe hetrostructure will be reported, where the effects of the nanoparticle-matrix interaction will be demonstrated. Finally, Chapter 7 presents a summary and an outlook.

Chapter 2

Magnetism of nanoparticles

2.1. Generalities

Early experiments on bulk ferromagnetic materials demonstrated that the magnetization, M , measured as a function of the applied field, H , displays hysteresis loops at temperatures below their corresponding Curie temperatures. The first explanation of this unusual behavior was attempted by Pierre Weiss in 1907 [9]. He assumed that ferromagnets are made out of many domains. Each of these domains is magnetized by a certain internal (or “molecular”) field to the saturation value, but the direction of the magnetization vector varies from one domain to the other. The applied magnetic field rotates the magnetization of individual domains into its own direction and when this field is sufficiently large to align all domains, the measured value becomes the saturation one of the sample.

These assumptions were actually valid and sound, and contain the basic understanding of ferromagnetism. Indeed, the existence of domains magnetized in different directions is not even an assumption anymore. These domains, separated by domain walls, have been observed by several techniques and their existence is now an established experimental fact [see the text book by Hubert and Schäfer for details, Ref. 6]. The size and shape of these domains depends on the interplay between the exchange, magnetostatic, and anisotropy energies of the system. Central to the hysteresis loop is the nucleation of domains, motion of domain walls and rotation of the magnetization within the domains. The coercivity mechanism arises both from hindrance to domain wall motion and from magneto-crystalline anisotropy.

The formation of domains is a process driven by the balance between the magnetostatic energy and the domain wall energy. The magnetostatic energy increases proportionally to the volume of the material, while the domain wall energy increases proportionally to the surface area. If the sample size is reduced, this points intuitively to the existence of a critical volume below which the reduction of the magnetostatic energy

becomes less than the minimum energy required to form a domain wall. Consequently, below this size a ferromagnetic material exists as a *single-domain* particle. This means that the particle is in a state of *uniform magnetization*. The constituent spins, at temperatures well below the Curie temperature, rotate in unison. The exchange energy is strong enough to hold all spins tightly parallel to each other and determines the value of the particle magnetic moment, while its direction is determined by the total anisotropy energy. The typical size of a single-domain particle is in the order of a few tens of nanometers depending on the material and contributions from various anisotropy energy terms. For instance, the characteristic radius of a spherical particle below which it exists in a *single-domain* domain state is given by [7] $R_c = 9E_\sigma/\mu_0M_s^2$, where M_s is the bulk saturation magnetization and E_σ the total domain wall energy per unit area. In the case of a Bloch wall $E_\sigma = 2(K/A)^{1/2}$, where K is the anisotropy energy constant and A a parameter representing the exchange energy density. Typical values of R_c are about 15 nm for Fe and 35 nm for Co, while for SmCo_5 it is as large as 750 nm [10]. Typical values of the magnetic moments of single-domain particles are about 10^2 - $10^5\mu_B$ depending on its size and on the material properties, where $\mu_B = e\hbar/2m_e = 9.274\times 10^{-24}\text{Am}^2$ is the Bohr magneton [7].

In principle, single-domain particles must reverse their magnetization by coherent spin rotation. This is a comparatively difficult process, if the particle has a significant magnetic anisotropy. Consequently, single-domain particles are expected have a high coercivity which is the basis of most of their applications. This (non thermal) magnetization reversal mechanism was first studied by Stoner and Wohlfarth [11] and will briefly be discussed in section 2.3. Furthermore, at any finite temperature, thermal activation can overcome the anisotropy energy barrier leading to switching of the particle moment. This solid state relaxation (switching) was first proposed and studied by Néel [12] and later on reexamined by Brown [13]. This model will briefly be discussed in section 2.4. However, larger particles, especially those approaching the critical size for single-domain behavior, reverse their magnetization by an incoherent mode. The two most important incoherent modes are magnetization fanning and curling [5]. In nanowires, even more complicated switching mechanisms like nucleation processes with subsequent domain wall motions occur [14]. In this chapter we concentrate on a description of the reversal mechanism only for single-domain particles. Following this, the effect of interparticle interactions is introduced which in conjunction with the intrinsic

particle properties is mostly responsible in determining the mode of magnetization reversal of an ensemble of single-domain particles.

Single domain particles will in general not be isotropic, but will have anisotropic contributions to their total energy associated with their external shape, the magnetocrystalline structure itself and the imposed stress. First, we briefly discuss the various anisotropy terms.

2.2. Anisotropies in magnetic nanoparticles

2.2.1. Magnetocrystalline anisotropy

Magnetocrystalline anisotropy arises from spin-orbit interaction. The electron orbits are linked to the crystallographic structure and by their interaction with the spins they make the latter prefer to align along well defined crystallographic axes. There are therefore directions in space called *easy axes* in which it is easier to magnetize a given crystal than in other directions called *hard axes*. Among the various types of magnetocrystalline anisotropy depending on the crystal structure, let us consider the uniaxial anisotropy in the case of a hexagonal and the cubic anisotropy in the case of a cubic crystal. The anisotropy energies are written as phenomenological expressions taking into account the crystal symmetry.

For uniaxial symmetry the anisotropy energy can be written as [5,7]

$$E_u = K_1 V \sin^2 \theta + K_2 V \sin^4 \theta + \dots, \quad (2.1)$$

where V is the particle volume, K_1 and K_2 are anisotropy constants, and θ is the angle between the magnetic moment and the symmetry axis. The K 's are dependent on temperature, but at temperatures much lower than the Curie temperature of the material they can be considered as constants. In all known ferromagnetic materials K_2 and other higher order coefficients are negligible in comparison with K_1 and many experiments may be analyzed by using the first term only. For single-domain particles with uniaxial anisotropy most of the calculations are performed also by neglecting K_2 and the magnetocrystalline anisotropy energy is written as

$$E_u = KV \sin^2 \theta, \quad (2.2)$$

where K is usually considered as the uniaxial anisotropy constant. This expression describes two local energy minima at each pole ($\theta = 0$ and π) separated by an equatorial ($\theta = 90$) energy barrier KV .

For cubic symmetry the appropriate expression is [7]

$$E_c = K_1 V (\alpha_1^2 \alpha_2^2 + \alpha_2^2 \alpha_3^2 + \alpha_3^2 \alpha_1^2) + K_2 \alpha_1^2 \alpha_2^2 \alpha_3^2 + \dots, \quad (2.3)$$

where α_1 , α_2 , and α_3 are the direction cosines of the magnetization with respect to the three cubic edges.

2.2.2. Shape anisotropy

The shape anisotropy originates from internal magnetostatic properties. For a uniformly magnetized single domain spherical particle the magnetization direction in zero field is parallel to its easy magnetocrystalline anisotropy axis. It has no shape anisotropy. However, for any non-spherical shape the magnetization direction is strongly influenced by its shape. For example, in the case of a uniformly magnetized ellipsoid of revolution, free magnetic poles are formed at the surfaces. As a result a demagnetizing field is produced in the inside by the potential of these free poles. This leads to an anisotropy energy which is usually written in the form $E_s = \frac{1}{2} (N_x m_x^2 + N_y m_y^2 + N_z m_z^2)$, where m_x , m_y , and m_z are the components of magnetization and N_x , N_y , and N_z are the demagnetization factors relative to the X , Y , and Z axes, respectively. For an ellipsoid of revolution, the demagnetization energy is given by [7,15]

$$E_s = \frac{1}{2} \mu_0 V M_s^2 (N_z \cos^2 \theta + N_x \sin^2 \theta), \quad (2.4)$$

where θ is the angle between the magnetic moment and the polar Z -axis, M_s the saturation magnetization, N_z the demagnetization factor along the polar axis, and $N_x (= N_y)$ the demagnetization factor along the equatorial axis. Equation (2.4) is often written as [15,16]

$$E_s = -\frac{1}{2} \mu_0 V M_s^2 (N_x - N_z) \sin^2 \theta, \quad (2.5)$$

where a constant energy term has been omitted. Since a constant energy term only means a shift in the definition of the zero energy, it does not change the calculations.

Eq. (2.5) can be rewritten as $E_s = K_s V \sin^2 \theta$, where K_s is the shape anisotropy constant. For a prolate ellipsoid, $K_s > 0$ and the effective anisotropy is of *easy axis* type, since there exists two minima of the anisotropy energy along the polar $\pm Z$ axis. For an oblate ellipsoid, $K_s < 0$ and the anisotropy energy has its minimum in the whole equatorial XY plane. In this case the anisotropy is of *easy plane* type.

2.2.3. Strain anisotropy

This is essentially a magnetostrictive effect and is often described by a uniaxial anisotropy energy term [15], $E_{st} = -\frac{3}{2}\lambda\sigma S \cos^2 \theta'$, where λ is the saturation magnetostriction, σ the strain value per unit surface, and θ' the angle between magnetization and the strain tensor axis.

The orientation of the magnetic moment of a nanoparticle is determined by the total free energy. In the absence of an external magnetic field it is the resultant of various anisotropy energies. The uniaxial magnetocrystalline anisotropy energy and magnetostatic (shape anisotropy) energy have different origins. In the special case where the easy crystalline axis of the single domain ellipsoidal particle is parallel to the Z-axis, they have the same θ dependence. Their resultant, from Eqs. (2.2) and (2.5), is given by

$$E_{res} = \left(K - \frac{1}{2}\mu_0 M_s^2 (N_x - N_z) \right) V \sin^2 \theta = K_{eff} V \sin^2 \theta, \quad (2.6)$$

where K_{eff} is an effective anisotropy constant. In the following we shall mainly assume uniaxial anisotropy, of easy-axis type, given by Eq. (2.6).

2.3. Magnetization reversal: The Stoner-Wohlfarth model

The first theoretical description of magnetization reversal in fine particles was developed by Stoner and Wohlfarth (hereafter referred to as S-W) [11], in 1948, in the context of high coercivities observed in hard magnetic materials comprised of elongated single-domain particles. This model demonstrates how the anisotropies present in a system can lead to hysteresis, even in a system in which there are no irreversible effects associated with domain wall pinning. It is particularly interesting to note that, over 50 years after its original development, the S-W model is still extensively used. Although the original study of S-W assumed a shape anisotropy, it is now widely used for the case of uniaxial magnetocrystalline anisotropy. The main assumptions of the model are: (i) coherent rotation of the magnetization of each particle (i.e., no internal degrees of freedom) and (ii) negligible interaction between the particles.

The equilibrium direction of the particle magnetization vector is determined by the direction of the applied magnetic field and the easy anisotropy axis. If a magnetic field H is applied at an angle θ to the easy axis of the uniaxial anisotropy of the particle, the magnetization vector will rotate to an angle ϕ from the field direction. This means that the magnetization vector will be at an angle $\phi - \theta$ from the easy axis. The coordinate system of the S-W model is shown in Fig. 2.1.

The total energy of the system is then given by

$$E = KV \sin^2(\phi - \theta) - \mu H \cos \phi, \quad (2.7)$$

where K is the effective anisotropy constant, V the volume of the particle and the particle moment $\mu = M_s V$, where M_s is the saturation magnetization of the bulk material. S-W preferred to work with the reduced energy [11,16],

$$\eta = \frac{E}{2KV} + \text{constant} = -\frac{\cos 2(\phi - \theta)}{4} - h \cos \phi, \quad (2.8)$$

where $h = \frac{M_s H}{2K}$. For given values of θ and h (or H) the magnetization vector will choose the angle ϕ which minimizes the energy function in Eq. (2.8), i.e., $\partial \eta / \partial \phi = 0$ and $\partial^2 \eta / \partial \phi^2 > 0$.

The first condition, i.e., the equilibrium condition implies

$$\frac{\partial \eta}{\partial \phi} = \frac{1}{2} \sin 2(\phi - \theta) + h \sin \phi = 0. \quad (2.9)$$

The second condition, i.e., the condition for stability limit implies

$$\frac{\partial^2 \eta}{\partial \phi^2} = \cos 2(\phi - \theta) + h \cos \phi > 0. \quad (2.10)$$

On the other hand, if $d^2 \eta / d\phi^2$ is negative, the equilibrium is unstable, and if $d^2 \eta / d\phi^2$ is zero, a condition of stability is just changing to one of instability. Thus, the critical field, h_c , is found by setting $d^2 \eta / d\phi^2 = 0$.

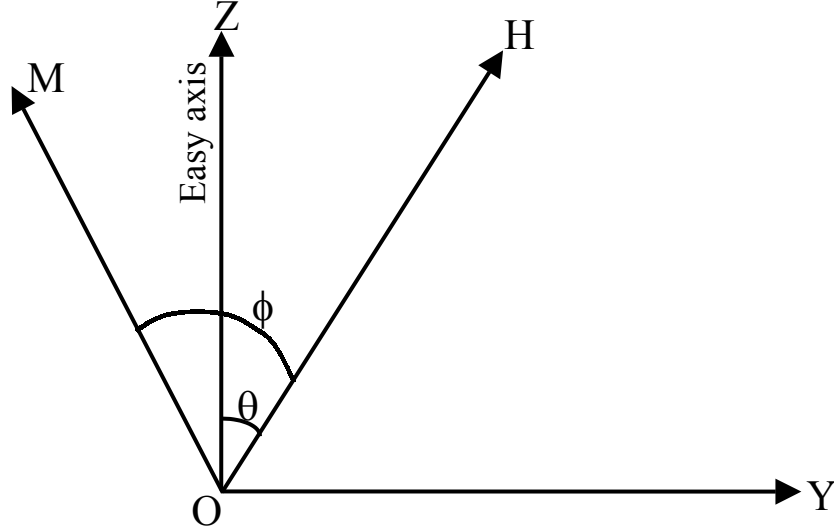


FIG. 2.1. Definition of angles in the Stoner-Wolffarth model.

Due to multi-valued trigonometric functions, Eq. (2.9) has always more than one solution for a given h and θ , and it can happen that more than one of these solutions represent an energy minimum. In order to obtain a unique solution, it is necessary to specify and follow the history of the value of h for each θ . A solution which starts at a particular branch cannot be just allowed to jump into another branch. The jump must be at a field value at which there is no energy barrier between these branches. This important feature is the basis of the *hysteresis*. The component of the magnetization vector M_H along the field H is given by

$$M_H = M_s \cos \phi. \quad (2.11)$$

In order to illustrate how the complete procedure works, let's consider the trivial case $\theta = 0$, i.e., the field is applied along the easy axis. In this case Eqs. (2.9) and (2.10), respectively, will be

$$\frac{d\eta}{d\phi} = (h + \cos\phi)\sin\phi = 0 \quad \text{and} \quad \frac{d^2\eta}{d\phi^2} = \cos 2\phi + h \cos\phi > 0. \quad (2.12)$$

One solution of the first half is $\cos\phi = -h$, which is a valid solution if $|h| < 1$, but it does not fulfill the second half since, $d^2\eta/d\phi^2 = h^2 - 1 < 0$. This solution is an energy *maximum* and has no physical significance. The other solution is

$$\sin\phi = 0 \Rightarrow \phi = 0 \text{ or } \pi. \quad (2.13)$$

In this case the second half of Eq. (2.11) reduces to

$$1 + h\cos\phi > 0. \quad (2.14)$$

The combination of Eqs. (2.13) and (2.14) means that it is necessary to use $\phi = 0$ for $h > -1$, and $\phi = \pi$ for $h < 1$. Furthermore, critical values of the reduced field are $h_c = \pm 1$.

Thus, in the region $|h| < 1$ both $\phi = 0$ and $\phi = \pi$ are valid energy minima. At this point it is necessary to introduce the field history. If we start by applying a large positive h , then reduce it to zero, and increase it in the opposite direction, the physical system remains on the branch of the solution $\phi = 0$ till the field $h_c = -1$ is reached. At this field the solution becomes unstable and the system must jump to another branch, $\phi = \pi$. It should be noted that according to Eq. (2.8) the reduced energy in this case becomes

$$\eta = -\frac{1}{4} - h \cos\phi. \text{ Once } h \text{ passes zero and even becomes slightly negative, the case } \phi = 0$$

has higher energy than that with $\phi = \pi$. However, the magnetization cannot just jump to a lower-energy state, because it is in a local minimum energy state, which means that there is an energy barrier that holds it there. The system is stuck in the higher energy state till the field reaches the value $h_c = -1$, at which the barrier is removed and a jump to a lower state becomes possible. A similar but reverse argument applies to starting from a large negative h , in which case the other branch is held till the field reaches the value $h_c = 1$. Thus, a *rectangular* hysteresis loop is obtained and the coercive field is given by $h_c = 1$, which means $H_c = 2K/M_s$. The way in which the reduced energy η varies with the angular position ϕ of the magnetization vector M for $\theta = 0$ is shown in Fig. 2.2 for various field strengths.

For the case $\theta \neq 0$, Eq. (2.9) has to be solved numerically, but the general behavior is rather similar to the case of $\theta = 0$. The hysteresis loops for a larger choice of values of θ are shown in Fig. 2.3.

Interestingly, also the case $\theta = \pi/2$ does not call for a numerical solution. In this case, Eqs. (2.9) and (2.10), respectively, become

$$(h - \cos\phi)\sin\phi = 0 \quad \text{and} \quad -\cos(2\phi) + h\cos\phi > 0. \quad (2.15)$$

The solution $\cos\phi = h$, which is a valid solution if $|h| < 1$, also fulfills the second half of Eq. (2.15) and is an energy minimum. It yields a magnetization proportional to the field, as in a paramagnet with no hysteresis and with zero coercivity. At $h = 1$ it changes over to the second solution of $\sin\phi = 0$, which is the saturation of $\phi = 0$ or $\phi = \pi$.

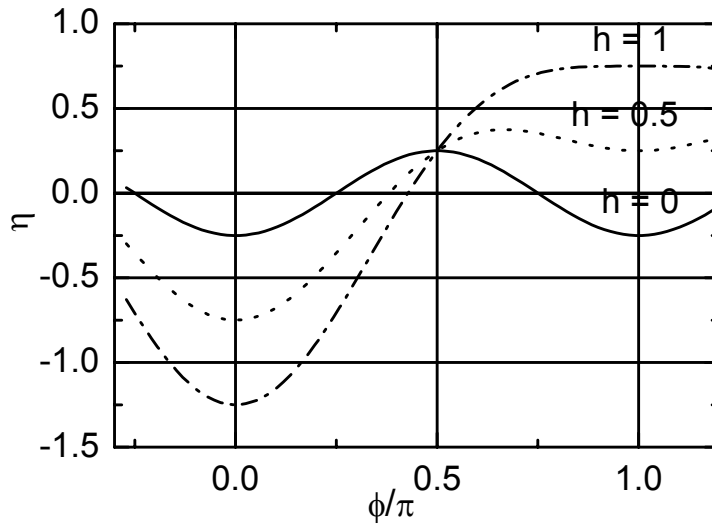


FIG .2.2. Variation of the reduced energy η with ϕ/π of a Stoner-Wohlfarth particle in a field parallel to the easy axis for different values of h as indicated.

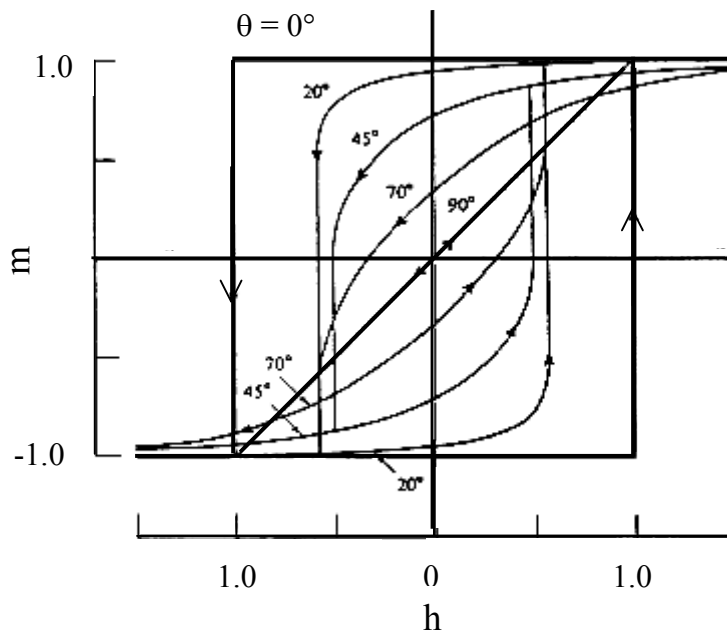


FIG. 2.3. Hysteresis loops in the Stoner-Wohlfarth model for $\theta = 0^\circ$ (bold), 20° , 45° , 70° , and 90° (bold) [11].

2.4. Superparamagnetism and relaxation dynamics of magnetic nanoparticles

As mentioned previously, with decreasing size of a ferromagnetic material a transition occurs from *poly-domain* to *single-domain* state. If we denote the magnetic moment of such a particle by μ and ignore the anisotropy energy and suppose that an assembly of such particles has come to equilibrium at a given temperature T under the influence of an applied magnetic field H , then the mean dipole moment in the field direction is

$$\mu H = \mu L(\zeta), \quad (2.16)$$

where $\zeta = \frac{\mu H}{k_B T}$ and $L(\zeta) = \mu \left(\coth \zeta - \frac{1}{\zeta} \right)$ the Langevin function [17]. The behavior is exactly analogous to the Langevin treatment of paramagnetism. However, the vital difference is that the moment is not that of a single atom but rather of a single domain particle which may be of the order of 10^2 - 10^5 Bohr magnetons (“superspins”). Since extremely large moments and, hence, large susceptibilities are involved the treatment is known as *superparamagnetism* [17].

The S-W model described in the last section explains the non-thermal magnetization reversal process (hysteresis), while in this section we consider the thermal effects on the magnetization reversal process. The assumptions of the S-W model remain preserved. The total energy of a S-W particle is given by Eq. (2.8). In zero external field it reduces to $E = KV \sin^2 \phi$, which has two minima, at $\phi = 0$ and π , separated by an energy barrier KV . At any finite temperature it is possible for the particle moment to escape over the barrier by means of thermal activation. This solid-state relaxation process was first studied by Néel in 1949 [12] and later on reexamined by Brown [13]. Néel suggested that the relaxation rate is given by an Arrhenius law,

$$\frac{1}{\tau} = f_0 \exp\left(-\frac{KV}{k_B T}\right), \quad (2.17)$$

where f_0 is the attempt frequency. The original estimate of Néel was $f_0 \cong \frac{1}{\tau_0} \approx 10^9$ s [12].

f_0 or τ_0 can be associated with the gyromagnetic precession (intra-potential well dynamics) [13]. Brown have shown that τ_0 depends on the material parameters (size and anisotropies), field and even on temperature. From Eq. (2.17), it is important to note that τ depends on V and T so that by varying the volume of the particles or temperature, τ can be made to vary from $\tau_0 \approx 10^{-9}$ s to millions of years.

When a magnetic field is applied along the easy axis, the total energy of the particle will be

$$E = KV \sin^2 \phi - \mu H \cos \phi . \quad (2.18)$$

The function E is plotted vs. ϕ/π in Fig. 2.4 for the case $\mu H = KV$.

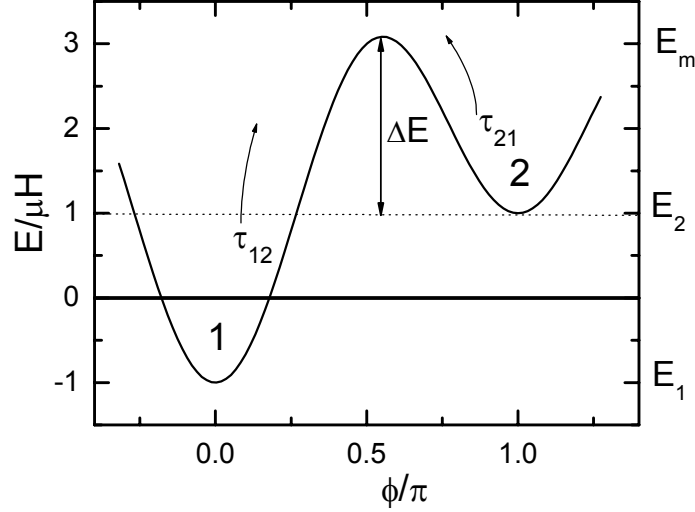


FIG. 2.4. ϕ/π dependence of the energy of a Stoner-Wohlfarth particle for the case $\mu_0 H = KV$ when a field is parallel to the easy axis.

There are still two minima, at $\phi = 0$ and π , whose energies are

$$E_1 = -\mu H \quad \text{and} \quad E_2 = \mu H, \quad (2.19)$$

respectively, with an energy barrier ΔE between them. In thermal equilibrium, the magnetization will lie in one of these minima. The probability of jumping over the barrier from minimum 1 to minimum 2 is a function only of the height of the barrier, $E_m - E_1$, where E_m is the energy at the maximum. Taking the derivative of Eq. (2.18) with respect to ϕ and equating to zero,

$$\frac{\partial E}{\partial \phi} = \sin \phi (2KV \cos \phi + \mu H) = 0. \quad (2.20)$$

The solution $\sin \phi = 0$ leads to two minima whose energies are given by Eq. (2.19). The other solution is at $\cos \phi = -\frac{\mu H}{2KV}$. In this case $\frac{\partial^2 E}{\partial \phi^2} < 0$, hence, the corresponding value of ϕ represents a point of maximum. Substituting this in Eq. (2.18), the energy at the maximum is found to be

$$E_m = KV + \frac{\mu^2 H^2}{4KV} = KV \left[1 + \left(\frac{HM_s}{2K} \right)^2 \right], \quad (2.21)$$

where $M_s = \frac{\mu}{V}$ is the spontaneous magnetization of the particle. Therefore, the rate of jumping over the barrier from minimum 1 to minimum 2 and vice-versa can be written, respectively, as

$$\tau_{12} = \tau_{012} \exp\left(\frac{E_m - E_1}{k_B T}\right) = \tau_{012} \exp\left(\frac{KV}{k_B T} \left(1 + \frac{H}{H_K}\right)^2\right) \quad (2.22)$$

$$\text{and } \tau_{21} = \tau_{021} \exp\left(\frac{E_m - E_2}{k_B T}\right) = \tau_{021} \exp\left(\frac{KV}{k_B T} \left(1 - \frac{H}{H_K}\right)^2\right), \quad (2.23)$$

where $H_K = \frac{2KV}{\mu} = \frac{2K}{M_s}$, and τ_{012} and τ_{021} are in principle two different constants proportional to the inverse curvature at the minimal points. In the particular case $H = 0$ the barrier is the same in either direction and τ_{012} and τ_{021} must be equal and Eqs. (2.22) and (2.23) reduce to Eq. (2.17). Brown [13] pointed out that if the minima are rather narrow and the barrier energy is rather large, it can be expected that τ_{012} and τ_{021} have only weak dependence on T and H . He also pointed out that this is negligible when compared with the dependence in the exponential and only a small error is introduced when they are taken as constants and equal. Brown proposed the following expression (in the case of $H = 0$)

$$f_0 \cong \frac{1}{\tau_0} = \frac{2K\gamma_0}{M_s} \sqrt{\frac{KV}{\pi k_B T}} \quad \text{for } \frac{KV}{k_B T} > 1, \quad (2.24)$$

where γ_0 is the gyromagnetic ratio. For the case when even better accuracy is required, there are several easy-to-use approximations (see the review article by Dormann *et al.*, Ref. [15]).

At any rate, the crucial dependence of the relaxation time on the particle size is in the exponent. Thus, it is necessary to take into account the time scale of the experiment t in order to determine the equilibrium behavior of an ensemble of single domain particles.

If $\tau \gg t$, a condition which is satisfied when $E \gg k_B T$, no change of the magnetization can be observed during the time of the measurement. Thus, almost everything mentioned in this section can be ignored. The only point which may not be ignored is that this stability of magnetization does not necessarily hold at the lowest

energy minimum. If it is brought by some means to the higher minimum of Fig. (2.4), it will stay there, practically for ever, or until it is brought down by an appropriate application of a magnetic field. This leads to hysteresis properties which demonstrate that a lower energy state exists, but it is not accessible because the system is stuck in a higher energy state.

In the other extreme, if $\tau \ll t$, a condition which is satisfied when $E \ll k_B T$, many flips back and forth of the magnetization occur during the time of the experiment. Therefore, in zero applied field the measured average value is zero. The thermal fluctuations have their way and ignore the anisotropy altogether. The behavior is the same as that of the Langevin treatment of paramagnetism, with no hysteresis but with saturation which is reached when all the particles are aligned.

In the case, when $\tau = t$, the temperature $T_b = \frac{KV}{k_B \ln(t/\tau_0)}$ is defined as the blocking

temperature where the above transition occurs. Below T_b the particle is said to be blocked at one of the minima, while above it behaves like a paramagnetic moment.

2.5. Effects of interparticle interactions

In section 2.4, we have reviewed the relaxation phenomenon of magnetic fine particle systems with negligible interparticle interactions. In this situation, the system is in a superparamagnetic (SPM) regime, for which the time evolution of the magnetization is governed by thermal activation over individual energy barriers of each particle within the framework of the Néel-Brown model. When interparticle interactions (for instance, dipolar interactions) are non-negligible the behavior of the system is substantially more complicated and the problem becomes non-trivial. The main types of magnetic interactions that can be present in fine particle assemblies are: (i) dipole-dipole interaction, (ii) tunneling exchange interaction when particles are only at a few nanometers distance apart [18], (iii) direct exchange interaction through the surface of the particles which are in close contact, and (iii) in granular solids, RKKY interaction through a metallic matrix when particles are also metallic, and superexchange interactions when the matrix is insulating. Recently a new kind of interaction mechanism arising from the Casimir effect has been proposed to exist when the magnetic entities are at a few nanometers distance apart [19,20].

These interparticle interactions have profound effects on the dynamical properties of the particle assembly. Firstly, they modify the energy barrier arising from the anisotropy contributions of each particle. In this case individual energy barriers can no longer be considered, only the total energy of the assembly being a relevant magnitude. The reversal of one particle moment may change the energy barriers of the assembly. Secondly, they produce a low temperature collective state which is completely different from individual blocked one. The collective state sometimes shares most of the phenomenology attributed to magnetic glassy behavior [21–23]. However, when interparticle interactions have some degree of coherence, the collective state can form a distinct long range ordered superferromagnetic (SFM) state which is different from the spin glasslike state in many respects [24,25].

Among others, dipolar interactions are always present in a magnetic nanoparticle system and are the most relevant ones. The dipole-dipole energy between two magnetic moments $\vec{\mu}_1$ and $\vec{\mu}_2$ separated by a distance \vec{r} is given by

$$E_{d-d} = \frac{\mu_0}{4\pi r^3} \left[\vec{\mu}_1 \cdot \vec{\mu}_2 - \frac{3}{r^2} (\vec{\mu}_1 \cdot \vec{r})(\vec{\mu}_2 \cdot \vec{r}) \right], \quad (2.25)$$

where $r = |\vec{r}|$. It is long-range and anisotropic in nature. It may favor ferromagnetic or antiferromagnetic alignments of the moments in a system of randomly distributed particles. This can lead to competition of different spin alignments. The nature of the low temperature state of such a frustrated system is similar to that of a spin glass state in many respects. Furthermore, it has recently been predicted that dipolar interactions can give rise to ferromagnetic and antiferromagnetic ground states, respectively, if the particles are positioned in face centered cubic and body centered cubic lattice sites [26].

From an experimental point of view, the problem of interparticle interactions is a complex one. The distribution of various parameters complicates the interpretation of the measurement. On the one hand, it is very cumbersome to disentangle the effects of interactions from the effects of random distributions of shape, size and anisotropy axes. On the other hand, several interactions can simultaneously be present in a sample making it rather difficult to assign the observed properties to specific interactions, if details of sample microstructures are not well known.

The first attempt to introduce interactions in the Néel–Brown model was made by Shtrikmann and Wohlfarth [27] who, by using a mean field approximation, predicted a Vogel–Fulcher law for the relaxation time in the weak interaction limit,

$$\tau = \tau_0 \exp\left[\frac{E}{k_B(T - T_0)}\right], \quad (2.26)$$

where T_0 is an effective temperature which accounts for the interaction effects.

A more general approach was developed by Dormann *et al.* [15]. Taking into account the dipole-dipole interaction the model predicted two magnetic regimes depending on the interaction strength. First, for negligible or very weak interactions, the predictions match the Néel-Brown model of superparamagnetism. Second, for appreciable dipolar interactions the individual energy barriers are modified by its strength and was referred to as superparamagnetic regime modified by interactions. Here an increase of T_b with the strength of the dipolar interactions (e.g., increasing particle concentration or decreasing particle distances) was predicted. The model could correctly reproduce the variation of the blocking temperature, T_b , deduced from *ac*-susceptibility and Mössbauer spectroscopy, as a function of the observation time window of the experiment. However, it could not account for the collective properties observed in many interacting magnetic nanoparticle systems. They were attributed to arise from exchange or superexchange interactions. Later on, Dormann *et al.* [23] studied the magnetic properties of γ -Fe₂O₃ nanoparticle systems of varying strength and evidenced three magnetic regimes, i.e., a pure superparamagnetic regime when the interactions are very weak, a superparamagnetic regime modified by the interactions in which it is still possible to define the energy barrier for a given particle, and a collective regime revealing a true thermodynamic phase transition.

In a third model proposed by Mørup and Tronc [28] for the *weak interaction limit*, the opposite dependence of T_b , viz. decreasing with increasing strength of the interactions was predicted. This behavior was again experimentally confirmed by Mössbauer spectroscopy in the samples of γ -Fe₂O₃ particles [28,29]. In order to untangle the apparent contradiction, Mørup [29] suggested that two magnetic regimes, governed by opposite dependencies of T_b , occur in systems of interacting fine particles. At high temperatures and/or for weak interactions, T_b signals the onset of a blocked state and T_b decreases as the interactions increase. In contrast, at high temperatures and/or for strong interactions, a transition occurs from an SPM state to a collective state which shows most of the features of typical glassy behavior. In this case, T_b is associated with a freezing process and it increases with the interactions. In the last few years, this collective state

and its glassy properties are among the most studied issues of assemblies of strongly interacting nanoparticles [22–24,30,31].

With regard to the high degree of complexity of the problem it seems useful to consider the results of “numerical experiments”. In the following, we will summarize the main conclusions derived from numerical calculations and MC simulations applied to models of interacting particle assemblies. For systems with random orientation of anisotropy axes, a reduction of the coercive field, H_c , with the strength of dipolar interactions was predicted by means of MC simulations [32], a result that was also experimentally confirmed by hysteresis measurements showing a decrease of H_c with particle density [33]. If the particles were not randomly oriented, H_c was predicted to increase or decrease depending on the geometrical arrangement of the particle moments [34]. Therefore, dipolar interactions may increase or decrease the energy barriers involved in the reversal of the particle moments depending on their geometrical disposition.

In granular systems, dipolar and exchange interactions may exist simultaneously. The results of numerical models for this situation indicate that both remanence and H_c increase with increasing exchange coupling when exchange effects are not uniform [35]. On the contrary, when particles are located on a lattice, an increase in the remanence and a decrease of H_c are predicted [36].

Useful fingerprints for characterizing the nature of a glassy system are correlation functions and their relaxational properties. Probably the simplest property to study on a magnetic system is the magnetization and its time dependence after applying a field pulse. Bunde *et al.* [37] studied the influence of dipolar interactions and polydispersivity on the isothermal magnetization relaxation of a random ensemble of magnetic nanoparticles after switching off a saturating external magnetic field. They found that the relaxation of magnetization (i) decays by a stretched exponential law at low concentration, (ii) decays by a power law at intermediate concentration, and (iii) retains a nonvanishing remanent magnetization at very high densities. In this work, results of steps (ii) and (iii) are indicative of a spin glass phase. However, a finite value of the remanent magnetization as observed in step (iii) seems to imply the existence of some long-range ordered state beyond the spin glass state with zero remanence. We are, hence, inclined to observe the realization of the conjectured [25] superferromagnetic domain state. Furthermore, MC simulations of a model very similar to the preceding one [38] concluded that collective behavior governs the dynamics of the system at low temperatures, which was

demonstrated by the occurrence of aging phenomena and a remarkable broadening of the relaxation time distribution as compared to the non-interacting case.

2.6. Phase diagram of interacting magnetic nanoparticles

Based on the discussion in the previous section, a schematic phase diagram for interacting magnetic nanoparticles has been proposed [15]. This is reproduced in Fig. 2.5. Here T_c and T_b are, respectively, the Curie and the blocking temperature of a nanoparticle. The phase diagram should be considered for a given measuring time t_m . For a different t_m , the T_b variation must be shifted upward (shorter t_m) or downward (larger t_m).

As predicted in the Dormann *et al.* [15] model, if T_b increases with the strength of interactions (continuous line), one should observe paramagnetic, superparamagnetic, blocked and collective states with decreasing temperature. In this case the collective state can emerge from a progressive inhomogeneous freezing of the moments without a true thermodynamic transition. However, above a certain value, the interactions can yield a collective state if the line T_{coll} crosses T_b along the T -axis. In this case, the sequence of the states will be paramagnetic, superparamagnetic and collective. The transition from superparamagnetic to a collective state marks a true thermodynamic transition.

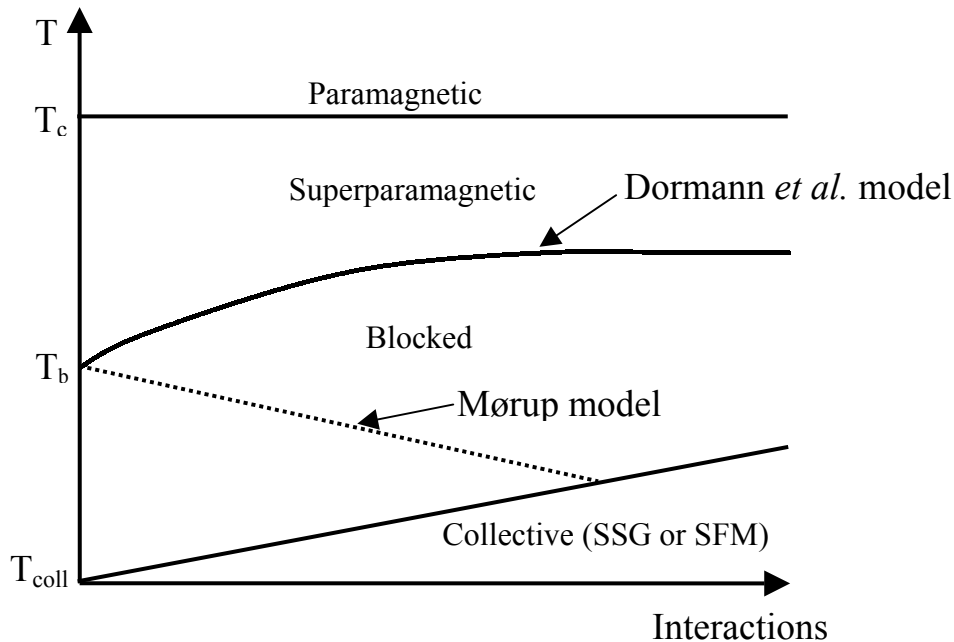


FIG. 2.5. Schematic phase diagram for magnetic nanoparticles with interparticle interactions.

In the opposite case, as predicted in the Mørup [29] model, T_b decreasing with increasing interactions, the observed sequence of states below a critical strength of interactions will be paramagnetic, superparamagnetic, blocked, and collective as in the Dormann *et al.* model. However, above the critical strength the blocked state will be suppressed and a true thermodynamic transition from superparamagnetic to a collective state will occur.

Chapter 3

Magnetism of spin glasses

3.1. Introduction

Magnetic systems exhibit various types of ordering depending on the nature of interaction among the magnetic entities, temperature, and external magnetic field. In order to describe the properties of a magnetic system, Heisenberg in 1928 [39] proposed the following microscopic Hamiltonian

$$\mathcal{H} = - \sum_{\langle ij \rangle} J_{ij} \vec{S}_i \cdot \vec{S}_j - H \sum_{i=1} \vec{S}_i, \quad (3.1)$$

where J_{ij} is the exchange coupling constant between the atomic spins S_i and S_j on sites i and j , respectively. $\langle ij \rangle$ denotes the sum is over the nearest neighbors. The second term is the Zeeman energy which describes the coupling of the system to a magnetic field.

The first term in Eq. (3.1) is responsible for a cooperative behavior and the possibility of a phase transition. If $J_{ij} = J > 0$, parallel alignment of neighboring spins is favorable and if $J_{ij} = J < 0$, anti-parallel alignment is favorable. Accordingly, Eq. (3.1) describes the Hamiltonian for a ferromagnet and an antiferromagnet. For, $J_{ij} = 0$, Eq. (3.1) is the Hamiltonian of a paramagnet, the spins do not interact, there is no cooperative effect and, hence, no phase transition.

However, when J_{ij} is a random variable, one's intuition might suggest that the end result would be something which is completely random and the possibility of a phase transition is questionable. Indeed, such systems do show a phase transition at a particular temperature to a state, while not ordered, is distinctly different from the high temperature disordered state. This magnetic state with mixed interactions, characterized by a random, yet cooperative freezing of spins below a well defined temperature is known as *spin glass* state. Such systems are usually formed by sparsely populating a non-magnetic lattice with random distributions of magnetic atoms, e.g., **AuFe**, **CuMn**, etc.

In order to describe a spin glass system, Edwards and Anderson (EA) in 1975 [40] used the Hamiltonian given by Eq. (3.1) with J_{ij} randomly chosen according to a Gaussian distribution

$$P(J_{ij}) = \frac{1}{\sqrt{2\pi\Delta^2}} \exp\left(-\frac{J_{ij}^2}{2\Delta^2}\right), \quad (3.2)$$

where Δ is the variance. Thus J_{ij} satisfies the criteria $[J_{ij}]_{\text{av}} = 0$ and $[J_{ij}^2]_{\text{av}} = \Delta^2$, where $[\dots]_{\text{av}}$ denotes an average value.

To satisfy the randomness of J_{ij} , there must be *disorder*: site or bond (otherwise the magnetic transition will be of the standard ferromagnetic or anti-ferromagnetic type of long-range order). The combination of the randomness with the competing or mixed interactions causes *frustration*, a unique attribute of the spin glass ground state, which being co-operative in character leads to many interesting properties. These features can be obtained in many systems involving different types of interaction mechanisms.

The noble metal alloys $\text{Cu}_{1-x}\text{Mn}_x$, $\text{Au}_{1-x}\text{Fe}_x$, $x \ll 1$, can be treated to a reasonably fair approximation to satisfy the two basic ingredients: *disorder* and *frustration*. In these systems the host conduction electrons lead to stronger and longer-range indirect-exchange interaction, the famous Ruderman-Kittel-Kasuya-Yoshida (RKKY) interaction [41,42], which has the form

$$J(r) = 6\pi Z J^2 N(E_F) \left[\frac{\sin(2k_F r)}{(2k_F r)^4} - \frac{\cos(2k_F r)}{(2k_F r)^3} \right], \quad (3.3)$$

where Z is the number of host conduction electrons per atom, J the s - d shell exchange constant, $N(E_F)$ the density of states at the Fermi level, k_F the Fermi momentum and r the distance between two magnetic impurities. At large distances, Eq. (3.3) leads to an oscillatory behavior

$$J(r) \propto \frac{\cos(2k_F r)}{r^3}. \quad (3.4)$$

The required factor of *competition* or *frustration* among ferro- and anti-ferromagnetic exchanges is obtained via the oscillating nature of $J(r)$. These spin glasses are referred to as long-range, metallic, canonical or RKKY spin glasses.

The basic criteria, *disorder* and *frustration*, may also be fulfilled in insulating, semi-conducting, or conducting compounds. They can be obtained by diluting into one of the sub-lattices a magnetic species in place of a non-magnetic one. Some prime examples are $\text{Fe}_{1-x}\text{Mg}_x\text{Cl}_2$, $x \leq 0.4$ (an insulator); $\text{Fe}_{1-x}\text{Mn}_x\text{TiO}_3$, $0.1 \leq x \leq 0.5$ (an insulator);

$\text{Eu}_{1-x}\text{Sr}_x\text{S}$, $0.2 \leq x \leq 0.6$ (a semiconductor); $\text{a}-(\text{La}_{1-x}\text{Gd}_x)_{80}\text{Au}_{20}$ (an amorphous metal). In these compounds (super)exchange interaction is responsible for the spin glass dynamics.

Frustration in can be illustrated with some oversimplified sketches as follows.

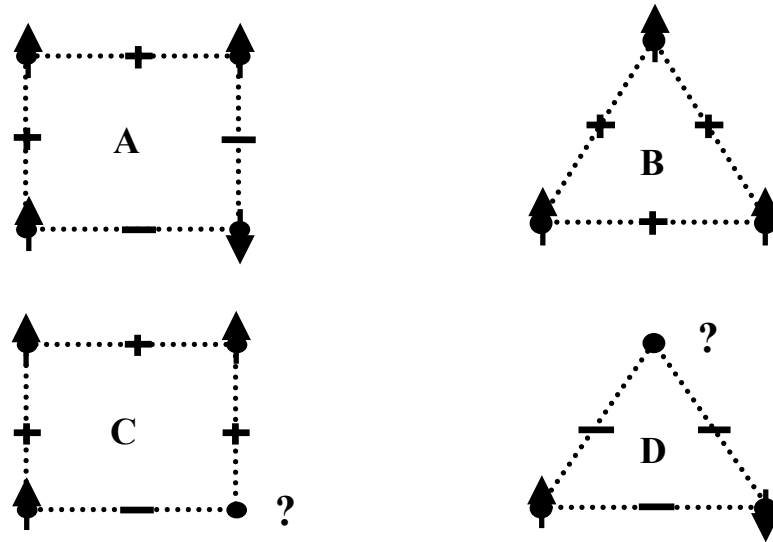


FIG. 3.1. Examples of magnetic frustration on square and triangular lattices. A and B show no frustration, while C and D show frustration associated to the disorder of interaction and to the geometry of the lattice, respectively.

Figure 3.1 illustrates two examples of frustration. Example A represents a square lattice without frustration, since all positive and negative interactions can be satisfied. The spin on the upper left can couple ferromagnetically with the spins on the upper right and lower left, while the spin on the lower right couples antiferromagnetically with them. In example C some frustration appears, since there is not an even number of positive and negative interactions. Here the frustration originates from disorder of interactions. Frustration can also originate from disorder of the lattice and is then referred to as geometrical frustration. Examples B and D represent two possible spin arrangements on a triangular lattice. In B there is no frustration, whereas in its counterpart D the system is geometrically frustrated.

3.2. Order parameter and criticalities

A phase transition occurs when there is a singularity in the free energy or in one of its derivatives and is always associated with critical phenomena. Since a considerable part of this thesis is related to critical phenomena, a brief discussion of some useful concepts of phase transitions including order parameter, critical point exponents, static and dynamic criticality is worthwhile. Excellent texts on the phase transitions exist in the literature, for example see Refs. [43,44]. We specially focus on a detailed description of the concepts related to spin glasses.

It is well known that sharp changes in the physical properties are observed below a critical temperature T_c , where the system undergoes a phase transition. Usually, the phase having the lowest symmetry has the lowest entropy so that one refers to this phase as the “ordered phase”. The transitions from paramagnet to ferromagnet or to antiferromagnet are the classic examples. For each phase, one can define an order parameter which characterizes the spontaneous symmetry breaking by having a zero value for $T > T_c$ and a non-zero value for $T < T_c$. The order parameter for the ferromagnetic phase is the magnetization M , and that for the antiferromagnetic phase is the staggered magnetization, $M = M_A - M_B$, where M_A and M_B are the sub-lattice magnetizations, respectively.

The spins of a spin glass are frozen-in at a random order. Instead of conventional order parameters reflecting spatial correlations, Edwards and Anderson (EA) [40] focussed on time order parameter and proposed the spin glass order parameter (popularly known as EA order parameter) as

$$q = \lim_{t \rightarrow \infty} [\langle S_i(0) \rangle \langle S_i(t) \rangle], \quad (3.5)$$

where $S_i(0)$ and $S_i(t)$ are the magnetic moment configurations at times $t = 0$ and $t = t$, respectively. $\langle \dots \rangle$ denotes thermal averaging and $[\dots]$ the configurational averaging over random bond realizations. For ergodic systems, the local time correlation can be written as

$$q = \lim_{t \rightarrow \infty} [\langle S_i \rangle^2]. \quad (3.6)$$

The EA order parameter has the following temperature dependence

$$q = 0, \quad T > T_g$$

$$q \propto \left(\frac{T_g - T}{T} \right)^\beta = (-\varepsilon)^\beta, \quad T < T_g. \quad (3.7)$$

Static criticality:

Using the fluctuation-response theorem, the order parameter q can be related to the static linear susceptibility of a spin glass [41,45]

$$\begin{aligned}\chi &= \frac{\mu_0}{k_B T} \frac{1}{V} \sum_{ij} [\langle S_i S_j \rangle - \langle S_i \rangle \langle S_j \rangle] \\ &= \frac{\mu_0}{k_B T} \frac{1}{V} \sum_{ij} (S^2 - \langle S_i \rangle^2) \\ &= \chi_0 - \frac{\mu_0}{k_B T} q,\end{aligned}\tag{3.8}$$

where $S = |S_i|$, $\chi_0 = \mu_0 S^2 \rho / k_B T$, and ρ is the number density of magnetic moments. To obtain Eq. (3.8) it is necessary to assume symmetric Gaussian distribution of exchange constants J_{ij} in the Hamiltonian Eq. (3.1) which satisfies $[J_{ij}] = 0$ and $[J_{ij}^2] = J^2$.

Thus, in principle, by measuring the static susceptibility close to the spin glass temperature, T_g , it should be possible to determine the ordering temperature. However, approaching T_g from above, the spin glass dynamics becomes so slow that it is hard to measure the static susceptibility close to T_g and $T \leq T_g$. A static scaling experiment thus needs to be performed at temperatures $T > T_g$.

In a spin glass, the appropriate quantity to study is the order parameter susceptibility, χ_{SG} , which is defined as [41,45]

$$\chi_{SG} \propto \frac{1}{(k_B T)^2} \left[\left(\langle S_i S_j \rangle - \langle S_i \rangle \langle S_j \rangle \right)^2 \right].\tag{3.9}$$

χ_{SG} plays the same role in spin glasses as the linear susceptibility in ferromagnets and diverges as the ordering temperature is approached from above as

$$\chi_{SG} \propto \varepsilon^{-\gamma},\tag{3.10}$$

where γ is the associated critical exponent. Experimentally, χ_{SG} is measurable through the quantity called the ‘‘non-linear susceptibility’’, χ_{nl} in the low field regime [45]. The field induced magnetization M of a spin glass can be expanded in odd powers of external field H as

$$M = \chi_0 H - \chi_3 H^3 + \chi_5 H^5 - \dots,\tag{3.11}$$

where χ_0 is the linear and χ_3, χ_5 etc. are the non-linear susceptibilities of third, fifth, etc. order, respectively. From Eq. (3.10), χ_{nl} can be written as

$$\chi_{nl} = \frac{M}{H} - \chi_0 = -\chi_3 H^2 + \chi_5 H^4 \dots \quad (3.12)$$

Suzuki has suggested the following general scaling law for χ_{nl} of spin glasses [45]

$$\chi_{nl} = \varepsilon^{-\beta} G\left(\frac{H^2}{\varepsilon^{\gamma+\beta}}\right), \quad (3.13)$$

where $G(x)$ is a scaling function. An expansion of $G(x)$ in powers of x yields

$$\chi_{nl} = a_1 \varepsilon^{-\gamma} H^2 + a_2 \varepsilon^{-(2\gamma+\beta)} H^4 + \dots \quad (3.14)$$

Comparing Eq.(3.12) and Eq. (3.14), it is seen that $\chi_3 \propto \varepsilon^{-\gamma}$, $\chi_5 \propto \varepsilon^{-(2\gamma+\beta)}$, and so on.

Dynamic criticality:

Approaching T_g from above, slow dynamics evolves because of the rapid growth of the spin glass correlations. The spatial correlations are described by the correlation function [41]

$$G(r_{ij}) = \left[\langle S_i S_j \rangle - \langle S_i \rangle \langle S_j \rangle \right]^2 \propto r_{ij}^{D-2+n} u(r_{ij}/\xi), \quad (3.15)$$

where r_{ij} is the distance between magnetic moments, D the dimension of the system, n a critical exponent describing the decay of spin-spin correlations at T_g , $u(x)$ a scaling function which decays to zero at length scales $r_{ij} > \xi$, and ξ the correlation length which diverges as $\xi \propto \varepsilon^{-\nu}$ with ν the associated critical exponent.

The relaxation time τ is related to ξ via the exponent z as

$$\tau \propto \xi^\nu \propto \varepsilon^{-z\nu}. \quad (3.16)$$

Experimentally, τ refers to the maximum temperature, T_m , of the *ac*-susceptibility, where $\tau = 1 / 2\pi f$ is connected with the *ac*-frequency f of the experiment.

Dynamic scaling of the *ac*-susceptibility has often been used as supporting evidence for the critical behavior of spin glass transition [46]. The imaginary part of the *ac*-susceptibility, $\chi''(\omega, T)$, measured at various frequencies $f = \omega / 2\pi$ is expected to yield a data collapse onto a single function, $H(\omega, T)$, according to

$$\frac{\chi''(\omega, T)}{\chi_{eq}} = \varepsilon^\beta H(\omega\tau), \quad T > T_g \quad (3.17)$$

where χ_{eq} is the equilibrium susceptibility in the limit $\omega \rightarrow \infty$.

3.3. Spin glass models

In this section we briefly review the development of various spin glass models and their salient features: *advantages* and *disadvantages*.

3.3.1. Edwards-Anderson model

In 1975, Edwards and Anderson (EA) proposed the first model of a spin glass system in a mean field approach [40]. They started with the standard Hamiltonian given by Eq. (3.1) with the exchange coupling, J_{ij} , chosen according to a Gaussian distribution given by Eq. (3.2). EA treated the problem from a general statistical thermodynamic point of view. Here the important assumption is that the system has quenched disorder, i.e., the impurity degrees of freedom are rigidly frozen, meaning that there is no change in the randomness of spin sites (sample structural disorder is frozen-in), only the spin orientation can vary.

A proper treatment of systems with quenched disorder involves averaging the Helmholtz free energy

$$F = -k_B T \ln Z(T, \mathcal{H}), \quad (3.18)$$

where $Z(T, \mathcal{H})$ is the partition function and \mathcal{H} is the Hamiltonian Eq. (1) with J_{ij} the quenched variables. It is easy to observe that this averaging is prohibitively difficult since, to start with, one needs to calculate $\ln Z(T, \mathcal{H})$, which depends on the large set J_{ij} describing the disorder. Thus one would have to do statistical mechanics with a Hamiltonian that contains an infinite number of parameters in the thermodynamic limit and have no translational invariance. Rather than abandoning the idea of averaging over the disorder, one can handle this kind of average by the replica method [40] which uses the following identity

$$\ln Z = \lim_{n \rightarrow 0} \frac{Z^n - 1}{n} \quad (3.19)$$

since for $n \rightarrow 0$, $Z^n = \exp(n \ln Z) = 1 + n \ln Z + \dots$

For positive integer n , one can express Z^n in terms of n identical replicas of the system,

$$\begin{aligned}
Z^n &= \prod_{\alpha=1}^n Z_{\alpha} = Tr \prod_{\alpha=1}^n \exp[\mathcal{H} / k_B T] \\
&= Tr \exp \left[- \sum_{\alpha=1}^n \mathcal{H} / k_B T \right],
\end{aligned} \tag{3.20}$$

where Z_{α} is the partition function of α -th replica. It is relatively easier to carry out the average now and, hence to calculate thermodynamic quantities. The magnetic susceptibility is related to the free energy by

$$\chi(T, H) = \left. \frac{\partial M}{\partial H} \right|_T = - \left. \frac{\partial^2 F}{\partial H^2} \right|_T. \tag{3.21}$$

Using the fluctuation-response theorem, EA predicted a cusp in the susceptibility, $\chi(T)$, at the glass temperature, T_g , which nicely resembles the experimentally measured $\chi(T)$.

Furthermore, the internal energy U ($F = U - TS$) can easily be calculated and hence, the magnetic specific heat, $C_m(T)$, by $C_m = \partial U / \partial T$. EA estimated a cusp at T_g for $C_m(T)$, which contradicts with experiments. This was the main drawback of the EA model and its mean-field approximation. Nevertheless, the clever idea of introducing a time dependent order parameter which formed the basis of subsequent models was a big progress and marks the start of spin glass theory as an active area of theoretical physics.

3.3.2. Sherrington-Kirkpatrick model

Sherrington and Kirkpatrick (SK), in the same year 1975, extended the EA mean-field approximation model [47]. They proposed that the interaction should be considered as infinite-range where every spin couples equally with every other spin. This means that the probability $P(J_{ij})$ is assumed to be the same for all i - j pairs of spins independent of how far they are apart. SK considered an Ising system with a Gaussian distribution

$$P(J_{ij}) = \frac{1}{\sqrt{(2\pi\Delta')^2}} \exp \left[- (J_{ij} - J'_0)^2 / 2\Delta'^2 \right], \tag{3.25}$$

where a mean J'_0 has been included for the possibility of ferromagnetism in the Gaussian function. Introducing the scaling variables $\Delta' = \Delta / N^{1/2}$ and $J'_0 = J_0 / N$, Eq. (3.25) can be rewritten as

$$P(J_{ij}) = \left(\frac{N}{2\pi}\right)^{\frac{1}{2}} \frac{1}{\Delta} \exp\left[-N(J_{ij} - J_0)^2 / 2\Delta^2\right], \quad (3.26)$$

Repeating the calculations of EA, SK arrived at the following result for the susceptibility

$$\chi(T) = \frac{[1 - q(T)]}{k_B T - J_0 [1 - q(T)]}. \quad (3.27)$$

Once again, $\chi(T)$ reproduces a cusp at T_g , confirming to experiments. When the specific heat is calculated as in EA model, there is also a cusp in $C_m(T)$ at T_g . For $T > T_g$, $C_m(T) = N k_B \Delta^2 / 2 (k_B T)^2$, hence a tail in $C_m \propto 1/T^2$ persists at higher temperature. The SK result is in stark contrast to the usual mean-field theory conclusion for a pure system where $C_m = 0$ for $T > T_g$. Furthermore, the entropy S , when determined from the SK model goes to a negative limit, $-Nk_B/2\pi$, which is the most unphysical result of SK model.

3.3.3. Hierarchical model

Using the replica symmetry breaking approach, Parisi in 1980, found an infinite number of solutions of the SK Hamiltonian with infinite-range interactions [48,49]. Each solution can be regarded as an equilibrium state: *metastable* if separated by finite barriers from others and *stable* if separated by infinite barriers. These states are hierarchically organized with respect to their mutual overlaps in a multi-valley landscape at any temperature below T_g . Figure 3.2 shows a schematic picture of the hierarchical organization at different temperatures in the spin glass phase. The various metastable states appear as local minima separated by barriers.

The multi-valley landscape is a function of temperature implying that the metastable states continuously split into new states as the temperature decreases (coarse-grained free energy landscape). Moreover, it is argued that the barriers should increase steeply with decreasing temperature and, possibly, diverge at lower temperatures.

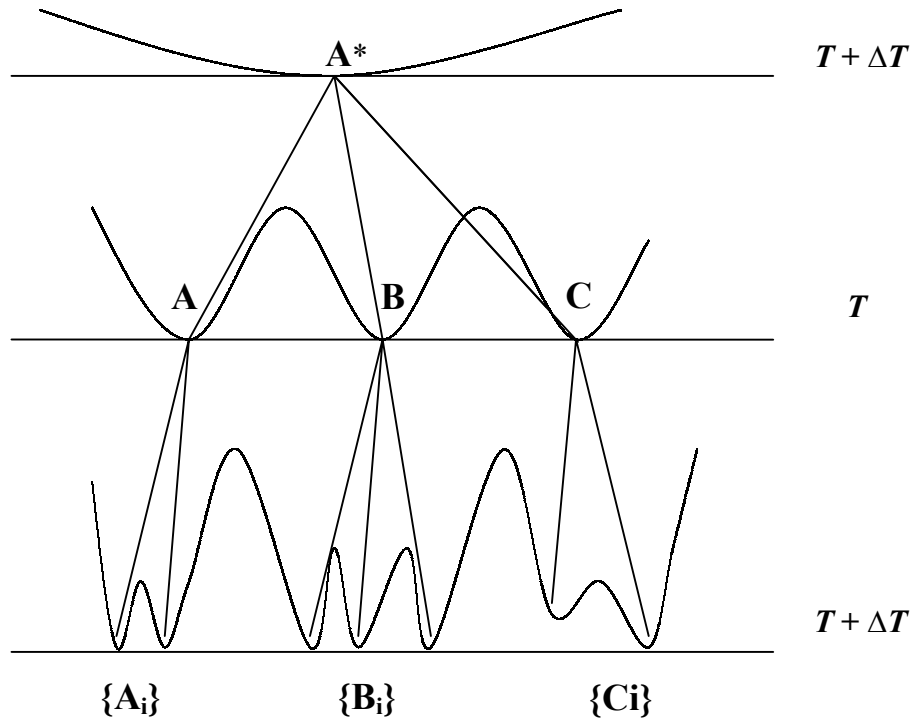


FIG. 3.2. Sketch of the coarse-grained free energy landscape as a function of temperature T . When the temperature decreases from T to $T - \Delta T$, states A , B , and C “give birth” to set of states $\{A_i\}$, $\{B_i\}$, and $\{C_i\}$, seen as sub-valleys, respectively. Conversely, when the temperature is raised from T to $T + \Delta T$, states A , B , and C merge into a single state A^* .

When the system is quenched from above T_g to $T < T_g$, it falls somewhere to one of the states in the complicated landscape defined at T . Suppose that it is in the state A . Upon lowering the temperature to $T - \Delta T$ ($\Delta T \ll T_g$) and following the above argument, new set of states or sub-valleys $\{A_i\}$, $\{B_i\}$, and $\{C_i\}$ are formed. This is seen as splitting of A , B , and C into $\{A_i\}$, $\{B_i\}$, and $\{C_i\}$ in the figure. Conversely, upon raising the temperature to $T + \Delta T$, the states A , B , and C merge into the state A^* .

In a finite-time dynamic experiment the observed properties are characteristics to the state (whether stable or metastable) where the system is trapped and the employed measuring time t (or inverse of frequency in an *ac*-experiment). The characteristic time-scale to surmount a barrier of height E can be taken as $\tau = \tau_0 \exp\left(\frac{E}{k_B T}\right)$. If t is long or short compared to τ to pass statistically many times through all valleys with a significant

thermal weight, average or quasi dynamical effects, respectively, can be expected. Although static experiments can fairly well be interpreted within the hierarchical picture, the very typical non-stationary dynamics (aging and memory) are rather complicated to be interpreted. This fact will be elaborated latter in connection with the interpretation of our experimental results in chapter 5.

3.3.4. Droplet model

Fisher and Huse (FH) proposed a phenomenological theory of the spin glass ordered phase based on a scaling ansatz [50,51]. FH also considered the EA-model Hamiltonian Eq. (3.1) with Ising spins and nearest neighbor interactions on a D -dimensional lattice. Their model is named as *droplet* model because the spin glass phase can be mapped as a distribution of droplets or dynamic domains of correlated spins. In the droplet model it is assumed that there is a two-fold degenerate ground state in zero magnetic field which are related by global spin reversal, say Γ and $\bar{\Gamma}$. The basic idea is to define a droplet as the spontaneous lowest energy excitations of coherently flipped spins. The statics, dynamics, and energetics of the droplets govern the equilibrium properties of the spin glass phase and dominates much of the physics.

The surface of a droplet is very rough, having a non-trivial fractal dimension $D > D_s > (D - 1)$. A droplet of size L scales with the number of spins as L^D . A droplet containing L^D spins, each of them up or down with equal probability, implies a fluctuation in the number of up/down spins of order $L^{D/2}$. Thus a droplet carries a magnetic moment proportional to $L^{D/2}$. In zero field the directions of these moments are symmetrically distributed and the sample net magnetization is zero. In a field, in contrast, this symmetry is broken since droplets having their moments aligned in the field direction are energetically favored, giving rise to a magnetization of the sample. The applied field can be regarded as weak perturbation, if the polarization is linear in field strength and hence, will not affect the properties of the system.

Due to randomness there is a wide distribution of droplet free energies. FH suggested that the free energy cost for creating a droplet of size L scales as

$$F \propto \gamma L^0, \quad (3.28)$$

where γ is the temperature dependent stiffness modulus (can be considered as nucleation

energy) and θ the stiffness exponent. It should be noted that θ cannot be negative since large droplets then cost low energy and a true thermodynamic phase cannot exist. FH derived an upper bound, $0 < \theta \leq (D-1)/2$. Numerical estimates have hitherto given $\theta = 0.2 - 0.5$ for the three dimensional ($3D$) Ising spin glasses [52], hence supporting the existence of a stable spin glass phase in $3D$. The value of θ has recently been determined experimentally [53] for $\text{Fe}_{0.5}\text{Mn}_{0.5}\text{TiO}_3$ and AgMn and amounts to ~ 0.2 and ~ 0.6 , respectively, which agree with the numerical studies.

Another important concept of the droplet picture is the chaotic nature of the spin glass phase: a change of temperature by a finite amount ΔT will rearrange the equilibrium configuration. However, there exists a length scale up to which the states $\Gamma(T)$ and $\Gamma(T + \Delta T)$ cannot be distinguished. This length scale is usually referred to as the overlap length and decreases rapidly with increasing ΔT .

The droplet picture accounts fairly well for the experimentally observed equilibrium and non-equilibrium dynamics of the spin glass phase. Below we give a short review of the concepts involved in the interpretation of our experimental results.

Domain growth and aging

A spin glass system after a quench from infinite temperature to $T < T_g$ is always in a non-equilibrium state. In a two-fold degenerate ground state each spin in the system can be mapped to either $\Gamma(T)$ or $\bar{\Gamma}(T)$, which can be called domains. The relaxation towards the ground state is governed by motion of the domain walls separating the two states. If a spin glass is left unperturbed at a constant temperature, it will lower its free energy via gradual rearrangement of spin configurations by decreasing the domain wall energy. Thus, domains of either type $\Gamma(T)$ and $\bar{\Gamma}(T)$ grow and in the ground state all domain walls are removed. This is a tediously slow process because of the randomness-induced free energy barriers which can only be overcome by thermal activation.

Consider a segment of a domain wall separating the states $\Gamma(T)$ and $\bar{\Gamma}(T)$. A movement of the segment by a distance L can be seen as a flip of a droplet of size L near the domain wall. It is argued that an energy barrier must be surmounted in order to flip a droplet, which is the origin of slow dynamics of the spin glass phase. FH made the assumption that the barrier height for the annihilation of a droplet grows with size as

$$B \propto \Delta(T)L^\psi, \quad (3.29)$$

where $\Delta(T)$ is the temperature dependent free energy scaling factor and Ψ is the barrier exponent, limited by $\theta < \psi \leq (D-1)$. Therefore, growth of a domain by size L requires an energy barrier $F(L) + B(L)$ to be surmounted, a process which at long length scales is dominated by $B(L)$ if $\theta < \psi$. Activated dynamics yields that barriers of height

$$B \propto T \ln\left(\frac{t}{\tau_0}\right) \quad (3.30)$$

will be conquered at the time scale t . For atomic spin glasses the microscopic spin-flip time is $\tau_0 = 10^{-12}$ s [51]. Therefore, the length scale of thermally active droplets becomes of the order [51]

$$L \propto \left(\frac{T \ln\left(\frac{t}{\tau_0}\right)}{\Delta(T)} \right)^{1/\psi}. \quad (3.31)$$

In this way, the creation of a droplet which incorporates a segment of a domain wall may lower the free energy of the system and shifts the position of the domain wall. On the other hand, a droplet which incorporates spins entirely inside a larger domain corresponds to an excitation and will be incorporated into the surrounding ground state. It is clear from this picture that the size of the thermally active droplet excitations sets the smallest possible size of domains which can exist in the sample. Furthermore, an already existing domain can equally well be viewed as an excitation which will be flipped back to the surrounding ground state as soon as the barrier height can be surmounted. All smaller domain structures are with a high probability to be annihilated and incorporated in larger fractal structures. The typical minimum distance between domain walls after a wait time t_w , at a constant temperature becomes

$$R \propto \left(\frac{T \ln\left(\frac{t_w}{\tau_0}\right)}{\Delta(T)} \right)^{1/\psi}. \quad (3.32)$$

By applying a small field after the wait time the magnetization relaxation that follows is governed by polarization of the droplet excitations of size given by Eq. (3.31) and with a typical magnetic moment of order $L^{D/2}$. At time scales $t \ll t_w$, the droplet excitations are small and take place mainly within equilibrated regions. Since only a relatively rare part is excited close to or at the domain walls, quasi-equilibrium response

is observed. Oppositely, non-equilibrium dynamics is probed at $t \gg t_w$, since a large number of the droplet excitations involve domain walls. The crossover between these two regimes is characterized by a maximum in the relaxation rate

$$S = \frac{1}{\mu_0 H} \frac{\partial M(t)}{\partial \ln t}, \quad (3.33)$$

and occurs when the probing time is of the order of the age of the system, i.e., when $\ln(t_w + t) \approx \ln t$ or when $t_w \approx t$. This crossover will be verified in Chapter 5 in connection with our experimental results. This phenomenon is known as “magnetic aging”.

Memory and rejuvenation

In addition to the simple aging experiments discussed above, other system histories provide useful additional information on the nature of the spin glass ordered phase. For example, we consider quenching to a temperature $T_1 < T_g$, waiting for a time t_w , then quenching to $T_2 < T_1$, and finally probing the system upon heating. The main outcome of the experiment is the existence of two seemingly contradictory aspects [54], namely “rejuvenation” upon cooling and “memory” upon heating.

Droplet picture can provide a suggestive and interesting scenario for these effects. In this picture, small temperature changes cause substantial changes of the equilibrium state. The argument goes as follows: the entropy associated to a droplet is the sum of contributions which are random in sign over the surface of the droplet. The entropy of a droplet of size L is $\sim k_B \sqrt{L^{D_s}}$. A subtle conjecture is that the free energy exponent θ satisfies the inequality $\theta < D_s/2$ [51]. Therefore, a small change of temperature can ruin the balance between the energy and entropy. In particular, the ground state becomes unstable at finite temperature change due to gain in entropy and is transformed into new equilibrium state. The rejuvenation effect can be interpreted as a signature of this chaotic change of the equilibrium states upon changing the temperature.

One consequence of the fractal domain picture and the chaotic nature of spin glass phase [55] is that more than one characteristic length scale can exist simultaneously. As already discussed above, the effect of an aging time, t_w , at T_1 is that domains of size $R(T_1, t_w)$ are equilibrated. When changing the temperature, these large scale domain structures remain virtually unaffected and can be retrieved upon heating to T_1 , thus leading to the memory effect. These phenomena will be elaborated in Chapter 5 when interpreting our experimental results.

Chapter 4

Materials, sample preparation, and experimental techniques

This chapter deals with the elemental properties of the materials investigated in the present work and the various experimental techniques employed for their preparation, structural, and magnetic investigation. Two kinds of magnetic systems have been investigated. First, we consider $\text{Co}_{80}\text{Fe}_{20}$ nanoparticles embedded in an alumina (Al_2O_3) matrix prepared as Discontinuous-Metal-Insulator-Multilayers (DMIMs). The DMIMs were prepared by sequential focused ion-beam (FIB) sputtering by the group of Prof. P. P. Freitas at INESC, Lisbon, Portugal. The structural characterization by transmission electron microscopy (TEM) and small angle X-ray reflectivity (SAXR) and magnetic characterization by Superconducting Quantum Interference Device (SQUID) magnetometry were carried at various laboratories of our university. Some of the magnetic relaxation experiments were performed by the use of a home-built SQUID magnetometer in the group Prof. P. Nrodblad at the Ångström Laboratory, Uppsala University, Sweden. Second, we have investigated Fe nanoparticles embedded in an antiferromagnetic FeCl_2 matrix prepared as granular thin films. The system was prepared by coevaporation of FeCl_2 and Fe in an ultra-high vacuum molecular beam epitaxy (MBE) chamber. Its structural characterization by X-ray diffraction (XRD) and magnetic characterization by SQUID magnetometry were performed in our laboratory.

4.1. Elemental properties of Fe, $\text{Co}_{80}\text{Fe}_{20}$, and FeCl_2

Chemically pure metallic Fe crystallizes below $T = 1179$ K in a stable body centered (bcc) structure (α -Fe) with density 7.873 g/cm³ [7]. The atomic radius and the lattice constant amount to 0.126 nm and 0.2866 nm, respectively. The transition metal Fe has an electronic configuration of $3d^6 4s^2$ and is ferromagnetically ordered below its Curie temperature $T_c = 1043$ K [7]. The magnetic moment $\mu = 2.22\mu_B/\text{atom}$ at $T = 0$ K,

corresponding to a saturation magnetization of 1.746 MA/m, is primarily due to that of the 3d electrons.

Co ($\mu = 1.72 \mu_B$) and Fe are miscible over a wide range of relative concentrations [56]. The physical and magnetic properties of CoFe binary alloy series are strongly dependent upon the relative concentration and temperature. They are soft ferromagnetic materials with high spin polarization [57]. The Slater-Pauling curve of $\text{Co}_x\text{Fe}_{100-x}$ alloys shows that the mean magnetic moment per atom increases with increase in Fe concentration and reaches a maximum value at about $\text{Co}_{30}\text{Fe}_{70}$ composition [58]. Collins and Forsyth investigated the magnetic structure of CoFe alloys by neutron diffraction [56]. Their experiments revealed that the moment on the Co atoms remains essentially constant at varying composition in the CoFe binary alloy series, while the moment on Fe atoms increases from $2.22 \mu_B$ for pure Fe to over $3.0 \mu_B$ for equiatomic alloys, and for alloys with > 50 at. % Co. Recent theoretical studies on CoFe clusters corroborate the above experimental fact [59]. Furthermore, the magnetocrystalline anisotropy is minimum at the composition $\text{Co}_{80}\text{Fe}_{20}$ [58]. From these specifications it is rather obvious to choose the composition $\text{Co}_{80}\text{Fe}_{20}$ as a soft magnetic material with high spin polarization.

Figure 4.1 shows the crystalline structure of FeCl_2 . $\underline{x}_r, \underline{y}_r, \underline{z}_r$ indicate the basis vectors of the rhombohedral unit cell. It builds up a lattice of space group symmetry D_{3d}^5 [60]. Hexagonal layers of Fe^{2+} -ions (solid circles) are separated by two layers of Cl^- -ions (open circles). Within the hexagonal layers isotropic FM interaction of the strength $J_1/k_B = 3.9$ K takes place between 6 nearest neighbors. Small negative isotropic exchange, $J_2/k_B = -0.52$ K, gives rise to weak AF coupling between next nearest neighbors within the Fe^{2+} -layers. Additional anisotropic intralayer exchange, $K/k_B = -2.2$ K, is limited to nearest neighbors. The separation of the Fe^{2+} -layers by two Cl^- -layers gives rise to weak AF superexchange interlayer coupling, $J'/k_B = -0.18$ K. In accordance with the large distance $c/3 = 0.585$ nm between adjacent Fe^{2+} -layers, the magnitude of J' is quite small in comparison with the FM intralayer coupling J_1 . Nevertheless, the 3D AF long range order occurring at $T < T_N = 23.7$ K originates from this small AF interlayer exchange.

Table 4.1 summarizes the microscopic parameters which describe the magnetic properties of FeCl_2 . The values of the in-plane interaction constants are based on the analysis of the planar spin wave spectra [61]. The AF inter-layer exchange can be determined from the metamagnetic spin-flip field according to $g\mu_B H = 2z|J'|$, where $z =$

24 is the number of nearest neighbors [62]. Usually, and in accordance with Table 4.1, z is determined by counting the number of geometrical nearest neighbors between adjacent Fe^{2+} -layers. However, on taking into account the equivalence of distinct paths of superexchange, the number of nearest neighbors increases from 6 to 24 for both adjacent layers. This has been accounted for in the value of J' , given in Table 4.1.

$S = 1$	effective spin quantum number
$J_1/k_B = 3.9 \text{ K}$	isotropic in-plane exchange of nearest neighbors
$J_2/k_B = -0.52 \text{ K}$	isotropic in-plane exchange of next nearest neighbors
$K/k_B = -2.2 \text{ K}$	anisotropic in-plane exchange of nearest neighbors
$J'/k_B = -0.18 \text{ K}$	isotropic inter-layer exchange of nearest neighbors
$D/k_B = 9.8 \text{ K}$	single ion anisotropy
$g = 4.1$	effective g-value

TAB. 4.1: Parameters describing the magnetic properties of FeCl_2 .

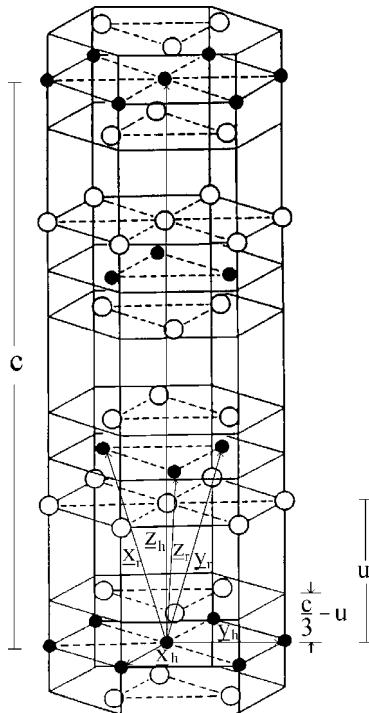


FIG. 4.1. Crystalline structure of FeCl_2 . x_h, y_h, z_h and x_r, y_r, z_r denote the hexagonal and rhombohedral basis vectors of the corresponding unit cells. Solid and open circles represent Fe^{2+} and Cl^- ions, respectively. $c = 1.7536 \text{ nm}$ is the length of the c -axis and $a = 0.3579 \text{ nm}$ is the length of the basis vectors within a hexagonal layer. The distance between adjacent Fe^{2+} - and Cl^- layers reads $c/3 - u$ where $u = 0.2543 c$.

4.2. Preparation of Discontinuous-Metal-Insulator-Multilayers (DMIMs)

All experimental activities of nanomagnetism start with the preparation of magnetic systems on a nanoscale. Currently continuous efforts are being made to synthesize or fabricate magnetic nanoparticles in an efficient and economical way. Preparation routes like chemical synthesis [63,64], sputtering [65–69], thermal deposition [70], and e-beam lithography [71] have been demonstrated to control the size and composition of magnetic nanoparticles and tune their magnetic properties to some good extent.

As already mentioned the DMIMs investigated in this thesis were fabricated by focused ion-beam (FIB) sputtering. The ion-beam sputtering was chosen as a more flexible method for preparation of nanostructures than common magnetron sputtering due to the independent control of the beam parameters, i.e., ion density and kinetic energy of bombarding ions and deposition pressure. Furthermore, it can be used for metallic as well as for insulating targets, especially for high melting-point Al_2O_3 targets. Another important advantage of the ion-beam sputtering lies in the high sample quality, i.e., the deposited materials maintain the stoichiometry and are free from any impurity and oxidation.

The FIB sputtering system is equipped with a load-lock chamber (Nordiko N3000), a 10 cm-diameter deposition gun, and a 25 cm-diameter assist gun as shown in Fig. 4.2. The Xe^+ -ions within plasma created in the deposition gun are accelerated by applying an acceleration voltage of +1450 V and an extraction voltage of –300 V. The heavy Xe^+ ions have the potential to sputter both metallic and insulating targets. The assist gun is used to accelerate a mixed Ar/O_2 beam from a radio-frequency plasma by applying a potential of +30 V to the assist grids. This beam is meant to oxidize a metallic layer to form an oxide film. The design of the system also makes it possible to rotate the targets for sequential deposition during multilayer growth. The thickness of each layer was controlled by the time of deposition from known deposition rates. The chamber base pressure was maintained at 5×10^{-8} Torr, which reduces to 10^{-5} Torr in the presence of Xe^+ -ions during deposition. Details of the sputtering system can be found in Ref. [72].

The DMIMs $[\text{Co}_{80}\text{Fe}_{20}(t_n)/\text{Al}_2\text{O}_3(3\text{nm})]_n$ consists of n number of $\text{CoFe}(t_n)/\text{Al}_2\text{O}_3$ bilayers where t_n corresponds to the nominal thickness of CoFe layer, i.e, the thickness that the CoFe layer would have if it were continuous. As already explained $\text{Co}_{80}\text{Fe}_{20}$ was chosen because it is a soft magnetic material with high spin-polarization [57]. $\text{CoFe}-\text{Al}_2\text{O}_3$ is an ideal system from a structural standpoint since the $\text{CoFe}/\text{Al}_2\text{O}_3$ interfaces are

of high quality and there is no evidence of intermixing of the deposited films at room temperature [73]. Furthermore, the non-wetting effect between CoFe and Al_2O_3 is larger than between, e.g., Co and SiO_2 [66] or CoFe and HfO_2 [67] chosen in other works. This favors the formation of granular CoFe structure during the deposition process. Fig. 4.3 shows a schematic sketch of the cross section of a DMIM system indicating the glass substrate, the Al_2O_3 layers of fixed thickness 3 nm and the CoFe layers of thickness t_n . An attractive feature of the DMIMs is that CoFe particle size increases linearly with t_n while the average inter-particle clearance monotonically decreases. Hence, the inter-particle interaction can be tuned by one parameter, viz., t_n , making it well suited for systematic investigation of magnetic properties.

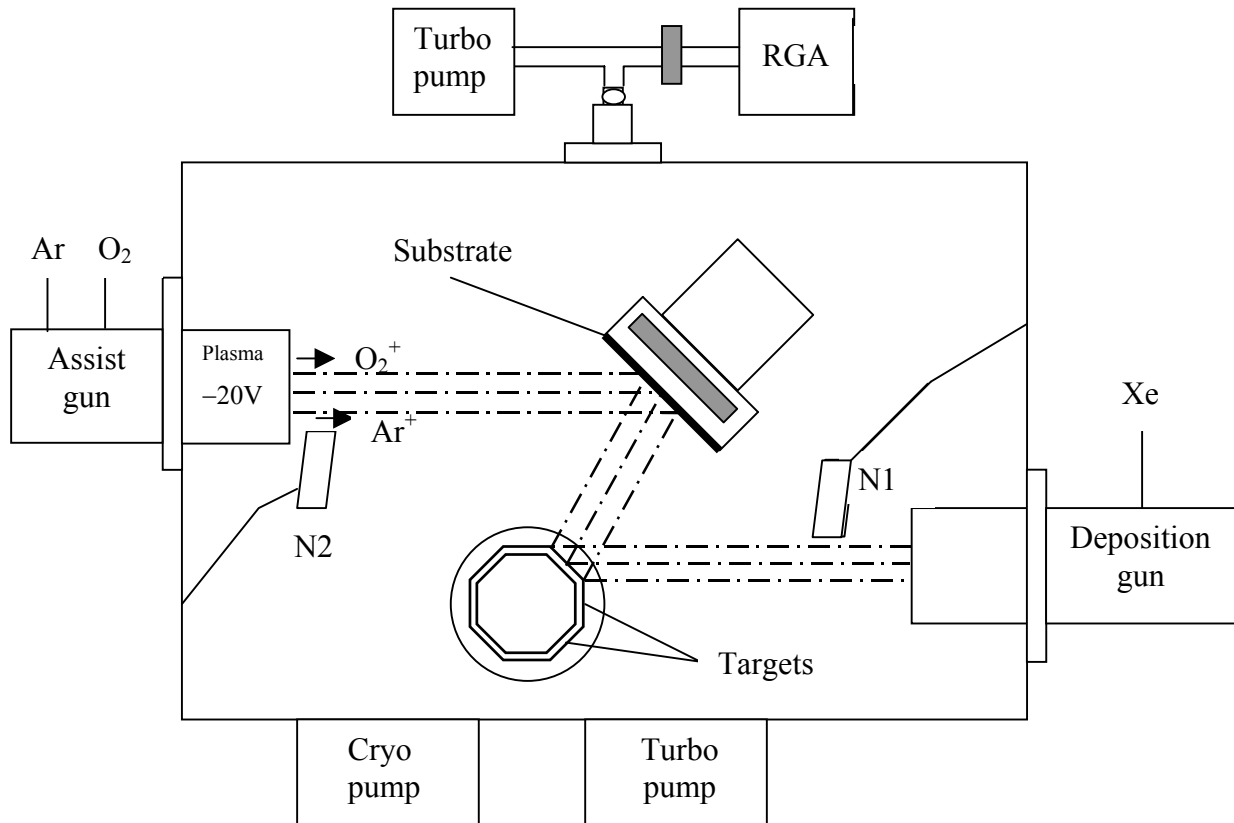


FIG. 4.2. Schematic drawing of the FIB system. A pictorial representation of the plasma during the buffer layer oxidation is shown. N1 and N2 are the neutralizers for the deposition and assist guns, respectively. RGA is the residual gas analyzer.

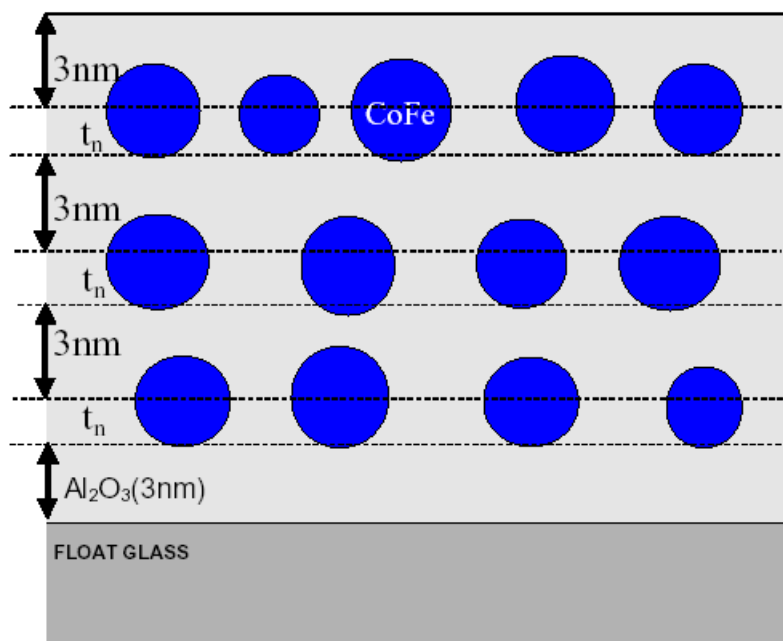


FIG. 4.3. Schematic cross section of a DMIM system consisting of the glass substrate, Al_2O_3 layers (thickness 3 nm) and CoFe layers (nominal thickness t_n) forming quasi-spherical particles.

Samples for magnetic investigation and SAXR were prepared on float glass substrates of 0.4 mm thickness and those for TEM characterization on water soluble KBr substrates during the same run. The thickness of Al_2O_3 layer was kept fixed at 3 nm and that of CoFe is varied in the range $0.5 \leq t_n \leq 1.8$ nm. The top and bottom layers are always Al_2O_3 . The first Al_2O_3 layer (buffer layer) on the glass substrate is formed by depositing an aluminum layer and its subsequent oxidation by a mixed O_2/Ar beam. Subsequent layers of CoFe and Al_2O_3 are alternately sputtered from $\text{Co}_{80}\text{Fe}_{20}$ -alloy and Al_2O_3 targets, respectively. The deposition rates of CoFe and Al_2O_3 were 0.035 and 0.012 nm/s, respectively. The substrates were mounted on a table rotating above the targets and are maintained at 200°C during deposition.

4.3. Preparation of granular FeCl₂-Fe thin films

Molecular beam epitaxy (MBE) allows the growth of high purity thin films in an ultra-high vacuum (UHV) environment. In MBE the materials are thermally evaporated from Knudsen-cells or electron-guns, and condense on a substrate forming a thin film.

Granular FeCl₂-Fe thin films were grown by coevaporation method in a home-built MBE chamber at Duisburg. It consists of two vacuum chambers: an UHV growth chamber and a load-lock. The load-lock is used to transfer samples in and out of the vacuum environment while maintaining the UHV integrity of the other chamber. The pressure in the chamber was measured with an ion-gauge. A mass spectrometer was utilized to maintain the residual gasses and check for leaks. An UHV pressure on the order of 1×10^{-10} mbar was achieved by means of UHV-diffusion pump (with nitrogen trap) and a titanium sublimation pump. The vacuum in the load-lock chamber was generated by a turbo-molecular pump.

A schematic cross-section of the growth chamber is shown in Fig. 4.4. It mainly consists of two plates: a top plate and a bottom plate. The top is equipped with manipulator, sample holder, quartz crystals, and cooling traps. The design of the sample holder makes it possible to cool the substrate down to liquid nitrogen temperature with the help of cooling traps. The substrate temperature can be controlled up to 300° C by means of thermocouple fixed at the sample holder. The bottom plate contains three Knudsen-cells and an e-gun. In order to achieve coevaporation a shutter with two openings was positioned in front of Knudsen-cells to allow the flux of materials reaching the substrate.

The sample investigated in this study was prepared by coevaporation of FeCl₂ and Fe on a sapphire (11 $\bar{2}$ 0) substrate. Prior to the growth process a base pressure of 1×10^{-10} mbar was maintained. After rinsing in acetone the sapphire substrate was preheated to 300° C for 1 hour in order to degas it and then cooled to and maintained at liquid N₂ temperature during the evaporation processes. As a result FeCl₂ becomes amorphous, which warrants tight embedding of the Fe particles during the growth. Upon room temperature annealing FeCl₂ eventually recrystallizes and recovers its original bulk properties [74].

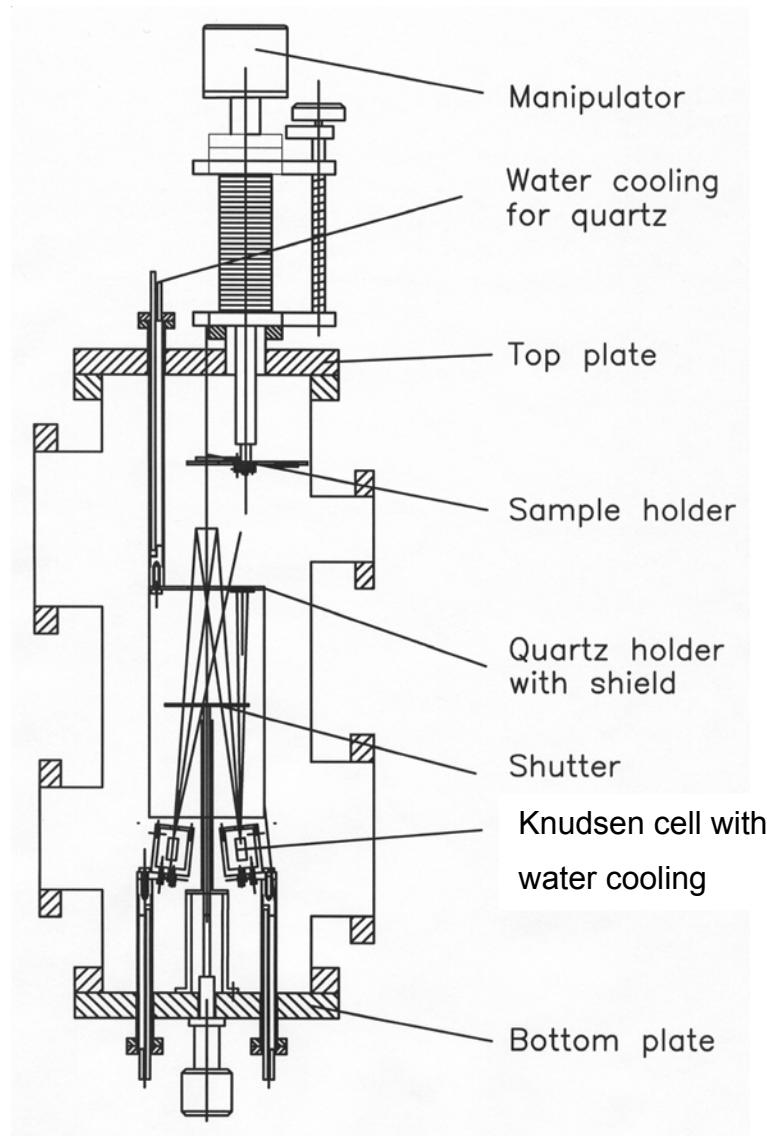


FIG. 4. 4. A schematic cross-section of the MBE growth chamber.

The materials were evaporated from different Knudsen cells, while their thicknesses were controlled by calibrated quartz oscillators. The growth rates of FeCl_2 and Fe were 0.1 and 0.04 nm/s, respectively. The pressure during deposition was better than 1×10^{-7} mbar. To ensure that Fe particles are completely embedded in a textured FeCl_2 matrix, first of all a 200 nm layer of FeCl_2 was deposited on the substrate followed by coevaporation of FeCl_2 and Fe up to a thickness of 500 nm. The sample was protected with a 50 nm thick gold capping layer. In order to avoid the formation of FeAu alloylike nanoparticles, the gold layer was deposited after completely covering the Fe and FeCl_2 mixture with a continuous 200 nm thick layer of FeCl_2 .

4.4. Transmission electron microscopy

A transmission electron microscope (TEM) yields information on the morphology, composition, and crystallography of objects on a very fine scale. In a conventional TEM a thin specimen is irradiated with a beam of highly energetic electrons. The transmitted electron intensity distribution is transformed into an image yielding a morphology of the specimen. More technical details of typical TEMs and their operation can be found in Ref. [75].

The structural properties of DMIMs were investigated by transmission electron microscopy performed on a Philips CM 12 (in collaboration with S. Stappert and G. Dumpich, Experimentalphysik, Universität Duisburg-Essen). The TEM has the following specifications:

Electron gun = LaB₆ rods

Electron energy = 120 keV

Condenser (focusing) system = twin lens arrangement

Point resolution = 0.25 nm

Magnification range = 2650 – 660,000 x

The TEM is attached with an energy-dispersive X-ray (EDX) Si detector (Oxford). The technique is based on the detection of characteristic X-ray peaks that are generated when an energetic electron beam interacts with the specimen. Each element produces characteristic X-rays that can be used to identify the presence of that element in the region being examined. Comparison of the relative intensities of X-ray peaks are then used to determine the relative concentrations of each element in the specimen. Elements with an atomic number less than that of carbon ($Z = 5$) are generally not detectable.

4.5. X-ray diffraction and small angle X-ray reflectivity

The X-ray diffraction intensity was measured in the $\theta - 2\theta$ configuration with a Philips PW1730 X-ray powder diffraction system equipped with a Cu-anode X-ray tube and a graphite monochromator.

If the Bragg condition is satisfied, constructive interference will occur and a peak in the diffraction intensity versus θ will appear. Information about the crystal orientation, lattice constant, layer thickness, and layer roughness can be obtained by analyzing the intensity peaks in the $\theta - 2\theta$ scan [76]. For the characterization of thin films and multilayers, X-ray reflectivity measurements under grazing incidence are performed.

4.6. Superconductivity Quantum Interference Device Magnetometry

A Superconducting Quantum Interference Device, abbreviated by SQUID, is a sensor of magnetic flux. With suitable input circuitry it is used for measurements of magnetic field gradient, magnetic susceptibility, voltage, current, etc. SQUIDs are made from conventional superconductors such as Niobium and operate at liquid helium temperature. With the advent of high T_c superconducting materials such as YBaCu_3O_7 (YBCO) their application is now being realized also at liquid nitrogen temperature.

The operating principles of SQUIDs combine the properties of Josephson weak-links or junctions with the phenomenon of flux quantization. The fundamentals of SQUID magnetometers and their technical conversion to commercial instruments can be found in Refs. [77,78].

The measurements of this work have been performed by the use of two SQUID magnetometers. On the one hand the static magnetization and *ac*-susceptibility measurements were carried out on our own commercial SQUID magnetometer (Quantum design, MPMS – 5S) [79]. On the other hand the relaxation experiments were performed on a home-built SQUID magnetometer [80] at the Ångström Laboratory, Uppsala University, Sweden. In both devices the superconducting ring contains one weak link exploiting the so-called *dc* Josephson effect.

In general, two different principles can be employed for measuring the magnetization of a sample: (i) the absolute magnetization of a sample can be measured by moving the sample through the pick-up coils and analyzing the magnitude of the output of the SQUID electronics. (ii) the magnetization can be measured by keeping the centered sample in one of the coils of the gradiometer. When the magnetization changes, e.g., by changing the temperature, the differential magnetization is obtained as the output of the SQUID electronics. Below we give short technical descriptions and system specifications of both magnetometers.

Commercial SQUID (MPMS – 5S, Quantum Design)

Figure 4.5 depicts some elements of this SQUID magnetometer. The main parts are: superconducting magnet, pick-up coils, *ac* coils, probe head, sample holder, and electromagnetic shielding. In a magnetization measurement it utilizes the above mentioned first principle. The sample space is magnetically insulated with concentric cans of μ -metal. In addition, the residual magnetic field at the sample position can further

be reduced by the help of the Ultra-Low Field (ULF) Option [81]. The lowest residual field achieved is in the range of 1 mG or 0.1 μ T.

The temperature stability of the magnetometer is better than 50 mK in the available temperature range between 1.9 and 400 K. A superconducting coil makes the magnetic field strength possible up to 5 T. The homogeneity of the field decreases with increasing distance from the center of the coil. The length of the coil over which a sample is scanned during a measurement is 4 cm. At the edges the deviation from the nominal field strength value amounts to typically 0.01 %. The magnet works in persistent mode during measurements.

The absolute sensitivity of the magnetometer is defined by the minimum measurable magnetic moment. It amounts to 10^{-11} Am² or 10^{-8} emu at the maximum field of 5 T. The field dependence of the sensitivity is a consequence of the remaining flux (linking) of the field put on into the gradiometer arrangement. The differential sensitivity is defined by the minimum resolvable change of a magnetic moment. It is likewise field dependent and amounts to 5×10^{-10} Am² or 5×10^{-7} emu at the maximum field strength of 5 T.

The device is equipped with alternating field options essential for ac-susceptibility measurements. The alternating field is available within a calibrated frequency range from 0.01 to 10^3 Hz. Its amplitude can be varied between 10^{-3} G and 4 G.

Home-built SQUID at Uppsala

This SQUID magnetometer system is designed for temperature and time dependent measurements employing the differential method. A complete description of the magnetometer can be found in Ref. [80]. There are few advantages of the magnetometer. A temperature resolution of 5 – 10 μ K can be achieved by means of a proportional-integrating-differentiating (PID) controller. The PID adjusts the temperature of the thermometer for zero output from a lock-in amplifier by supplying an adequate amount of power to a Manganin heater on the sample holder.

For magnetization relaxation measurements, it allows acquisition of data starting about 0.3 s after the field switch. The time constant of the dc-magnet is short (50 μ s), thus yielding a well defined time zero, $t = 0$, with respect to which the data collection time is counted. The data are collected at logarithmically spaced time intervals. The

magnetometer allows a reliable magnetization relaxation measurement starting from $t = 0.3$ s up to 10^6 s covering more than six decades in time in one experiment.

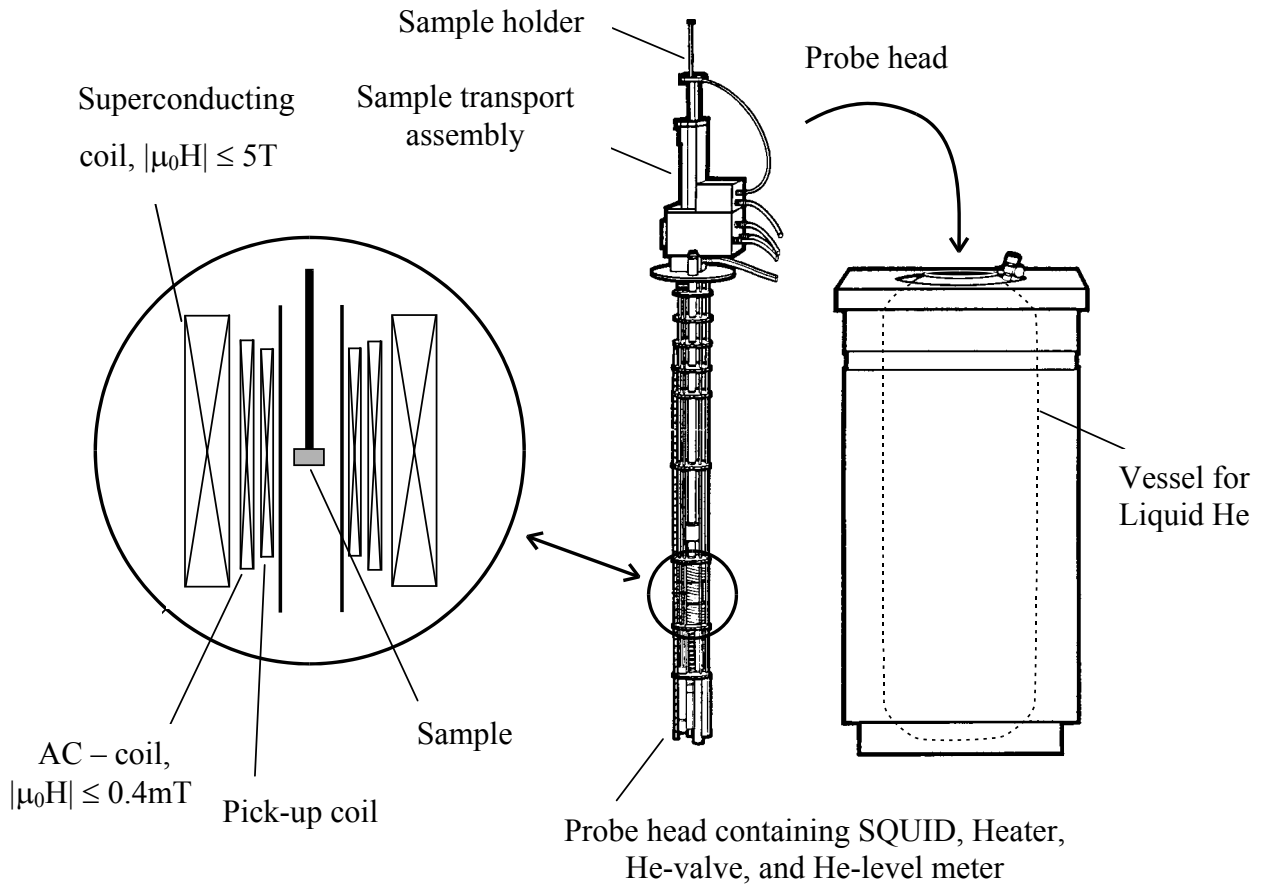


FIG. 4.5. Pictorial representation of the commercial SQUID-magnetometer (MPMS – 5S, Quantum Design). Right: Helium container of ca. 52 liter capacity into which the probe head is immersed. Left: a magnified part of sample measuring region and solenoid magnet.

Chapter 5

Properties of discontinuous $\text{Co}_{80}\text{Fe}_{20}/\text{Al}_2\text{O}_3$ multilayers

The structural and magnetic properties of discontinuous-metal-insulator-multilayers (DMIMs) $[\text{Co}_{80}\text{Fe}_{20}(t_n)/\text{Al}_2\text{O}_3(3\text{nm})]_{10}$ are strongly dependent on the nominal thickness t_n of the magnetic CoFe layer. Structural investigation reveals that the average size of CoFe nanoparticles increases approximately linearly with increasing t_n , while the average clearance between the particles monotonically decreases. As a consequence, the inter-particle interaction is expected to increase with increasing t_n . TEM studies as described in section 5.1 show that at $t_n = 0.9$ nm the DMIM system consists of an assembly of randomly distributed, quasi-spherical nanoparticles with an average diameter, $d \approx 3$ nm. Moreover, the distance between the centers of nearest neighbor particles (hereafter referred to as inter-particle distance) is almost constant and amounts approximately to 6 nm. This system can be considered as a model system to investigate the effects of interparticle interactions on the dynamics of the particle assembly. In section 5.2, it will be shown that this DMIM system remarkably reveals a magnetic phase transition from high temperature superparamagnetic (SPM) state to low temperature superspin glass (SSG) state below a well-defined glass temperature T_g . The glassy dynamics of the low temperature phase is then complemented by the observation of various non-equilibrium properties such as magnetic aging, memory-imprinting, and rejuvenation. This system is denoted as DMIMs in the SSG limit. On the other hand, DMIMs with $t_n=1.3$ and 1.4 nm revealing the features of a superferromagnetic (SFM) state is denoted as DMIMs in the SFM limit and will briefly be discussed in section 5.3.

5.1. Structural properties

The structural properties of DMIMs are investigated by transmission electron microscopy performed on a Philips CM2 whose point resolution is 0.25 nm at 120 keV. In-plane TEM

images are obtained on single CoFe layers sandwiched between Al₂O₃ layers. As mentioned in Chapter 4 these CoFe/Al₂O₃ bilayers are deposited on water soluble KBr substrates. After dissolving in water the films are collected on circular Cu grids of diameter 3.05 mm. One of these grids is placed on the slide of the microscope and various regions are imaged under different magnifications. Observations are made on two to three similar grids, and comparison of images at a constant magnification revealed very similar morphology.

The micrographs in Fig 5.1(a) and (b) were obtained on a Al₂O₃(3nm)/CoFe($t_n = 0.9\text{nm}$)/Al₂O₃ (3nm) sample at magnifications of 2.3×10^5 and 3.8×10^5 , respectively. From these plane-view micrographs it is observed that, at this nominal thickness, the CoFe forms well separated, quasi-spherical and nearly mono-disperse particles. It is well known that the morphology of ultrathin films largely depends on the balance of the free surface energies of substrate, overlayer and interface. The formation of isolated particles in our case indicates a Vollmer-Weber-type growth mode where the deposits tend to nucleate three-dimensional dots, leaving the substrate exposed at lowest energy. The same kind of growth mechanism has also been observed in Co/Al₂O₃ [65, 68] and Co/SiO₂ multilayers [66].

It is further noticed that the granules tend to occupy the sites of hexagons as shown by some sketches in the micrograph (b), thus forming quasi-self-organized structures of a triangular lattice. A close examination of the micrographs indicates that the inter-particle clearance is almost constant and amounts approximately to 3 nm. Furthermore, comparison with transmission electron microscopy studies on a sample with $t_n = 1.3$ nm [69] reveals that the average particle size grows approximately linearly with t_n , while their average clearance monotonically decreases. In accordance with previously observed electronic transport properties, a transition from tunneling to ohmic conductance, percolation is expected to occur at $t_n = 1.8$ nm [69].

Statistics on the size distribution of the particle assembly was obtained by the help of Global-Lab image software. For this purpose the areas of 1051 particles were collected under different sections of the micrographs 5.1 (a) and (b). The areas are then used to calculate the corresponding circular diameters. The histogram in Fig. 5.2 (b) displays the number of particles vs. diameter. It is found that most of the particles are of 3 nm in diameter. The particle size distribution is well described by a Gaussian

distribution, $f(d)dd = \frac{1}{\sqrt{2\pi}\sigma_d} \exp\left[-(d-d_m)^2/2\sigma_d^2\right]dd$, with a mean diameter $d_m \approx$

2.8 nm within a Gaussian distribution width of $\sigma_d = 0.95$ nm.

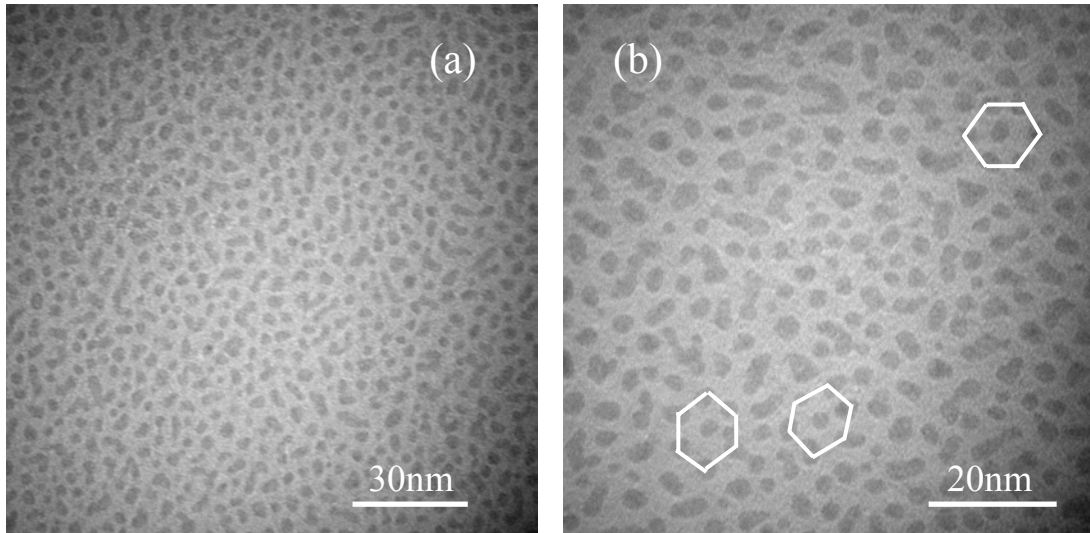


FIG. 5.1. TEM top-view micrographs of a CoFe(0.9nm)/Al₂O₃(3nm) bilayer at magnifications of 2.3×10^5 (a) and 3.8×10^5 (b), respectively.

The elemental composition of the DMIMs was verified by analyzing the energy dispersive X-ray (EDX) spectrum obtained during transmission electron microscopy. The EDX spectrometer is equipped with a minicomputer that can typically identify the characteristic energy level of individual element and count the number of quanta in different energy windows to calculate the intensity distribution. Fig 5.2(a) presents an EDX spectrum obtained on a Co₈₀Fe₂₀(0.9nm)/Al₂O₃(3nm) sample where various elements and their relative intensities are shown. It was found that apart from the desired elements, i.e., Co, Fe, Al, and O of the sample, other elements such as K and Br from the substrate, Cu from the grid, Si from the detector, and Mn as an impurity from the preparation chamber are also present. Comparison of the intensity ratios yields Co and Fe fractions of 82 % and 18 %, respectively, hence, revealing a good stoichiometry of the metallic Co₈₀Fe₂₀ nanoparticles.

The multilayer structure of the DMIMs was verified by SAXR taken on Philips PW 1730 XRD system. Fig. 5.2(c) shows a typical reflectometry curve obtained on a $[\text{CoFe}/\text{Al}_2\text{O}_3(3\text{nm})]_{10}$ multilayer. Owing to the discontinuity of the metallic layers superstructure Bragg peaks only up to second order are observed. The oscillations with small periods correspond to the total thickness interference of the multilayer.

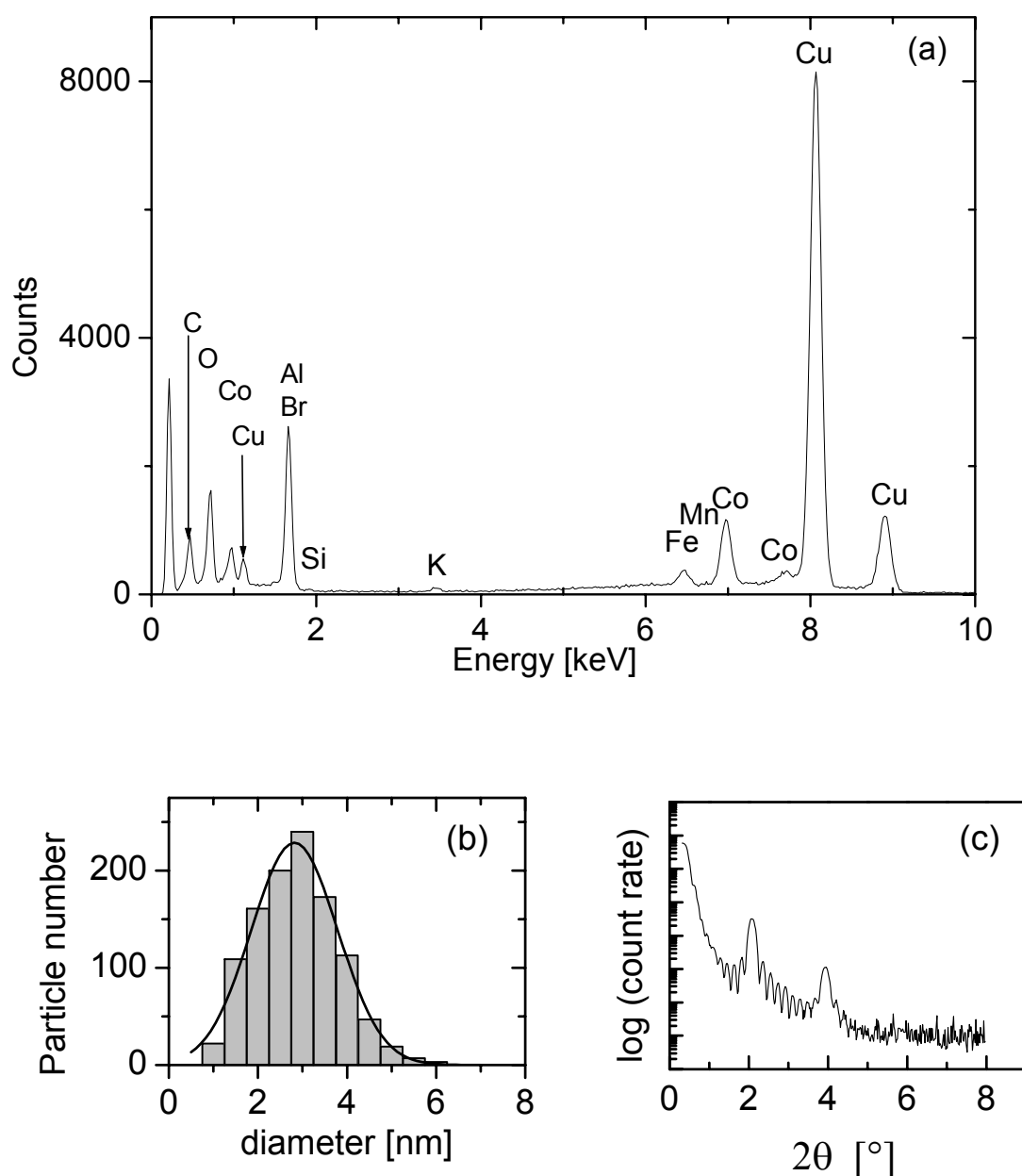


FIG. 5.2. (a) EDX spectrum obtained during TEM. (b) Particle size distribution obtained after image analysis of the micrographs shown in Figs. 5.1 (a) and (b). (c) SAXR diagram of a $[\text{CoFe}(0.9\text{nm})/\text{Al}_2\text{O}_3(3\text{nm})]_{10}$ multilayer.

The sharpness of the metal-insulator interface is readily verified by confirming the absence of unidirectional anisotropy after field-cooling (FC) to below the Néel temperature T_N of a possible CoFe oxide surface due to interfacial reaction of CoFe with Al_2O_3 [73]. As shown in Fig. 5.3 we do not observe any exchange bias [82] giving rise to a shift of the hysteresis loop after FC at temperatures below the antiferromagnetic (AF) ordering temperature. The loops displayed in Fig. 5.3 have been recorded at $T = 10$ K after zero-field cooling (ZFC) and FC in $\mu_0 H = 1$ T, respectively, from $T = 300$ K. They are completely identical and symmetric about $\mu_0 H = 0$. They indicate the absence of any core-shell FM-AF structure.

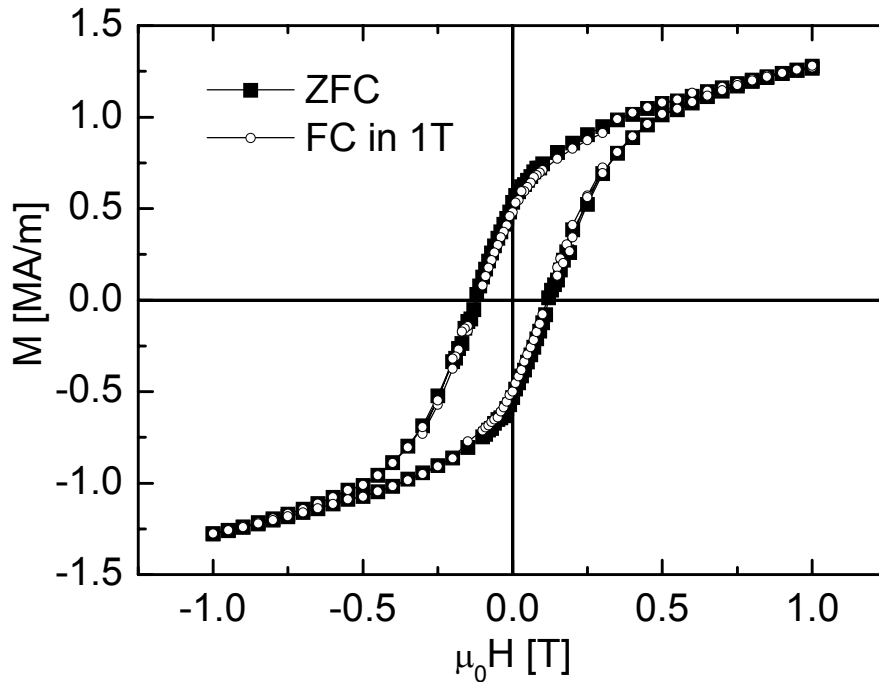


FIG. 5.3. M vs. $\mu_0 H$ loops recorded at $T = 10$ K after ZFC and FC in $\mu_0 H = 1$ T, respectively, of the DMIM system $[\text{CoFe}(0.9\text{nm})/\text{Al}_2\text{O}_3(3\text{nm})]_{10}$.

5.2. DMIMs in the SSG limit

In this section, we begin with the magnetic investigation in the high temperature regime in order to evidence the superparamagnetic behavior of the DMIM system [CoFe(0.9nm)/Al₂O₃(3nm)]₁₀. This property can then be utilized to extract the magnetic moment of individual CoFe nanoparticles (“superspins”). Then we focus on the temperature regime where dynamical effects sets-in in the experimental time window. The question of individual blocking and collective SSG freezing of the superspins will be addressed. In this context the relaxational behavior of the particle assembly will be contested within the framework of Arrhenius-Néel-Brown-type law (transition at $T = 0$) and that of a critical power law, characteristic of a phase transition at finite T_g . This will be followed by static criticality study where the behavior of the non-linear susceptibility will be tested. A Cole-Cole analysis will then be presented in terms of appropriate empirical models of relaxational polydispersivity.

We then concentrate on the low temperature long-time equilibrium and non-equilibrium dynamics of the DMIM system. Various magnetization relaxation protocols will be employed to study such phenomena: magnetic aging, memory-imprinting, chaos, and rejuvenation. The observations will be discussed within the framework of existing models. Finally, the influence of external magnetic fields on the low temperature state will be presented.

5.2.1. High Temperature properties: evidence of superparamagnetic features

In order to evidence the SPM behavior at least two requirements must be fulfilled. First, the magnetization curve must show no hysteresis, since this is not an equilibrium property. Second, the magnetization must be temperature dependent in the sense that the normalized magnetization, M/M_s , when plotted against $\mu_0 H/T$ must result in a universal curve. Here M_s is the saturation magnetization of the system as obtained for $\mu_0 H = 0.5$ T.

Figure 5.4 presents M/M_s vs. $\mu_0 H$ curves measured at $T = 100, 70,$ and 60 K. They are fully reversible indicating that the particle system is in thermal equilibrium. Furthermore, as expected, all M/M_s curves collapse onto a single curve as a function of $\mu_0 H/T$. These features clearly reveal the SPM behavior of the DMIM system [CoFe(0.9nm)/Al₂O₃(3nm)]₁₀ at $T \geq 60$ K.

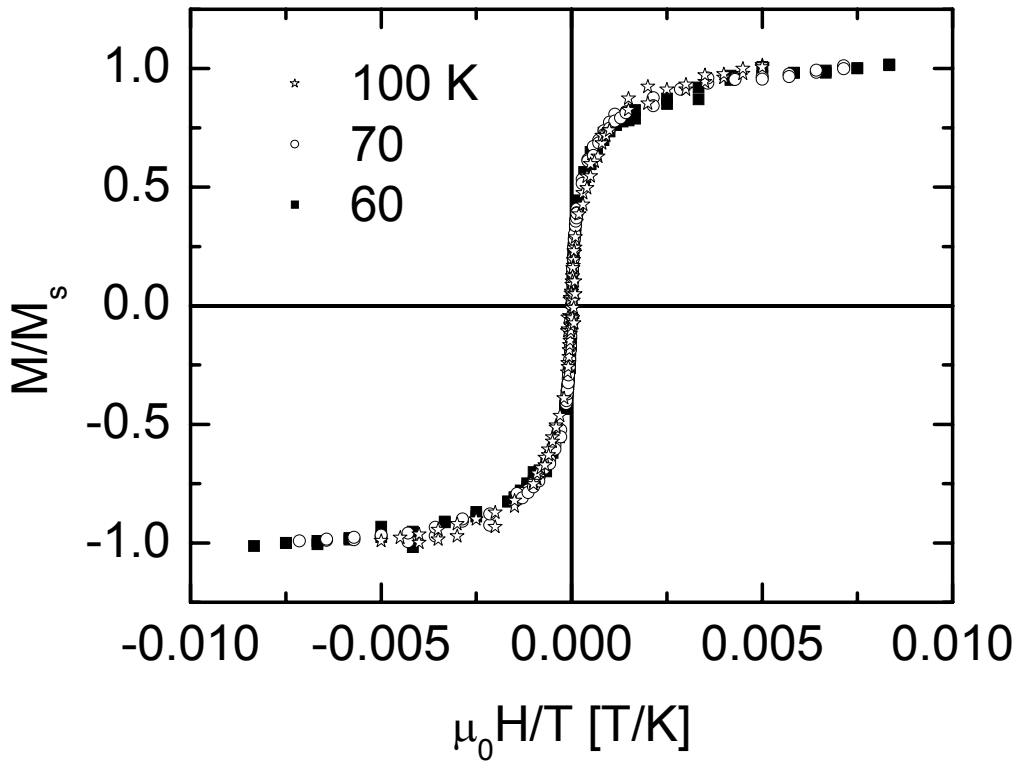


FIG. 5.4. Normalized magnetization, M/M_s , as a function of $\mu_0 H/T$ at $T = 100, 70,$ and 60 K of the DMIM system $[\text{CoFe}(0.9\text{nm})/\text{Al}_2\text{O}_3(3\text{nm})]_{10}$.

Figure 5.5 shows a fit of the Langevin function, $M = M_s L(\mu H / k_B T)$, to the experimental data obtained at $T = 100$ K. Here $M_s = n\mu$, n refers to the number of particles per unit volume and μ to the average value of the magnetic moment of a particle. We obtain $\mu = (2874 \pm 128)\mu_B$, where μ_B is the Bohr magneton and a particle volume density $n = (0.05 \pm 0.01) \text{ nm}^{-3}$.

Figure 5.6 presents zero-field-cooled (ZFC) and field-cooled (FC) magnetizations (M^{ZFC} and M^{FC} , respectively) vs. T involving an external magnetic field of $\mu_0 H = 0.2$ mT. The standard procedure of a typical M^{ZFC} and M^{FC} measurement is as follows: (i) the sample is cooled in zero field from the SPM regime, e.g., $T = 100$ K in Fig. 5.6, to $T < T^*$ (T^* may be the blocking temperature T_b or the glass temperature T_g), e.g., $T = 10$ K in Fig. 5.6. (ii) a field step of $\mu_0 H$ is applied at $T = 10$ K and M^{ZFC} is recorded during heating up to 100 K. (iii) M^{FC} was measured during a subsequent cooling from $T = 100$ K without changing the magnetic field.

From Fig. 5.6 it is observed that M^{ZFC} and M^{FC} are reversible down to $T \approx 60$ K. If we associate an effective observation time of 100s to the measurement this feature indicates that equilibrium of the system has been reached in the measuring time.

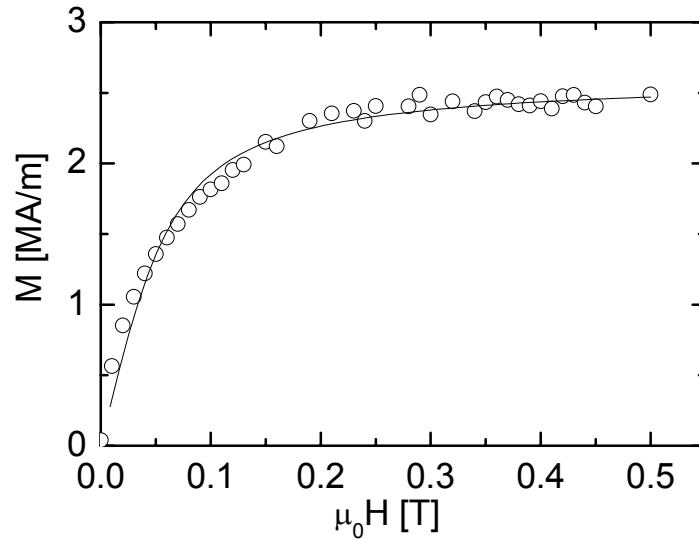


FIG.5.5. Magnetization as a function of applied field at $T = 100$ K. The solid line is a fit to the Langevin function.

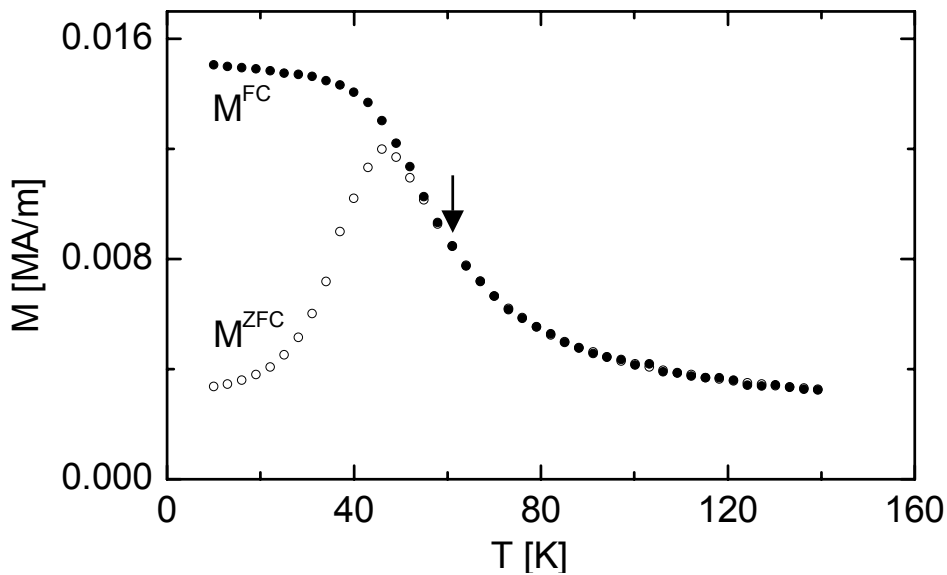


FIG. 5.6. Zero-field-cooled and field-cooled magnetizations, M^{ZFC} and M^{FC} , respectively, involving an external magnetic field of $\mu_0 H = 0.2$ mT.

5.2.2. Low temperature properties: individual blocking vs. cooperative freezing

Looking at the behavior of M^{ZFC} and M^{FC} in Fig. 5.6 in the low temperature regime, i.e., $T < 50$ K, two important features are noticed. The first one is the irreversibility between the two curves, appearing approximately at the maximum temperature, $T_m = 46$ K, of M^{ZFC} curve. The second one is related with the time and temperature effects of M^{ZFC} and M^{FC} . M^{ZFC} is zero until the field is applied, in Fig. 5.6, at $T = 10$ K. Then with $\mu_0 H$ on and T constant, it jumps to a value depending on the strength of $\mu_0 H$ and an effective time. The effective time is the sum of the time of the field change and the measuring time of the first data point. At this stage if we wait long enough, we expect an asymptotic approach, $\lim_{t \rightarrow \infty} M^{ZFC} = M^{FC}$. On the other hand, if we proceed to increase the temperature at some reasonable rate dT/dt , M^{ZFC} drifts upwards and attains a maximum value at T_m . This trace is irreversible and is a function of the rate dT/dt . Such behavior does not occur with M^{FC} , it is fully reversible. The corresponding *dc*-susceptibilities, $M^{ZFC}/\mu_0 H$ and $M^{FC}/\mu_0 H$, are referred to as non-equilibrium (disordered) and equilibrium (ordered) ones, respectively.

The above mentioned features are commonly associated with *non-ergodic* systems such as spin glasses and assemblies of magnetic nanoparticles both in the non-interacting and in the interacting limits. In the case of a non-interacting assembly of magnetic nanoparticles individual blocking of the particle moments is expected [12,13]. However, in the case of an interacting nanoparticle system either an interaction-induced modified blocking of particle moments is expected to occur within the framework of the SPM model [15] or a collective freezing of particle moments might occur and lead to a collective SSG state [22-24,30,31,83-85]. In order to decide on one of these possibilities we must carry out representative experiments that can help discriminating among the above possible behaviors.

Here we first examine the novel critical behavior and the various manifestations of a phase transition of our DMIM system. Various criteria of a non-collective behavior will simultaneously be tested and their implications will be discussed. We then turn to examine some important relaxation experiments characterizing the low temperature frozen-in state.

5.2.2.1. Dynamic criticality

The dynamics of an ensemble of nanoparticle system can be probed via *ac*-susceptibility experiments covering a wide frequency range, e.g., $10^{-2} - 10^3$ Hz. In such experiments, the ground state properties of the system remain virtually unaffected by the application of a small oscillating field. Fig. 5.7 illustrates the temperature dependence of the *ac*-susceptibility of the DMIM system $[\text{CoFe}(0.9\text{nm})/\text{Al}_2\text{O}_3(3\text{nm})]_{10}$ measured in the frequency range $10^{-2} \leq f \leq 1$ Hz at an *ac*-amplitude $\mu_0 H_{ac} = 0.05$ mT after ZFC from $T = 150$ K, i.e., starting from the SPM regime [30]. The *ac*-susceptibility, $\chi = \chi' - i\chi''$, has two components, a real part χ' , the dispersion and an imaginary part χ'' , the absorption.

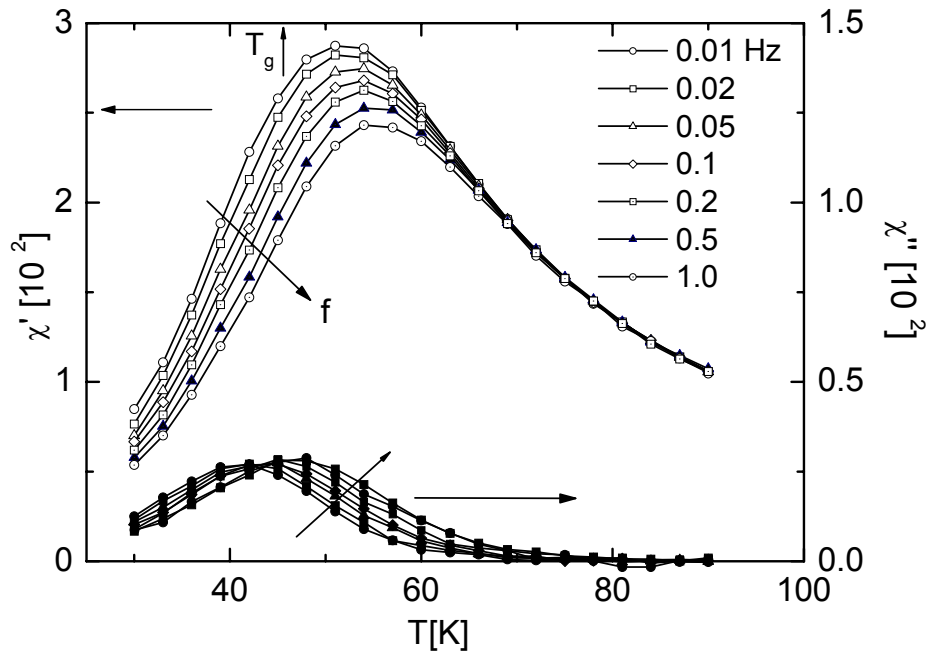


FIG. 5.7. χ' and χ'' vs. T of the DMIM system $[\text{CoFe}(0.9\text{nm})/\text{Al}_2\text{O}_3(3\text{nm})]_{10}$ measured at different frequencies f as indicated in the figure (data points interpolated by spline functions). The glass temperature T_g is marked by an arrow.

It is seen that the peaks of both χ' and χ'' shift towards lower temperature on decreasing the frequency f or, equivalently, increasing the observation time $t = 1/\omega$, where $\omega = 2\pi f$. A peak in χ' (or in the low field dc-magnetization $M/\mu_0 H$) refers to the situation where the observation time t equals the relaxation time τ of the system. Thus, useful information on the relaxational dynamics can be obtained from the variation of the peak position, T_m , of $\chi'(T)$ at different frequencies. As explained in Chapter 2, in the case of a

collection of non-interacting nanoparticles with randomly distributed anisotropy axes the relaxation time follows an Arrhenius law, $\tau \equiv 1/\omega = \tau_0 \exp(KV/k_B T)$, within the framework of the Néel-Brown model [12,13]. Here τ_0 is the inverse attempt frequency, K the anisotropy constant, V the volume of the particle, and k_B the Boltzmann constant. Fig. 5.8(a) shows a plot of $\log_{10}[\tau/s]$ vs. $1/T_m$, which yields $KV = 2.4 \times 10^{-20}$ J and $\tau_0 = 10^{-23}$ s when fitted to the Arrhenius law (solid line). While the value of anisotropy energy KV appears reasonable, the rather unphysical value of τ_0 implies that the relaxational dynamics of the system cannot be adequately described by the Néel-Brown model.

Alternatively, the data are very well described by assuming critical dynamics of a spin glass with a finite static glass temperature T_g [42] as shown in Fig. 5.8(b). Indeed, a best fit of the data to the power law $\tau = \tau^* (T_m/T_g - 1)^{-z\nu}$ yields $T_g = (45.6 \pm 4.6)$ K, a dynamic critical exponent $z\nu = 10.2 \pm 4.6$, and a relaxation time of individual particle moment $\tau^* = (2.8 \pm 1.3)10^{-7}$ s. It should be noticed that the fairly large values of τ^* refers to the single superspin dynamics, which obeys Arrhenius-Néel-Brown behavior, $\tau^* = \tau_0 \exp(KV/k_B T)$ [83,85], with $\tau_0 \approx 10^{-10}$ s and $KV \approx 10^{-20}$ J. The values of $z\nu$ and τ^* are very close to those reported on frozen ferrofluids [83], where the formation of a low-temperature collective SSG state has been claimed. It is worth mentioning that similar τ^* and $z\nu$ values have also been obtained for another DMIM system with $t_n = 0.9$ nm prepared in a different batch [73]. However, a larger value of $T_g = 61$ K was found in this case.

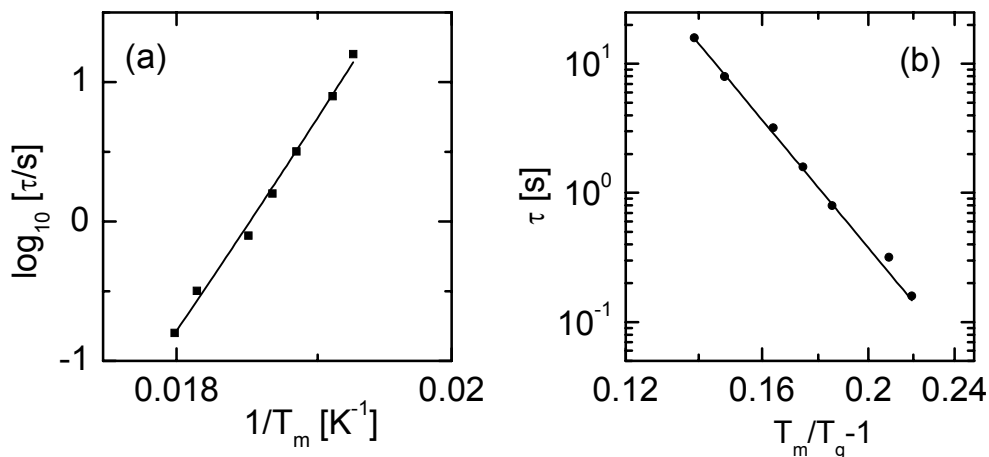


FIG. 5.8. (a) $\log_{10}[\tau/s]$ vs. $1/T_m$ and the best fit to an Arrhenius law (straight line).

(b) τ vs. $T/T_g - 1$ and the best-fit to a power law (straight line).

Another useful quantity that can be obtained from ac-susceptibility is the relative shift of T_m at different frequencies, $k = \Delta T_m / T_m \Delta \log \omega$ [42]. The value of k is found to be 0.034 which is rather similar to that found in the $\text{Eu}_{0.2}\text{Sr}_{0.8}\text{S}$ spin glass system [86]. These properties give very strong hints at a collective rather than a single-particle low-temperature behavior of our nanoparticle DMIM system $[\text{CoFe}(0.9\text{nm})/\text{Al}_2\text{O}_3(3\text{nm})]_{10}$. This low temperature collective state, as mentioned above, is referred to as the SSG state because of the involvement of superspins ($\mu \approx 10^3 \mu_B$) in the ordering process.

As discussed in Chapter 3, dynamic scaling of χ'' can also be tested in order to get supporting evidence for the critical behavior of the superspin glass transition. A full scaling analysis of $\chi''(\omega, T)$ is shown in Fig. 5.9. Here the data from Fig. 5.7 are best-fitted according to Eq. (3.17) by plotting $(T/T_g - 1)^{-\beta} \chi'' / \chi_{eq}$ vs. $\omega \tau^* (T/T_g - 1)^{-z\nu}$. The function $\chi_{eq}(T)$ is approximated by a Curie-Weiss hyperbola, $\chi'(f = 0.01 \text{ Hz}, T) = \chi_0 / (T - T_0)$, best-fitted to the respective low- f data within the range $60 \leq T \leq 90 \text{ K}$, while trial values of $z\nu$ and T_g are chosen to be close to the above dynamic power law fits. It is seen that data sets are reasonably collapsing when choosing consistent parameter sets, $T_g = 44 \text{ K}$, $z\nu = 10.0$ and $\beta = 1.0$. The value $\beta = 1.0$ complies with observations on SSG systems like (17 %) Fe-C [87]. Hence, the dynamic scaling analysis further corroborate the fact that our DMIM system with nominal thickness $t_h = 0.9 \text{ nm}$ represents a generic SSG.

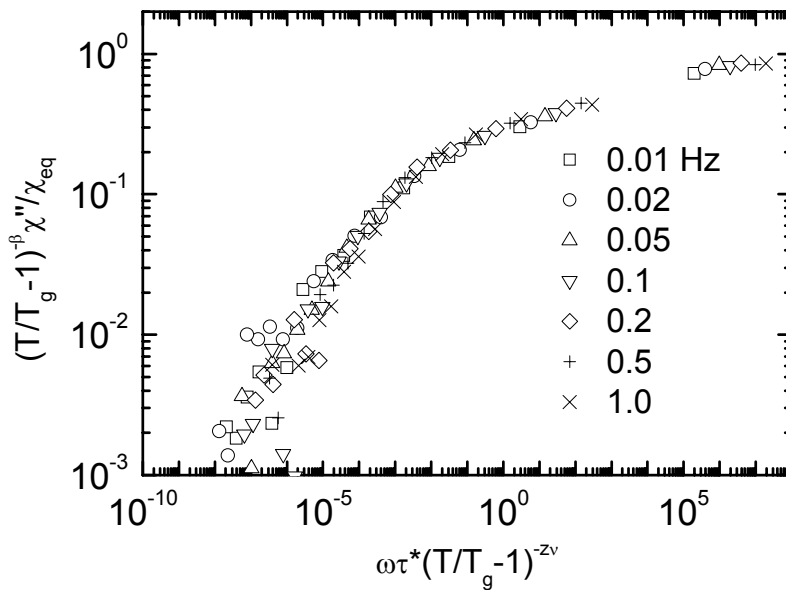


FIG. 5.9. Dynamic scaling plots $(T/T_g - 1)^{-\beta} \chi'' / \chi_{eq}$ vs. $\omega \tau^* (T/T_g - 1)^{-z\nu}$ of the susceptibility data shown in Fig. 5.7, best-fitted by the parameter sets $T_g = 44 \text{ K}$, $z\nu = 10.0$, $\beta = 1.0$, and $\chi_{eq} = 0.115 / (T - 42.5 \text{ K})$.

5.2.2.2. Static criticality

Another crucial test that can definitely prove the existence of a superspin glass state relies on the divergence of the critical non-linear susceptibility χ_3 at the glass temperature T_g as explained in Chapter 3. To this end magnetization isotherms M vs. $\mu_0 H$ were recorded after ZFC from $T = 150$ K at temperatures $52 \leq T \leq 64$ K in fields $0 \leq \mu_0 H \leq 0.08$ mT at steps of 0.01 mT resolution. They are displayed in Fig. 5.10 at some selected temperatures.

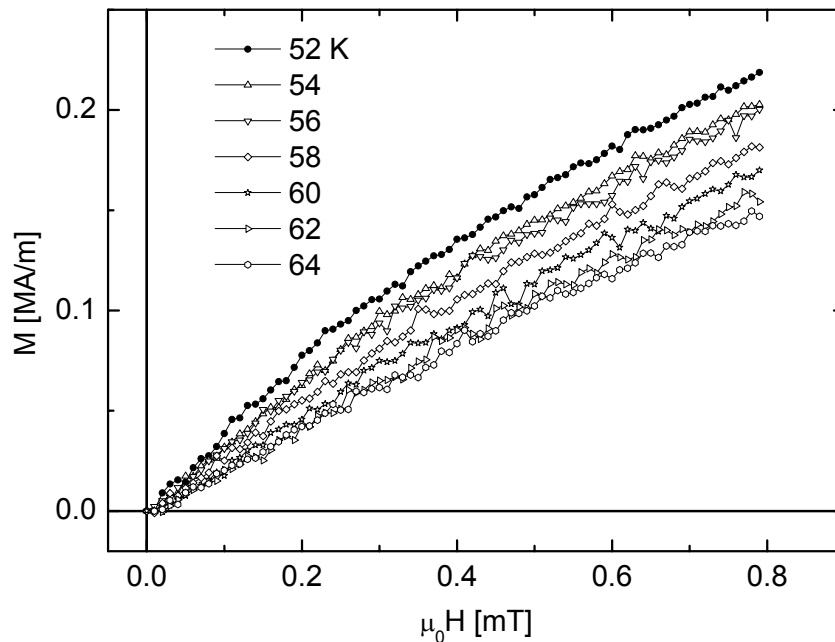


FIG. 5.10. Magnetization isotherms at some selected temperatures as indicated in the figure.

In order to warrant thermal equilibrium, i.e. to achieve the static limit, the critical slowing down has been overcome by isothermal equilibration times between data points, $t_w = 200$ and 500 s at $T > 60$ K and ≤ 60 K, respectively. The data were fitted to a polynomial, $M = \chi_1 H - \chi_3 H^3 + \chi_5 H^5$, where χ_3 is expected to diverge at T_g in case of a collective spin-glass phase transition. The results are plotted in Fig. 5.11 together with a best-fitted power law, $\chi_3 = \chi_3^0 (T/T_g - 1)^{-\gamma}$ revealing $T_g = (43.6 \pm 1.5)$ K, $\gamma = 1.47 \pm 0.20$ and $\chi_3^0 = (2.5 \pm 1.3)10^{-5} (\text{m/A})^2$. Within errors T_g agrees with the value obtained from dynamic scaling. The critical exponent $\gamma \approx 1.5$ is smaller than that observed on spin

glasses, $\gamma \approx 4$ [88]. This seems to hint either at proximity to mean-field behavior, $\gamma = 1$ [42] owing to the long-range nature of the dipolar interaction, or due to spurious blocking processes of some of the largest particles of the system [31].

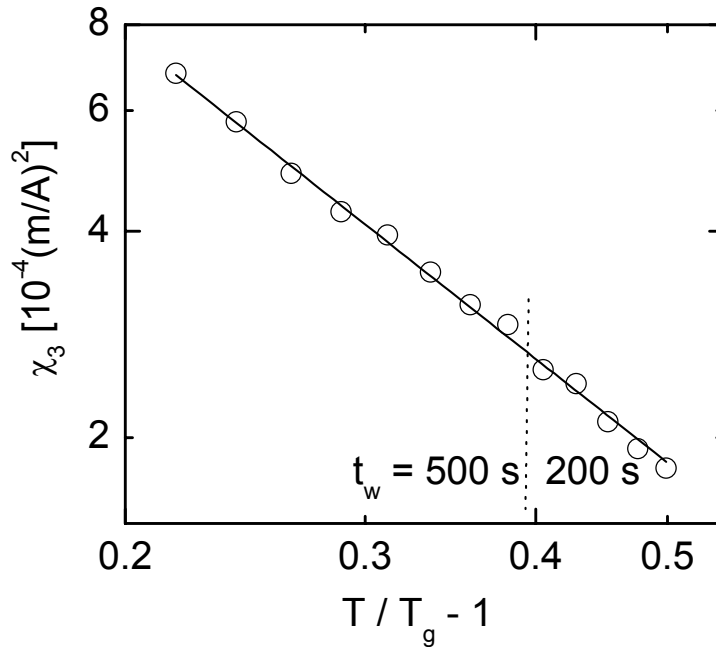


FIG. 5.11. χ_3 vs. $T/T_g - 1$ (obtained after wait times t_w as indicated) and best fit to power law, $\chi_3 = \chi_3^0 (T/T_g - 1)^{-\gamma}$, with $T_g = (43.6 \pm 1.5)$, and $\gamma = (1.47 \pm 0.2)$ (straight line).

We have also performed the static criticality test in an alternative way [31]. For this purpose, the temperature variation of the ZFC *dc*-magnetization was recorded under various magnetic fields, $0.05 \leq \mu_0 H \leq 0.7$ mT, as shown in Fig. 5.12 (a). The curves are qualitatively similar to each other. The peak positions shift slightly downwards in temperature at increasing magnetic field. From the M vs. T data isothermal cross sections M vs. $\mu_0 H$ are obtained both below and above the peak positions and fitted to polynomials, $M = \chi_1 H - \chi_3 H^3 + \chi_5 H^5$. χ_1 , χ_3 , and χ_5 data thus obtained are plotted against temperature in Fig. 5.12(b), (c) and (d), respectively. In Fig. 5.12 (b) the ZFC *dc*-magnetization in a field $\mu_0 H = 0.05$ mT (from Fig. 5.12 (a)) is compared with $\chi_1(T)$. It is seen that the peak positions of both curves coincide with each other, while the height and acuteness of the cusp appears slightly reduced in the χ_1 data. In Fig. 5.12 (c) the nonlinear

susceptibility, χ_3 , tends to diverge close to T_g . A power law, best fitted in the temperature range from 48 to 70 K (inset of Fig. 5.12 (c)) yields $\gamma = 1.43 \pm 0.10$ and $\chi_3 = (14 \pm 1) \times 10^{-5} \text{ (m/A)}^2$ keeping T_g fixed at 43.6 K. These values are in fairly good agreement with those obtained from the above static criticality test.

The nonlinear susceptibility, χ_5 , in Fig. 5.12 (d) also shows a sharp peak near to the expected transition temperature. One should notice that due to the above truncation of the series expansion, Eq. (3.11), χ_5 contains all higher order terms, χ_7 , χ_9 , etc. Hence, fitting to a power law may not yield the appropriate exponent. Indeed, the resulting exponent $2\gamma + \beta = 1.24 \pm 0.14$ appears too small, yielding an unreasonable value $\gamma = -1.6$, if $\beta = 1.4$. Obviously, one should consider higher order terms, up to at least order H^7 , when intending to make the χ_5 analysis.

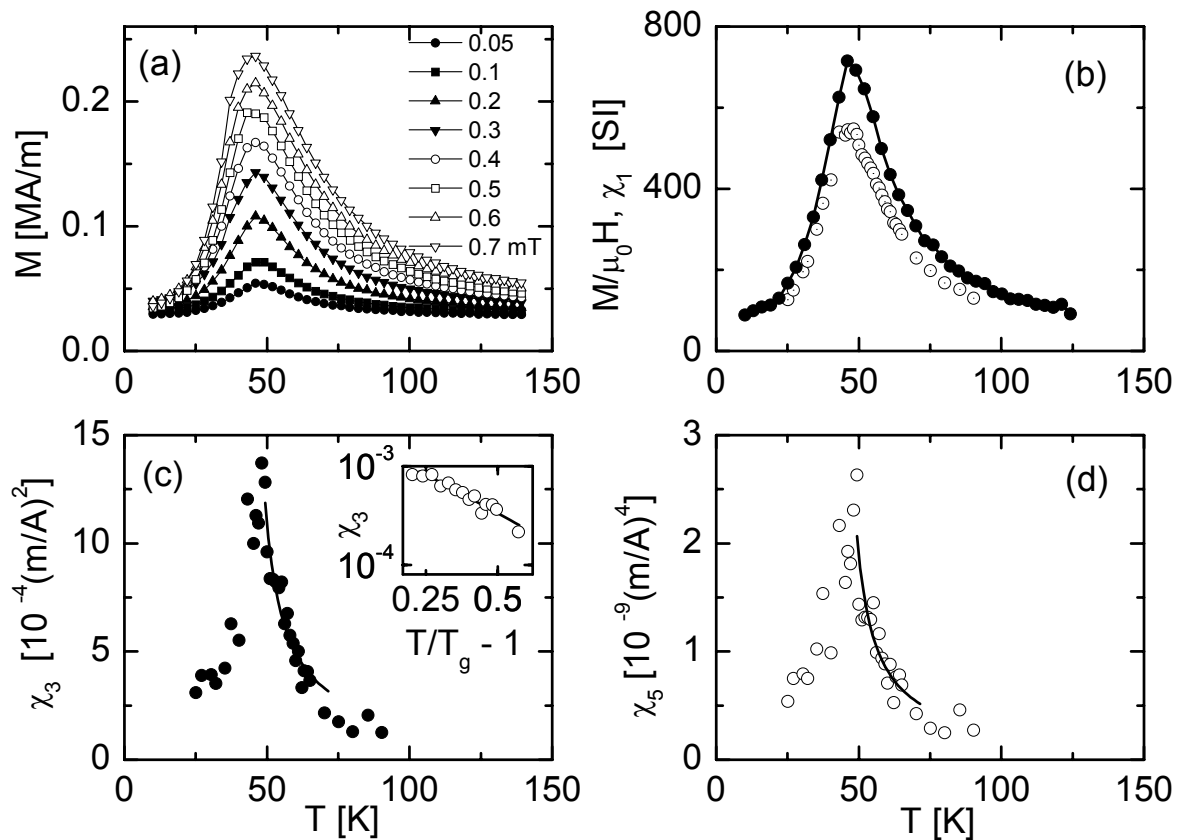


FIG. 5.12. (a) Temperature variations of the ZFC magnetization in various fields as indicated. (b) $M/\mu_0 H$ at $\mu_0 H = 0.05$ mT (Fig. 5.12(a), solid circles) and χ_1 (extracted from Fig. 5.12(a), dot centered circles) vs. T . (c) χ_3 and (d) χ_5 vs. T extracted from Fig. 5.12(a) and best fitted to power laws (solid lines). The inset to (c) shows a double logarithmic plot of χ_3 vs. $T/T_g - 1$, best fitted to a power law within 48 - 70 K.

5.2.2.3. Cole-Cole analysis

Cole-Cole analysis is sometimes used to estimate the distribution of relaxation times of a spin glass [89]. The complex *ac*-susceptibility, $\chi = \chi' - i\chi''$, is written in the Cole-Cole model as [90]

$$\chi(\omega) = \chi_s + \frac{\chi_T - \chi_s}{1 + (i\omega\tau_c)^{1-\alpha}} \quad (5.1)$$

where χ_T and χ_s are the isothermal ($f \rightarrow 0$) and adiabatic ($f \rightarrow \infty$) susceptibilities, respectively, τ_c is the characteristic relaxation time, and α a measure of the polydispersivity of the system. The case $\alpha = 0$ yields the standard Debye-type relaxator with one single relaxation frequency as expected, e.g., in the case of an ensemble of non-interacting superparamagnetic particles. The limiting case $\alpha = 1$ corresponds to an infinitely wide distribution of relaxation times. In spin glass systems, one expects values of α near to 1.

Decomposing Eq. (5.1) into its real and imaginary parts, one obtains

$$\chi'(\omega) = \chi_s + \frac{\chi_T - \chi_s}{2} \left(1 - \frac{\sinh[(1-\alpha)\ln(\omega\tau_c)]}{\cosh[(1-\alpha)\ln(\omega\tau_c)] + \cos[(1/2)(1-\alpha)\pi]} \right) \quad (5.2)$$

and

$$\chi''(\omega) = \frac{\chi_T - \chi_s}{2} \left(\frac{\sinh[(1/2)(1-\alpha)\pi]}{\cosh[(1-\alpha)\ln(\omega\tau_c)] + \cos[(1/2)(1-\alpha)\pi]} \right), \quad (5.3)$$

respectively.

Figure 5.13 shows χ' and χ'' as functions of frequency f at different temperatures $T = 45, 50, 55,$ and 60 K [91]. The spectra were recorded at an *ac*-amplitude of $\mu_0 H = 0.05$ mT after ZFC. While some negative curvature of χ' seems to indicate a well defined dispersion step at $f > 10^3$ Hz for $T > 60$ K, it becomes gradually broadened as T decreases. At lower T the real part, χ' , exhibits nearly constant negative slopes, thus corresponding to an extremely broad dispersion step. The imaginary part reveals extremely broad peaks which strongly shift to lower frequencies with decreasing temperature. Obviously our SSG system exhibits a very wide distribution of relaxation times with a pronounced temperature dependence.

Each isotherm spectrum $\chi'(f)$ and $\chi''(f)$ in Fig. 5.13 can be fitted to Eq. (5.2) and (5.3), respectively, in order to extract the corresponding critical relaxation time τ_c and polydispersity exponent α . It is relatively easier to perform the fitting of χ'' since only three parameters, $\chi_T - \chi_s$, $1-\alpha$, and τ_c are required, whereas in case of χ' four parameters are required. The solid lines in Fig. 5.13(b) are the best fitted curves according to Eq. (5.3).

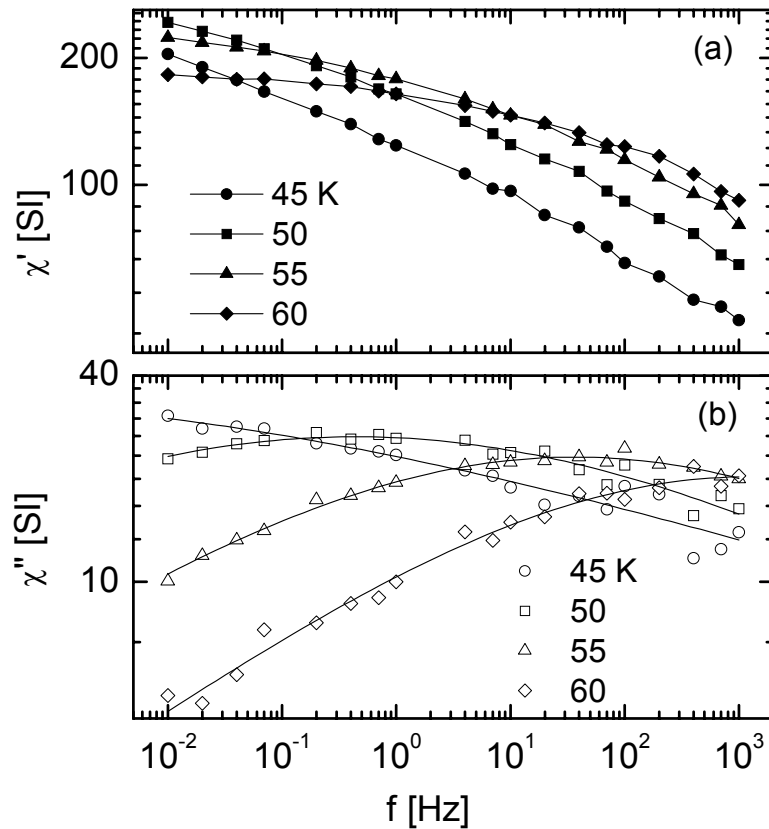


FIG. 5.13. χ' and χ'' vs. f at different temperatures as indicated. The lines in (a) are guides to the eye and in (b) are best fits according to Eq. (5.3).

The values of τ_c and α obtained from the fits are plotted vs. T in Fig. 5.14. It is observed that τ_c increases by eight orders of magnitude with decrease in temperature from $T = 60$ to 45 K. Furthermore, the τ_c data when fitted to a power law, $\tau_c = \tau_0(T/T_g - 1)^{-z\nu}$ yield $\tau_0 = 5.0 \times 10^{-8}$ s, $T_g = 43.0$ K, and $z\nu = 9.0$, consistent with the values obtained previously from dynamic and static criticality analyses (section 5.2.2.1 and 5.2.2.2). The exponent α increases, as expected, with decreasing temperature. Its high value ($\alpha \approx 0.8$)

meets the requirement that the DMIM system exhibits a broad distribution of relaxation times.

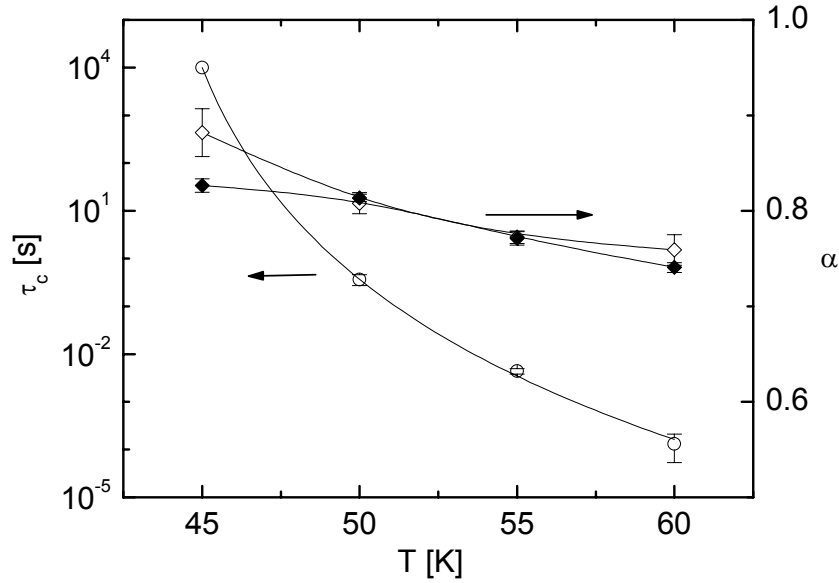


FIG. 5.14. τ_c (open circles) and α (open diamonds) vs. T obtained from best fits of Eq. 5.3 to $\chi''(f)$ data. τ_c is best fitted to a power law (solid line) as explained in the text. α (closed diamonds) are obtained from fits of Eq. 5.4 to χ' vs χ'' data in Fig. 5.15.

In order to further illustrate the relaxation time distribution, the susceptibility data can be plotted in the complex plane as χ' versus χ'' , where each frequency represents one point. These so called Cole-Cole plot yields a perfect semicircle centered on the χ' axis at $(\chi_T + \chi_s)/2$ and with radius $(\chi_T - \chi_s)/2$ for a classic Debye-relaxator. The apex of the semicircle corresponds to $\omega\tau = 1$. Non-zero α has the effect to depress the semicircle such that angles between the χ' -axis and the tangents at $\omega = 0$ and $\omega \rightarrow \infty$ are $\mp(1 - \alpha)\pi/2$, respectively. Fig. 5.15 shows the Cole-Cole plot of the SSG system. Eqs. (5.2) and (5.3) can be expressed in the form [92]

$$\chi''(\chi') = \frac{\chi_T - \chi_s}{2 \tan[(1 - \alpha)\pi/2]} + \left\{ (\chi' - \chi_s)(\chi_T - \chi') + \frac{(\chi_T - \chi_s)^2}{4 \tan^2[(1 - \alpha)\pi/2]} \right\}^{1/2} \quad (5.4)$$

The best fits of Eq. 5.4 to χ' vs. χ'' data are shown in Fig. 5.15 by solid curves. The resulting values of α shown in Fig 5.14 by closed diamonds are comparable to those obtained from χ'' vs. f analysis referring to Fig. 5.13 (b) (open diamonds). These considerations clearly evidence the superspin glass nature of our nanoparticle system.

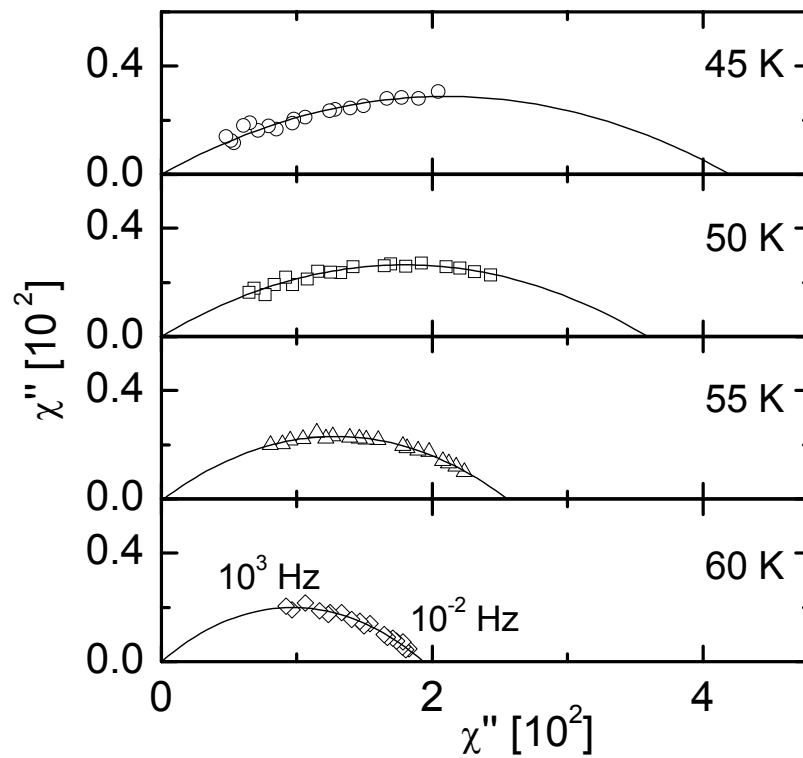


FIG. 5.15. Cole-Cole plots of the SSG system. The frequency of the ac -field increases from right to left. The curves are best fits to Eq. (5.4).

5.2.3. Non-equilibrium dynamics of the superspin glass state

We have shown that the DMIM system $[\text{CoFe}(0.9\text{nm})/\text{Al}_2\text{O}_3(3\text{nm})]_{10}$ exhibits a low temperature SSG state below $T_g \approx 44$ K. A spin glass below T_g is always in a non-equilibrium state owing to its extremely large equilibration times. As a consequence it exhibits characteristic features like aging, memory, chaos, and rejuvenation in the spin glass phase. For a SSG nanoparticle system analogous phenomena can also be expected. In the following we describe some well defined experiments for our DMIM system $[\text{CoFe}(0.9\text{nm})/\text{Al}_2\text{O}_3(3\text{nm})]_{10}$.

5.2.3.1. Magnetic aging

Magnetic aging was first observed in **CuMn** spin glass by Lundgren *et al.* [93]. They found that relaxation of ZFC magnetization strongly depends on the wait time, t_w , at a measurement temperature $T_m < T_g$, before the probing field is applied and the magnetization is recorded as a function of time. The procedure for an aging experiment is illustrated in Fig. 5.16.

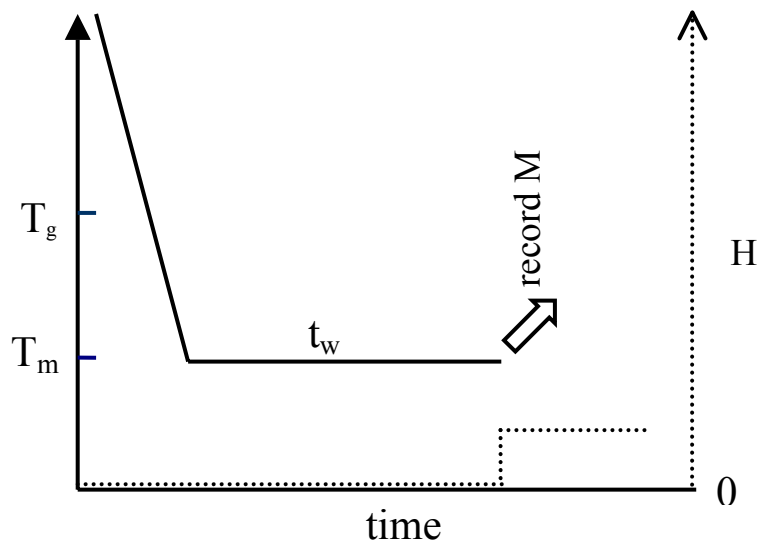


FIG. 5.16. The time-temperature-field procedure for an aging experiment.

Fig. 5.17 shows the relaxation of ZFC magnetization, M^{ZFC} vs. $\log t$, obtained at $T = 32, 42,$ and 60 K [94]. The employed wait times, t_w , are indicated in each plot. The measurements were performed at a probing field of $\mu_0 H = 0.04$ mT. At 32 and 42 K, they show a clear wait time dependence with points of inflexion at times close to the corresponding wait times, i.e, the system ages. In contrast, at $T = 60$ K the relaxation is independent of the wait time, implying that the observed relaxation is governed by noncollective thermally activated dynamics of individual particles and the system behaves like a SPM one. The wait time dependence is more clearly reflected in the relaxation rate, $S = \frac{1}{\mu_0 H} \frac{\partial m}{\partial \ln t}$, as shown in Fig. 5.18.

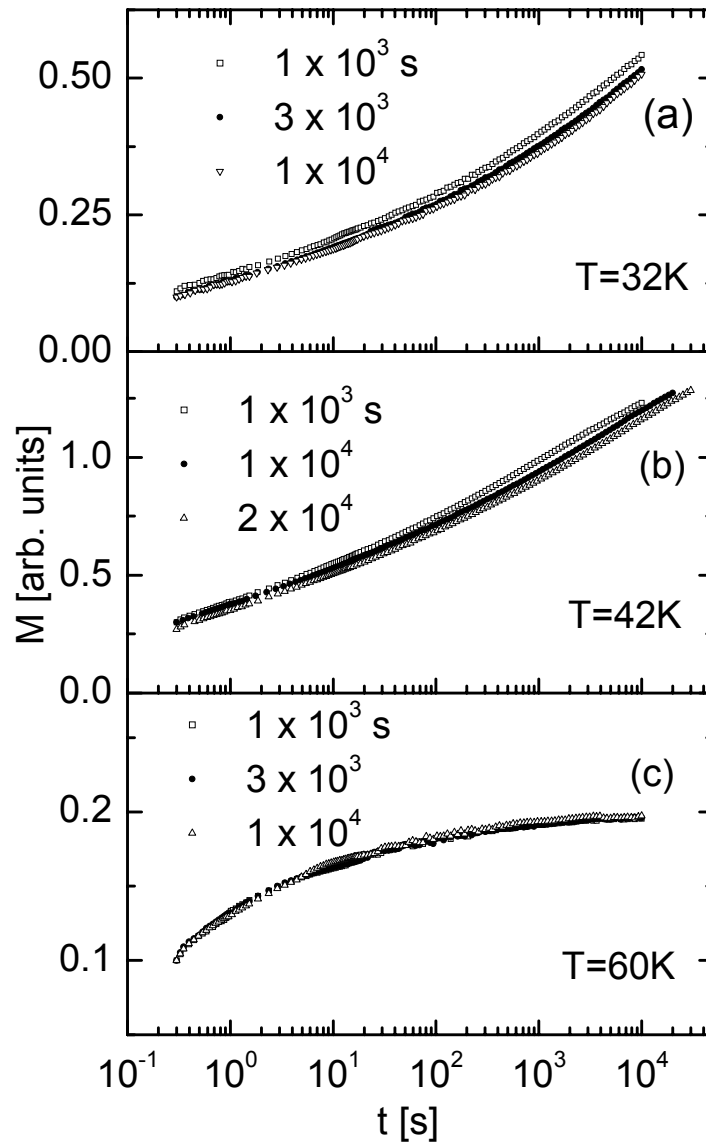


Fig. 5.17. Relaxation curves M vs. $\log t$ at temperatures $T = 32$ K (a), 42 K (b), and 60 K (c) recorded at $\mu_0 H = 0.04$ mT after different wait times t_w as indicated.

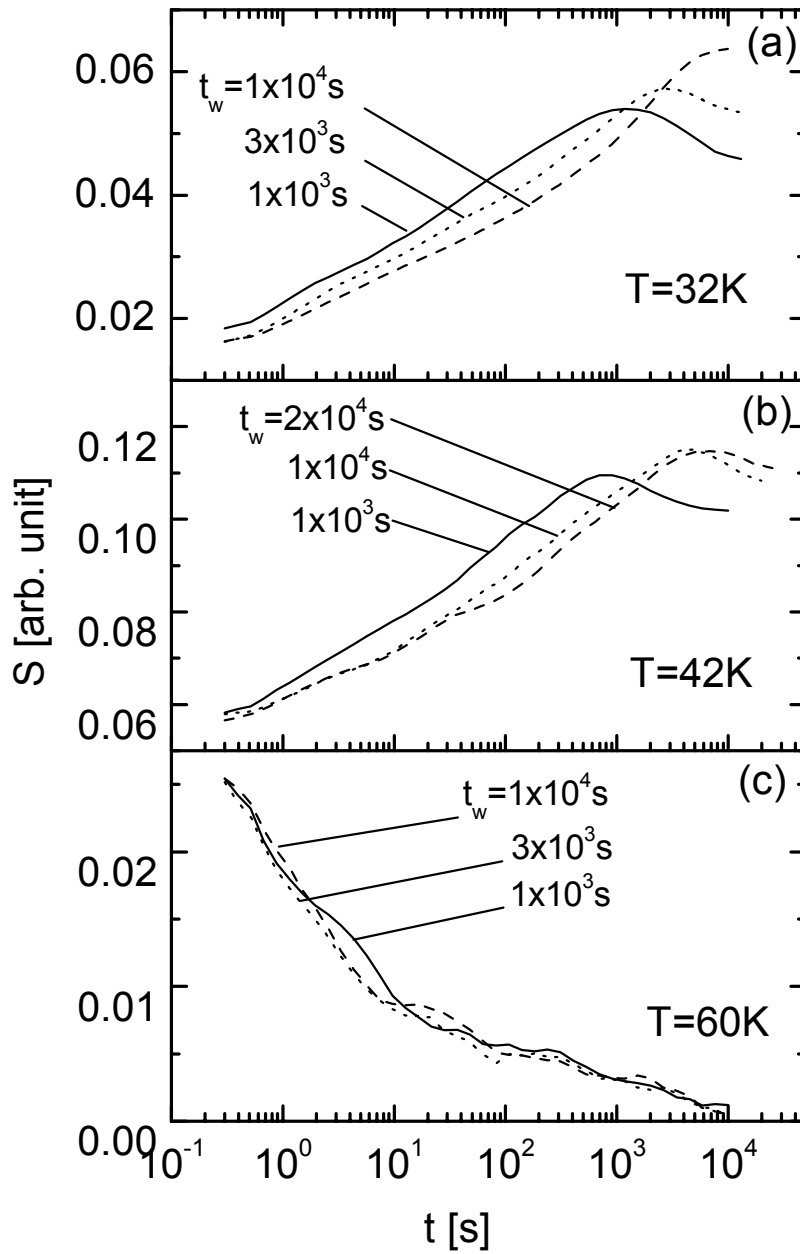


FIG. 5.18. Relaxation rate S vs. $\log t$ at $T = 32$ K (a), 42 K(b), and 60 K(c) corresponding to the relaxation curves of FIG. 5.18. Different wait times t_w are indicated in each plot.

The characteristic aging observed in the SSG phase implies that the correlation between the particle magnetic moments develops in the same way as the correlation between the spins of an atomic spin glass [93]. It indicates that non-equilibrium phenomena play a key role for the dynamics at low temperatures. This non-equilibrium dynamics can be dealt within the context of the droplet model [51] of spin glasses.

According to this model the approach towards equilibrium after a quench from above T_g to $T_m < T_g$ is governed by the growth of equilibrium domains during aging in the SG phase. As discussed in Chapter 3, a typical domain size after an aging time t_a ($t_a = t_w + t$) is $R(t_a) = [T \ln(t_a/\tau^*)/\Delta(T)]^{1/\psi}$, where τ^* is the relaxation time of an individual particle moment, $\Delta(T)$ sets the free energy scale, and ψ a barrier exponent. When a small probe (dc) field is applied, the domain is probed via the polarization of droplets of size $L(t) = [T \ln(t/\tau^*)/\Delta(T)]^{1/\psi}$. Two limiting cases can be considered: (i) $\ln t \ll \ln t_a$, where $L(t) \ll R(t_a)$ and (ii) $\ln t \gg \ln t_a$, where $L(t) \approx R(t_a)$ (since, $t \approx t_a = t + t_w$). In the first case, quasi-equilibrium dynamics is probed whereas in the second case the probed length scale involves domain walls. This crossover from equilibrium to non-equilibrium response is reflected by a point of inflexion in M or, equivalently, a peak in the relaxation rate S vs. time.

5.2.3.2. Memory-imprint and rejuvenation effect

Although the spins in the spin glass phase are frustrated and the ground state is chaotic on changing the temperature, it does exhibit robustness of its equilibrium properties. Such phenomena as memory-imprinting and rejuvenation have recently been observed in the spin glass phase [54,95,96] by employing specific experimental protocols as illustrated in Fig. 5.19.

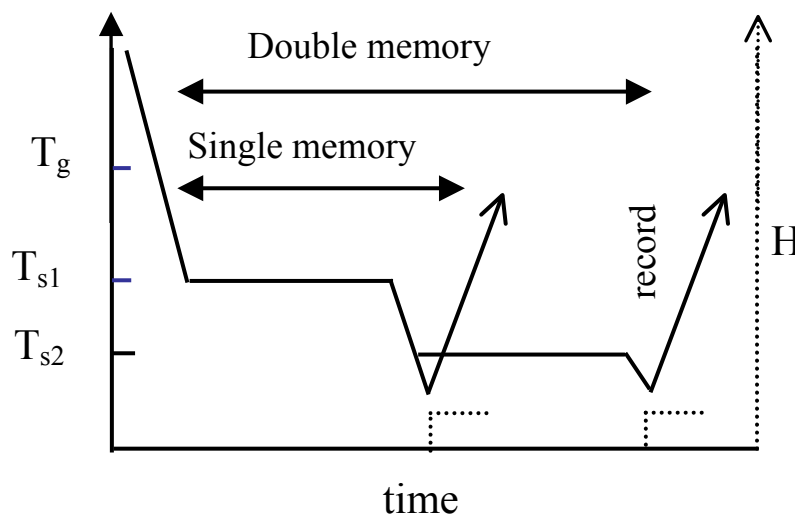


Fig. 5.19. The experimental procedure in a single and double memory experiment.

In a memory experiment, the sample is ZFC from $T > T_g$ to a stop temperature $T_s < T_g$ (T_{s1} and $T_{s2} < T_{s1}$ in a double memory experiment), where the system is aged for a certain duration before further cooling down to lower temperatures and the field-induced magnetization is recorded during heating. This is referred to as a stop-and-wait protocol.

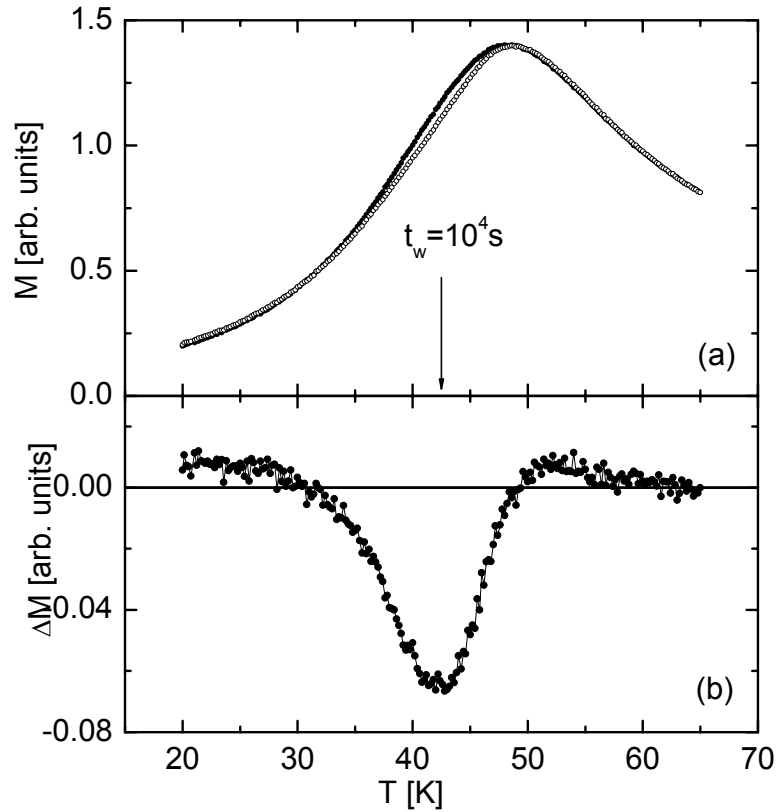


Fig. 5.20. (a) Temperature dependence of the reference magnetization, $M_{\text{ref}}(T)$ (solid circles), and of the magnetization with a stop-and-wait protocol, $M(T)$ (open circles), at a magnetic field of $\mu_0 H = 0.04$ mT. (b) $\Delta M = M(T) - M_{\text{ref}}(T)$ vs. T .

Figure 5.20 illustrates the memory and rejuvenation effects of the ZFC dc -magnetization after a stop-and-wait at $T_s = 42$ K $= 0.95T_g$ for a duration of 10^4 s [97]. As can be seen in Fig. 5.20(a), the data corresponding to the intermittent stop-and-wait (open squares) lay significantly below the reference curve (solid circles) at temperatures close to T_s . This difference indicates that the magnetic moment configuration spontaneously rearranges towards equilibrium via growth of equilibrium domains, when the system is left unperturbed at constant temperature T_s . These equilibrated domains become frozen-in

on further cooling and are retrieved on reheating. In other words, the system shows a memory effect, which is observed as a minimum in $\Delta M = M(T) - M_{\text{ref}}(T)$ at about T_s in Fig. 5.20 (b). The fact that reference and the stop-and-wait curves coalesce at low temperatures and only start to deviate as T_s is approached from below, clearly indicates that rejuvenation [98] of the system occurs as the temperature is decreased away from T_s in the stop-and-wait protocol. These effects are similar to those reported in ordinary atomic spin glasses [96].

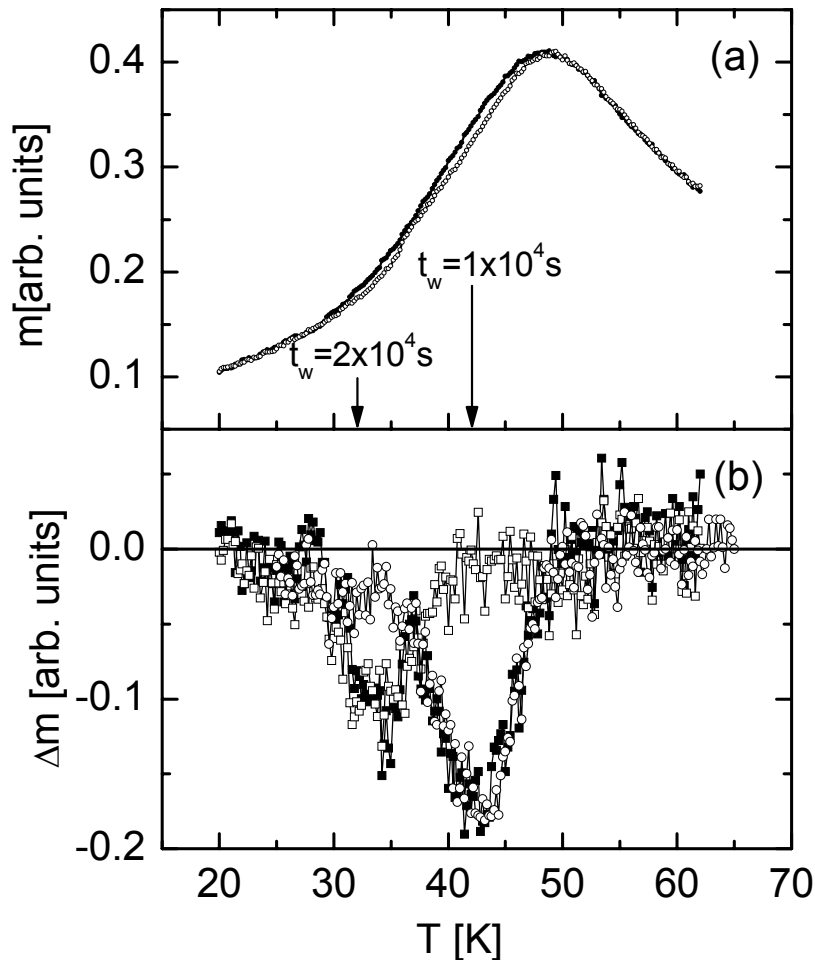


Fig. 5.21. Comparison of the reference magnetization, $M_{\text{ref}}(T)$, (solid circles) with the magnetization, $M(T)$, (open circles) employing a double stop-and-wait protocol. The data are recorded at $\mu_0 H = 0.1$ mT. (b) ΔM vs. T for the double stop-and-wait protocol (solid squares) in comparison with two independent stop-and-wait protocols at 42 K and 32 K for durations of 10^4 s and 2×10^4 s (open circles and squares, respectively).

Figure 5.21 presents a double memory and aging experiment: the cooling process is interrupted twice at $T_{s1} = 42$ K $= 0.95 T_g$ and $T_{s2} = 32$ K $= 0.72 T_g$ for durations of 10^4 s

and 2×10^4 s, respectively. Upon subsequent reheating M^{ZFC} shows memory anomalies at the corresponding T_s values as seen in Fig 5.21(a), and ΔM as seen in Fig. 5.21(b) shows two distinct minima. The double memory curve [solid squares in Fig. 5.21(b)] can be regarded as a superposition of two independent stop-and-wait experiments as shown by two ΔM curves obtained consecutively at $T_s = 42$ and 32 K (open circles and squares, respectively). One also sees that the stop-and-wait magnetization curves coalesce with the reference curve except at temperatures close to T_s which, as discussed above, signals rejuvenation.

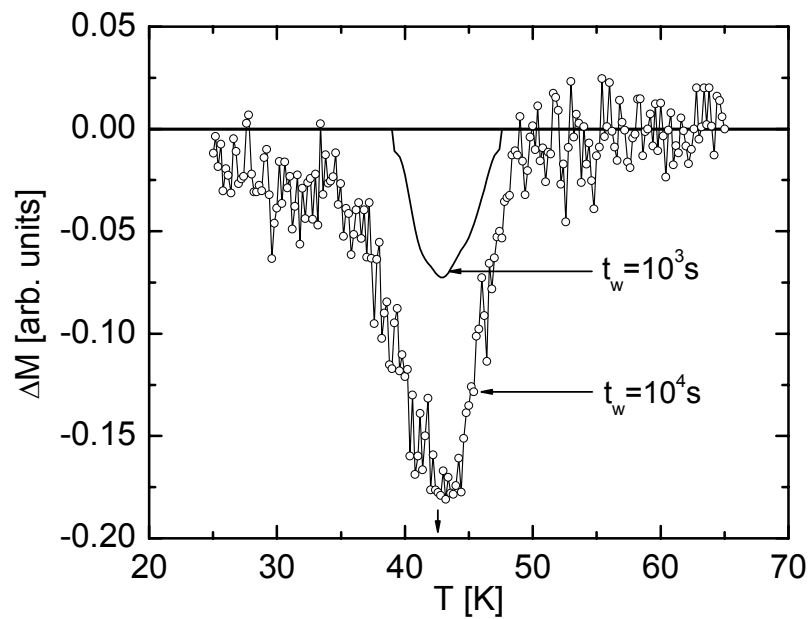


Fig. 5.22. Comparison of ΔM vs. T for two single memory dips at $T = 42$ K for stop durations of 10^3 and 10^4 s (solid curve and open circles, respectively). The solid curve corresponds to smoothed ΔM data.

According to the domain growth law [51] the depth of a memory dip should approximately increase linearly with logarithmically increasing stop times. Fig. 5.22 shows ΔM vs. T for two different stop times, $t_s = 10^3$ and 10^4 s at $T = 42$ K. The expected linear increase of the memory dip with the logarithm of the stop time is supported by the data.

The memory imprinting phenomenon can also be observed in the thermoremanent magnetization (TRM) employing another stop-and-wait protocol [73]. Curve 1 in Fig. 5.23 (a) is a reference curve measured after rapidly quenching the sample in a field of $\mu_0 H = 0.1$ mT from $T = 90$ K, where the system shows a superparamagnetic behavior, to 30 K. The data are recorded after removing the field on heating at a constant rate of 0.5 K/min. Curve 2 is subsequently recorded after employing a stop-and-wait protocol, where the sample is rapidly quenched from $T = 90$ K to an intermittent stop temperature $T_s = 50$ K, where it was aged for $t_w = 10^4$ s before further quenching to $T = 30$ K. Again, the data are recorded on heating the sample under the same conditions as chosen for the reference curve 1. As shown in Fig. 5.23 (b) the difference of the two data sets maximizes at T_s , while no enhancement of M is observed at low T . This is unexpected for an ensemble of non-interacting superparamagnetic particles, where the aged curve should lie above the quenched one at *all* temperatures. Indeed, the enhanced equilibration into the field aligned state for all particles when experiencing a halt at temperature T_s should not get lost upon further cooling. Actually, however, the sample retains a memory of a quasi-equilibrium state reached after aging in a weak field at the stop temperature. This quasi-equilibrium gets lost when quenching the sample to low temperatures because of the chaotic nature of the collective spin glass state [55], but it is rediscovered on reheating to T_s .

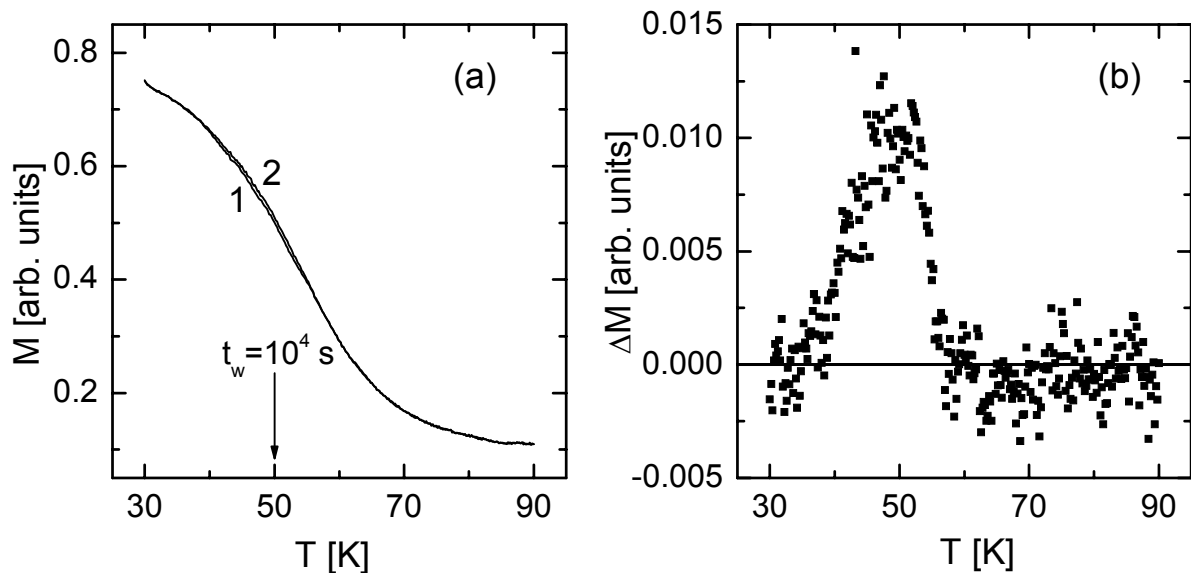


FIG. 5.23 (a) Temperature dependence of the reference TRM, M_{ref} (curve 1), and of the TRM after a stop-and-wait protocol, M (curve 2), after FC in $\mu_0 H = 0.1$ mT. (b) $\Delta M = M - M_{\text{ref}}$ vs. temperature.

Relaxation measurements of the thermoremanent magnetization, M^{TRM} , has also been studied by employing temperature cycle protocols [99]. In a temperature cycle protocol the sample is cooled in a constant field from $T = 100$ K to the measurement temperature $T_m < T_g$ and, after the field is set to zero, the relaxation of the M^{TRM} is measured immediately for a period t_1 , then the temperature is rapidly changed by ΔT and the relaxation is subsequently measured for a period t_2 , and finally the cycle is completed by returning to T_m , where the relaxation is recorded for a period t_3 .

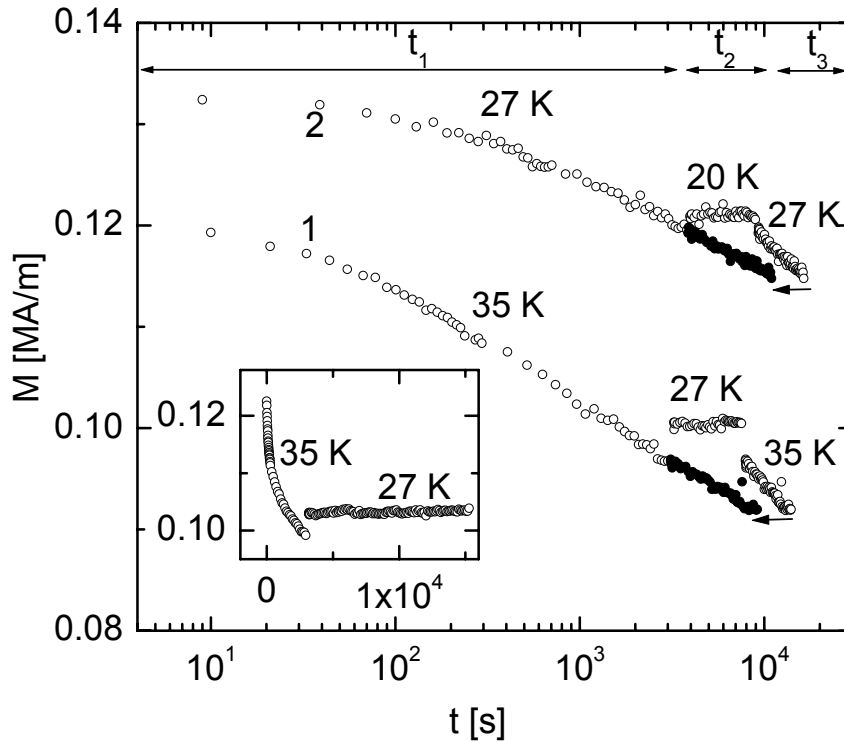


FIG. 5.24. Relaxation curves of M^{TRM} after field cooling with $\mu_0 H = 0.4$ mT at (1) $T_m = 35$ K ($t < 3000$ s), 27 K ($3000 < t < 8000$ s) and 35 K ($8000 < t < 14\,000$ s) and (2) $T_m = 27$ K ($t < 4000$ s), 20 K ($4000 < t < 9000$ s) and 27 K ($9000 < t < 17\,000$ s). The data referring to the last time intervals have been replotted against $t - 8000$ s as solid circles as indicated by arrows. The inset shows the relaxation cycle at $T_m = 35$ K ($t < 3000$ s) followed by a prolonged period ($3000 < t < 15\,000$ s) at 27 K. The inset shows the relaxation cycle at $T_m = 35$ K ($t < 3000$ s) followed by a prolonged period ($3000 < t < 15\,000$ s) at 27 K.

Figure 5.24 shows the relaxation of M^{TRM} at $T_m = 35$ (1) and 27 K(2), respectively, with negative temperature cycles. When temporarily cooling by $\Delta T = -8$ and -7 K, respectively, no relaxation is observed in either case. After heating, again, to T_m the previous relaxation continues as evidenced by shifting the time scale (solid symbols).

When comparing the two cases it is conjectured that the quasi-equilibrium state reached when cooling the sample from 35 to 27 K or from 27 to 20 K cannot simply be assigned to the temperature dependent relaxation of blocked particle magnetic moments. In this case, one should merely observe a change of the relaxation rate referring to the Néel-Brown-Arrhenius law. However, as can be seen in the inset to Fig. 5.25 the relaxation involving $T_m = 35$ K is completely suppressed when step cooling to $T = 27$ K even for prolonged periods, $t \approx 1.2 \times 10^4$ s.

The reason can be provided within the framework of the droplet model as follows [51]. It predicts that a droplet excitation, L , is associated with an energy barrier $B \propto L^\psi$ which must be surmounted by thermal activation. For the droplets to be active the condition $F_L \leq k_B T$ should be satisfied, where F_L is the free energy gain associated with the formation of a droplet of size L . Since the thermal activation process becomes slower as the temperature is lowered within the spin glass regime, the restarted domain growth at $T_m - \Delta T$ cannot proceed and the domains cannot become larger than the overlap length, $l_{\Delta T}$, which is a measure of the length scale below which equilibrium exists at both T and $T - \Delta T$. It should be noted that M^{TRM} comes back to the level it reached before cooling, when the temperature returns to T_m after temporary cooling. The solid circles show the data taken during t_3 shifted by t_2 , the time spent at $T_m - \Delta T$, along the time scale. It is found that the relaxation exactly continues the previous curve. In other words, the relaxation before temporary cooling is retrieved on returning to the measurement temperature.

On the other hand, the hierarchical picture [49] as discussed in Chapter 3 predicts the existence of a low temperature spin glass phase with a large number of nearly degenerate states separated by finite barriers, $\Delta(T)$. Hammann *et al.* [100] have studied the variation of $\partial\Delta T/\partial T$ vs. T and $\partial\Delta T/\partial T$ vs. $\Delta(T)$ and found that $\partial\Delta T/\partial T$ depends only on the particular value of $\Delta(T)$ and not on the temperature. They have shown that the finite barriers between the metastable states increase very steeply with decreasing temperature. An extrapolation suggests a divergence at lower temperatures. They have also suggested that in temperature cycles lowering the temperature splits the metastable states into a large number of new states. These new states merge again when the temperature is raised back. In this scenario, our experimental observations can be interpreted by the fact that intermediate cooling leads to a divergence of the energy barriers. As a consequence, the probed metastable states become pure states at the lower temperature. Thus, no new aging

is observed during temporary cooling. The system recovers the previous state when the temperature is raised back, thus yielding a memory effect.

Figure 5.25 shows the relaxation of M^{TRM} involving $T_m = 35$ K and small temperature cycles of $\Delta T = -1$ (1), -2 (2) and -3 K (3). It is observed that when temporarily cooling to $T = 32$ K (3), no relaxation is observed and the memory effect is observed upon heating to $T = 35$ K. On the other hand, the system continues to relax at $T = 34$ and 33 K, although at a slower rate during temporary cooling. Hence, on returning to $T_m = 35$ K the previous magnetic state cannot be retrieved. This is at variance with the situation after pulse cooling with $\Delta T = -3$ K, where a complete memory effect is observed. Obviously a specific temperature window exists within which the memory effect fails. This fact has previously been stated for conventional spin glasses [101]. The observation, of course, accords with both models. In the droplet model the statistical overlap of the droplet size distributions and in the hierarchical model the transitions over finite barriers can explain the loss of memory effect.

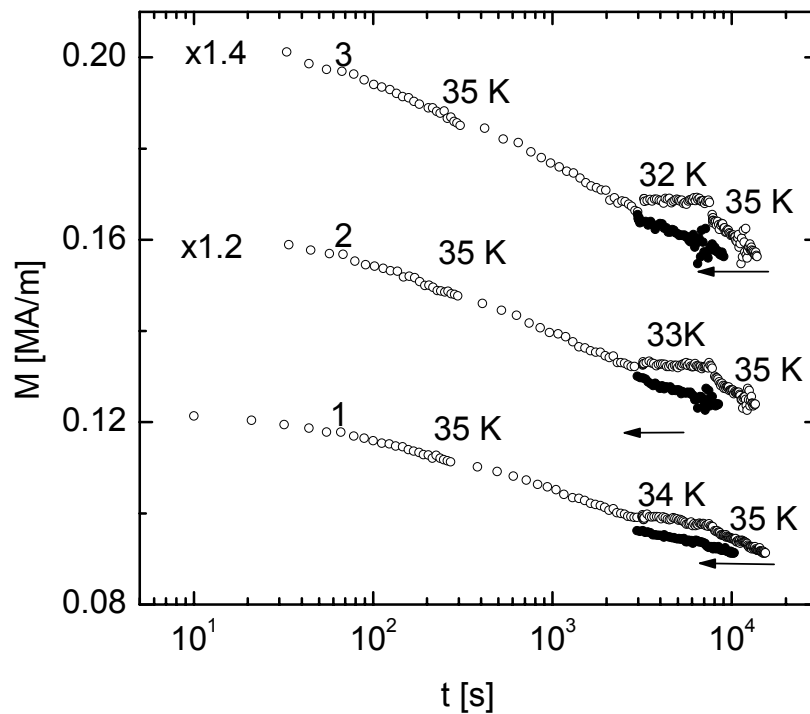


FIG. 5.25. Relaxation curves of M^{TRM} after field cooling with $\mu_0 H = 0.4$ mT at (1) $T_m = 35$ K ($t < 3000$ s), 34 K ($3000 < t < 8000$ s) and 35 K ($8000 < t < 14\,000$ s), (2) $T_m = 35$ K ($t < 3000$ s), 33 K ($3000 < t < 8000$ s) and 35 K ($8000 < t < 14\,000$ s) and (3) $T_m = 35$ K ($t < 3000$ s), 32 K ($3000 < t < 8000$ s) and 35 K ($8000 < t < 14\,000$ s). All data sets obtained within $8000 < t < 14\,000$ s have been replotted against $t - 5000$ s (solid circles).

Figure 5.26 shows the relaxation at subsequent positive and negative temperature cycles in one experiment. The most important observation is an asymmetric behavior in the positive cycle, where a faster relaxation is encountered during temporary heating, but is suppressed when returning to $T_m = 27$ K. The observation can be explained by the asymmetric variation of the free energy surface with temperature changes as proposed in the hierarchical picture. Due to an increase in temperature the barriers have been lowered at 35 K, thus enabling processes between renewed states, which were not accessible at 27 K. Hence, a faster relaxation is observed upon intermediate heating.

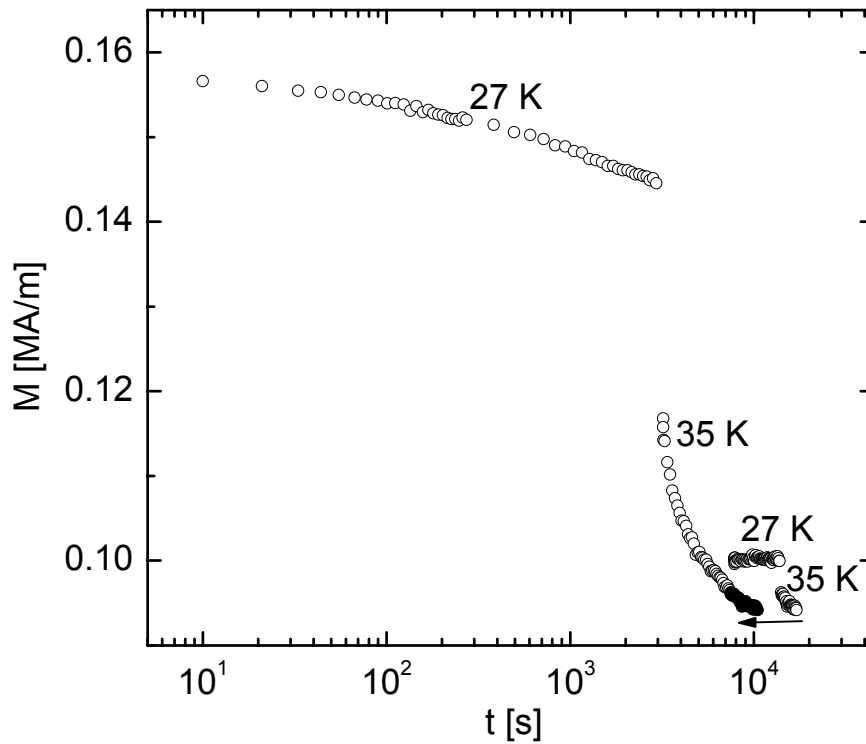


FIG. 5.26. Relaxation curves of M^{TRM} after field cooling with $\mu_0 H = 0.4$ mT. The positive cycle involves $T_m = 27$ K ($t < 3000$ s), 35 K ($3000 < t < 9000$ s) and 27 K ($9000 < t < 15000$ s). The negative cycle involves $T_m = 35$ K ($3000 < t < 9000$ s), 27 K ($9000 < t < 15000$ s) and 35 K ($15000 < t < 18000$ s). The latter data have been replotted against $t - 6000$ s (solid circles).

5.2.4. Effect of external magnetic field on the superspin glass transition

Spin glass ordering in the presence of an externally applied magnetic field has been matter of a long standing debate [102-104]. de-Almeida and Thouless (AT) [105] studied the effect of external field on the spin glass transition within the framework of the Sherrington-Kirkpatrick mean-field model [47]. They found that replica symmetry breaking (RSB) occurs both in zero and non-zero fields. This suggests the occurrence of spin glass transitions in finite fields. In the magnetic field $\mu_0 H$ vs. temperature T plane, the phase boundary between the paramagnetic and the spin glass phase is called an AT line and has the form,

$$\mu_0 H(T_{AT}) = A \tilde{\varepsilon}^\alpha, \quad (5.5)$$

where $\tilde{\varepsilon} = \left(1 - \frac{T_{AT}(H)}{T_{AT}(0)}\right)$ with $T_{AT}(0) \equiv T_g$ and the coefficient $A = \sqrt{\frac{4}{3}} \frac{kT_{AT}(0)}{g\mu_B S}$. A value of $\alpha = 3/2$ was predicted by de Almeida and Thouless.

Gabay and Toulouse (GT) [106] generalized the theory of de-Almeida and Thouless to vector spin glasses, in which the freezing-in of transverse and longitudinal spin components successively occurs at two different temperatures in the presence of a field. At decreasing temperature the transverse components freeze-in first at T_{GT} (Gabay-Toulouse temperature) as indicated by a weak difference of the zero-field cooled (ZFC) and field cooled (FC) magnetization, whereas the longitudinal components freeze-in at a lower temperature, T_{AT} , where a strong irreversibility in the magnetization occurs. In the case of the Heisenberg model with random anisotropy a crossover in the high field limit from AT to GT-type behavior was predicted [106]. A schematic drawing of this crossover behavior is shown in Fig. 5.27. The high field limit GT line has the form of Eq. (5.5) with

$$\alpha = 1/2 \text{ and } A = \sqrt{\frac{8}{(m+1)(m+2)}} \frac{kT_{AT}(0)}{g\mu_B S}, \text{ where } m = 1 \text{ (3) for Ising (Heisenberg)}$$

systems. The crossover from AT to GT line is attributed to the important role of anisotropy of the system. In the low-field regime, where the AT line is predicted, the anisotropy is important, whereas in the strong-field regime, where a crossover to GT line is predicted the anisotropy is unimportant.

On the contrary, scaling approaches within the framework of the droplet model [51] predict that any non-zero magnetic field destroys the spin glass ordering and makes the system paramagnetic. However, the model predicts a dynamic phase line $T_f(\mu_0 H)$,

where T_f corresponds to the freezing temperature. Its behavior depends on the observation time.

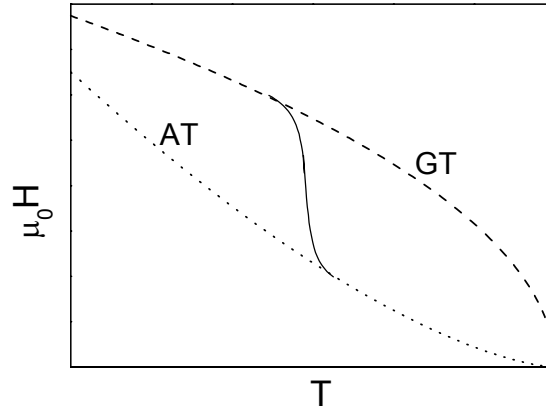


FIG. 5.27. Schematic drawing of the mean-field phase diagram with longitudinal Almeida-Thouless (AT) and transverse Gabay-Touless (GT) irreversibility onset lines.

The experimental situation is not clear-cut. While both lines, $T_{GT}(H)$ and $T_{AT}(H)$, have been found in Heisenberg-like spin glasses [107,108] like **CuMn**, in Ising-like spin glasses like $\text{Fe}_{0.5}\text{Mn}_{0.5}\text{TiO}_3$ only the $T_{AT}(H)$ line seems to occur [109]. However, even the latter was disputed within the framework of the droplet model. Mattsson *et al.* [103], reconsidered $\text{Fe}_{0.5}\text{Mn}_{0.5}\text{TiO}_3$ and argued that there is no spin glass phase transition in a magnetic field although a similar downward shift of the droplet freezing temperature, T_f , was found.

Recent Monte-Carlo (MC) simulations of the 3D Edwards-Anderson Ising-type spin glass with short range interactions [110] predict that the spin glass state survives in a non-zero magnetic field, where an AT line is encountered below a critical field. Moreover, MC simulations of the fully isotropic Heisenberg spin glass predict that it undergoes a chiral glass (CG) transition at finite fields [111]. Calculations show that the transition behavior within the framework of the chiral model is of RSB-type, thus close to the mean-field behavior [47] but the transition may well be of different nature. There is an anisotropy dependent crossover from AT- to GT-like behavior as in the mean-field model as shown in Fig. 5.27. The high field behavior can be described by Eq. (5.5) with $\alpha = 1.0$. Recent torque experiments performed on **AuFe** spin glasses in magnetic fields as high as 7 T support the chiral model phase diagram [108].

In order to evidence the survival of the SSG ordering in a magnetic nanoparticle system to the application of a magnetic field, one of the criticalities of the phase transition can be tested. For this purpose, *ac*-susceptibility was recorded in a magnetic field of $\mu_0 H = 1.0$ mT superimposed to an *ac*-amplitude of $\mu_0 H = 0.05$ mT at frequencies $0.01 \leq f \leq 1.0$ Hz [31]. The validity of dynamical critical scaling was tested similarly as in section 5.2.2.1 and is shown in Fig. 5.28. The apparent collapse of data sets onto a master curve clearly reveals the occurrence of the SSG ordering at this field.

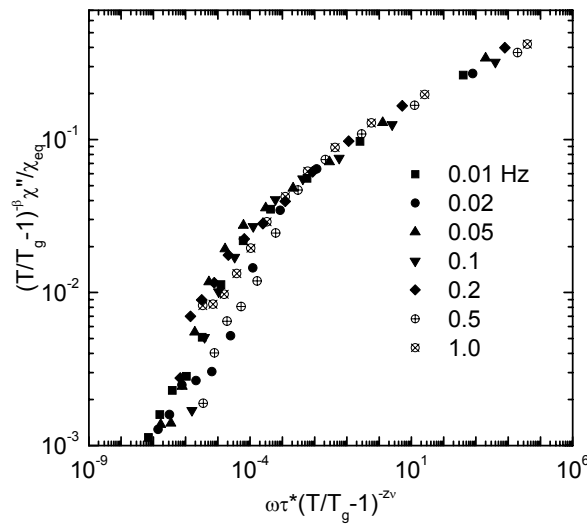


FIG. 5.28. Dynamic scaling plots $(T/T_g - 1)^{-\beta} \chi'' / \chi_{eq}$ vs. $\omega(T/T_g - 1)^{-z\nu}$ of the *ac*-susceptibility data measured in an external field $\mu_0 H = 1$ mT, best-fitted by the parameter set $T_g = 41$ K, $z\nu = 8.0$, $\beta = 1.0$, $\chi_{eq} = 6397/(T - 34.8 \text{ K})$, and $\tau^* = 10^{-7}$ s.

The above test inspired us to investigate the $\mu_0 H$ vs. T phase line of the SSG system. Fig 5.29 (a) and (b) exhibit M^{ZFC} and M^{FC} vs. temperature at various external magnetic fields, $\mu_0 H \leq 80$ mT. As expected the peak of M^{ZFC} shifts downwards at increasing field strength. The irreversibility, according to Sompolinsky [112], can be considered as the characteristic feature RSB. Owing to a distribution of particle sizes, the peaks of M^{ZFC} occur a little below the onset temperature of the irreversibility, which can be attributed to spurious blocking of larger particles whose blocking temperatures, T_b , exceed T_g . For this reason the difference $\Delta M = M^{\text{FC}} - M^{\text{ZFC}}$, displayed in the main panel of Fig. 5.30 at some selected fields $\mu_0 H = 2, 5$ and 10 mT, appears as a smooth function of T

without sharp kinks due to weak (*i.e.* transverse) or strong (*i.e.* longitudinal) irreversibility [106].

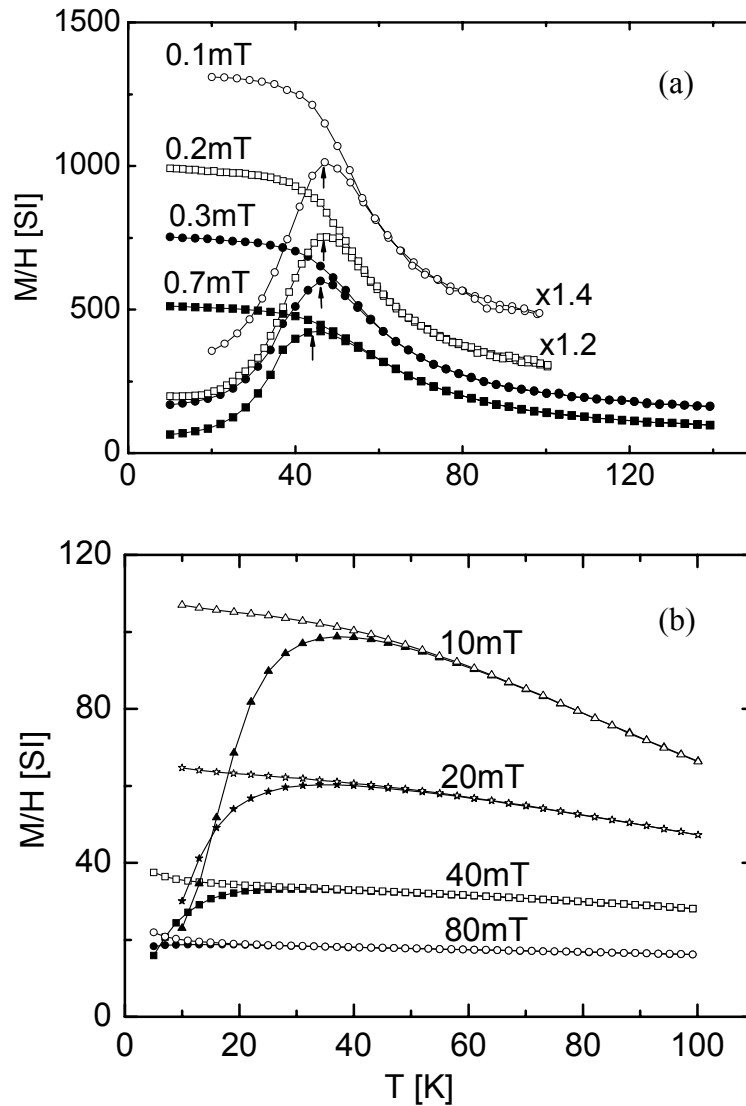


FIG. 5.29. M/H vs. T at various external fields as indicated in the plots.

In order to evidence the very existence of a $(\mu_0 H, T)$ phase boundary, *i.e.* Eq. (5.5), we have tested three different, but equally plausible modes: (i) the points of inflexion of $\Delta M(\mu_0 H)$, $T_1(\mu_0 H)$, (ii) the intersections of the steepest tangent of $\Delta M(\mu_0 H)$ with the T -axis, $T_2(\mu_0 H)$, and (iii) the peak positions of $M^{\text{ZFC}}(\mu_0 H)$, $T_3(\mu_0 H)$. The inset to Fig. 5.30 shows some selected plots of $d(\Delta M)/dT$ and ΔM vs. T at $\mu_0 H = 2, 5$ and 10 mT and the

corresponding points of inflexion, $T_1(\mu_0 H)$. The points of intersection, $T_2(\mu_0 H)$, are also indicated by arrows in the main panel.

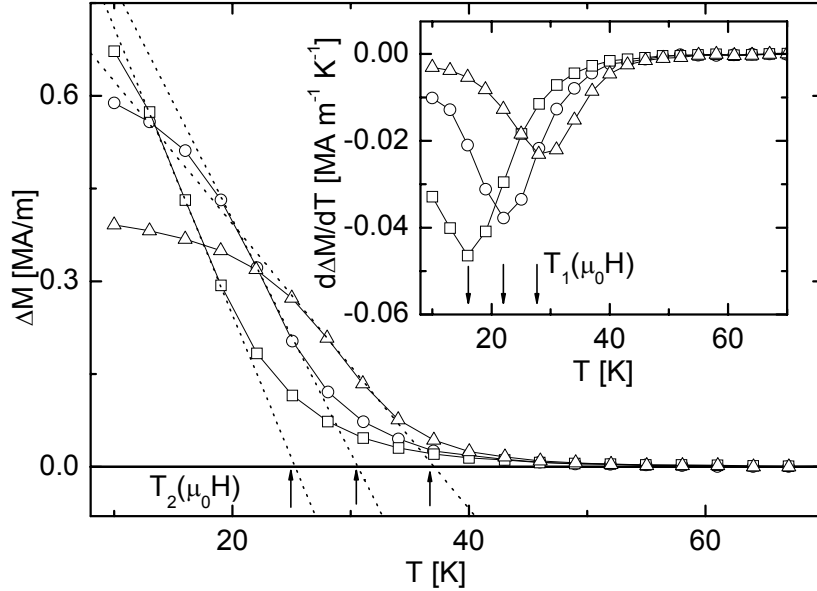


FIG. 5.30. Plots of $d\Delta M/dT$ (inset) and ΔM vs. T for $\mu_0 H = 2$ (triangles), 5 (circles) and 10 mT (squares). The corresponding points of inflexion, $T_1(\mu_0 H)$, and of intersection, $T_2(\mu_0 H)$, are indicated by arrows.

In Fig. 5.31 we present $T_1(\mu_0 H)$ (curve 1), $T_2(\mu_0 H)$ (curve 2), and $T_3(\mu_0 H)$ (curve 3). Although the curves are seriously shifted against each other along the T -axis, they have one important similarity in common. They are fairly flat in the low-field range, $\mu_0 H \approx 2$ mT, while they sharply ascend beyond $\mu_0 H \approx 5$ mT. Interestingly, best fits of the low-field data points according to Eq. (5.5) (solid curves) yield very similar exponents, $\alpha = 1.3 \pm 0.6$ (1), 2.6 ± 1.0 (2) and 1.5 ± 0.4 (3), but different prefactors, $A = 8.8$ mT (1), 38.5 mT (2) and 52.0 mT (3), and $T_{AT}(0) = (41.1 \pm 3.1)$ K (1), (54.4 ± 4.9) K (2) and (48.0 ± 0.6) K (3). While all exponents come close to the mean-field prediction, $\alpha = 3/2$ [105], comparison with the value $T_g \approx 44$ K obtained previously clearly favors curve 1 to become the best candidate for the ubiquitously expected AT line. In addition, its prefactor is very close to those predicted for the 3D Heisenberg ($A = 8.2$ mT) and the 3D Ising model ($A = 15.0$ mT) [113].

The strong rise of all curves at $\mu_0 H \geq 5\text{mT}$ reminds us of the AT-to-GT [106] or of the AT-to-CG crossover [111] predicted for the randomly anisotropic 3D Heisenberg spin glass. Owing to the restricted range of temperatures, $T = 10\text{ K}$, no points of inflexion are available for $\mu_0 H > 10\text{ mT}$, where curve 1 merely shows the largest $\Delta M(\mu_0 H)$ values. Moreover, the points of inflexion obtained up to the highest field range show no saturation tendency as expected for the above two crossovers. We therefore consider the peak positions of M^{ZFC} to study the high field behavior. They show a saturating tendency as expected for the above two crossover scenarios. Although the GT line can be taken as representing a true transition, it is essentially invisible in any longitudinal measurement, *e.g.* magnetization differences [108]. This implies that the magnetization measurements at high fields cannot be used as a reliable probe of the onset of true transverse spin freezing.

Alternatively, $T_3(\mu_0 H)$ data when fitted at $\mu_0 H \geq 40\text{mT}$ by Eq. (5.5) yields $\alpha \approx 0.8$, hence, very close to that expected for CG crossover $\alpha = 1$ [111]. Hence, we tentatively propose that a crossover into a chiral glass regime might characterize the field range exceeding $\mu_0 H \approx 2\text{ mT}$ in our randomly anisotropic 3D dipolar system.

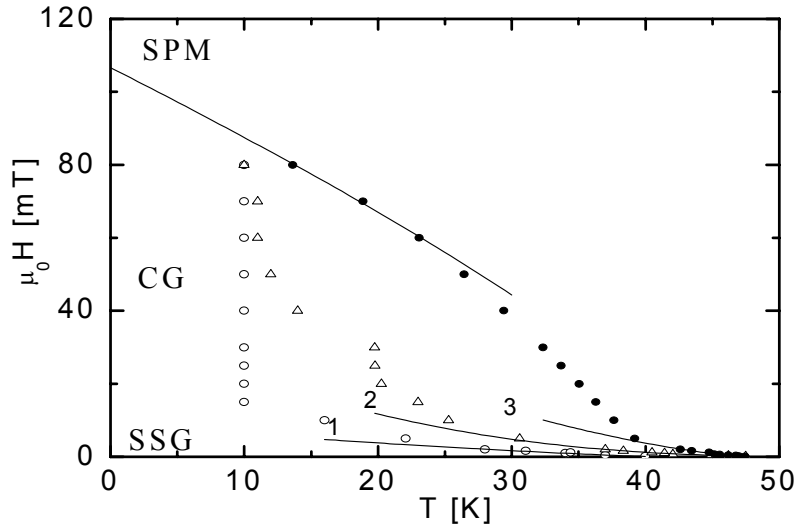


FIG. 5.31. Field dependence of $T(\mu_0 H)$ determined from data shown in Fig. 5.29(a) and (b) as "points of inflexion" (curve 1) and "points of intersection" (curve 2) of $\Delta M(\mu_0 H)$ vs. T , respectively, and as peaks of M^{ZFC} vs. T (curve 3), best fitted to Eq. (5.5) by solid lines for $\mu_0 H = 2\text{ mT}$ (see text). Tentative phases (SSG, CG and SPM) are indicated.

5.2.5. Conclusion

Our investigations clearly show that dipolar interactions and random distribution of anisotropy axes of single-domain ferromagnetic nanoparticles in the DMIM system $[\text{Co}_{80}\text{Fe}_{20}(0.9 \text{ nm})/\text{Al}_2\text{O}_3(3 \text{ nm})]_{10}$ give rise to a superspin glass state below $T_g \approx 44 \text{ K}$. This has been evidenced by the dynamic and static criticality studies. A Cole-Cole analysis of the *ac*-susceptibility reveals that the system exhibits a broad distribution of relaxation times in the superspin glass phase. The dynamics of the collective low temperature state has been studied by magnetization relaxation measurements employing various experimental protocols. Typical non-equilibrium features of an ordinary atomic spin glass such as aging, memory-imprint and rejuvenation are also observed in the superspin glass phase. The effect of an external magnetic field on the superspin glass state reveals an Almeida-Thouless line in the field range $0 \leq \mu_0 H \leq 2 \text{ mT}$, while a crossover into a chiral glass regime seems to occur in fields exceeding 2 mT.

5.3. DMIMs in the superferromagnetic limit

In this section we deal with the DMIM systems $[\text{Co}_{80}\text{Fe}_{20}(t_n)/\text{Al}_2\text{O}_3(3\text{nm})]_{10}$, where $t_n = 1.3$ and 1.4 nm. As it has already been discussed in section 5.2.1 and reported in Ref. [69], CoFe nanoparticles with average diameter $d \approx 3$ nm and inter-particle distances of 5 nm within a log-normal distribution width $\sigma_v = 2.7$ constitute the DMIM system with $t_n = 1.3$ nm. From the growth kinetics and in accordance with the observations on similar systems, e.g., Co/Al₂O₃ multilayers [68], slightly larger CoFe nanoparticles with closer inter-particle distances are expected to constitute the DMIM system with $t_n = 1.4$ nm. Accordingly, the average nearest-neighbor interaction will be enhanced as compared to that in the previously discussed DMIM system with $t_n = 0.9$ nm. This will have potent effects on the critical dynamics of the system. Indeed, as it will be shown here the properties are in striking contrast to those of the SSG state and rather refer to those of a superferromagnetic state.

5.3.1. The DMIM system $[\text{Co}_{80}\text{Fe}_{20}(1.3\text{nm})/\text{Al}_2\text{O}_3(3\text{nm})]_{10}$

Figure 5.32 presents the real and imaginary parts, χ' and χ'' , respectively, of the complex susceptibility, $\chi = \chi' - i\chi''$, vs. T of the DMIM $[\text{CoFe}(1.3\text{nm})/\text{Al}_2\text{O}_3(3\text{nm})]_{10}$ system measured in the frequency range $0.01 \leq f \leq 500$ Hz at an ac -field amplitude $\mu_0 H = 0.05$ mT after ZFC from $T = 300$ K.

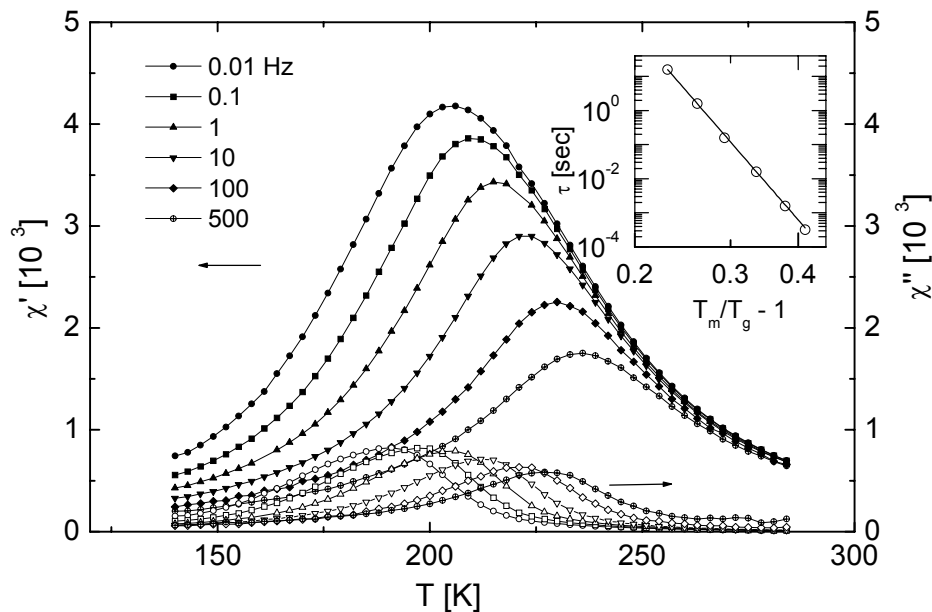


FIG 5.32. Temperature dependence of χ' (solid symbols) and χ'' (open symbols) taken with ac -amplitude $\mu_0 H = 0.05$ mT at frequencies as indicated in the figure. The inset shows $\tau = 1/2\pi f$ vs. $T_m/T_g - 1$ and best fit to a power law (solid line).

The observed frequency dependence of $\chi(T)$ appears rather similar to that of superspin glasses. However, a dynamic critical analysis performed according to the conventional critical power law, $\tau = \tau^* \left(\frac{T_m}{T_g} - 1 \right)^{-z\nu}$, where τ , τ^* , T_m , T_g , and $z\nu$ have identical meanings as described in section 5.2.2.1, yields $T_g = 166.5 \pm 8.5$ K, $\tau^* = 3.3 \pm 6.8) \times 10^{-11}$ s, and $z\nu = 18.3 \pm 5.3$. The best fitted power law is shown in the inset to Fig. 5.32. The value of τ^* appears too small to assign to a single superspin dynamics [85] and $z\nu$ appears rather large compared to that found in superspin glasses [30,31]. Furthermore, the frequency dependence of $\chi''(T)$ shows that its peak value increases with decreasing frequency, a tendency which is opposite to that observed in superspin glasses. These considerations suggest that the dynamics of the system cannot simply be put into the context of SPM to SSG transition.

In order to reveal the nonlinear response of the system we then studied the ac -field amplitude, $\mu_0 H_{ac}$, dependence of $\chi(T)$ and $\chi''(T)$. As shown in Fig. 5.33 both χ' and χ'' exhibit an extreme non-linearity with increase in $\mu_0 H_{ac}$. The data were recorded at an ac -frequency $f = 1$ Hz. An increase of $\mu_0 H_{ac}$ by a factor of 2 causes the peaks of $\chi(\chi'')$ vs. T to shift to lower T by 15(20) K and to shrink by factors of 1.4(1.35). This is in sharp contrast with a corresponding set of curves of the SSG referring to the DMIM system with $t_n = 0.9$ nm in Fig. 5.34.

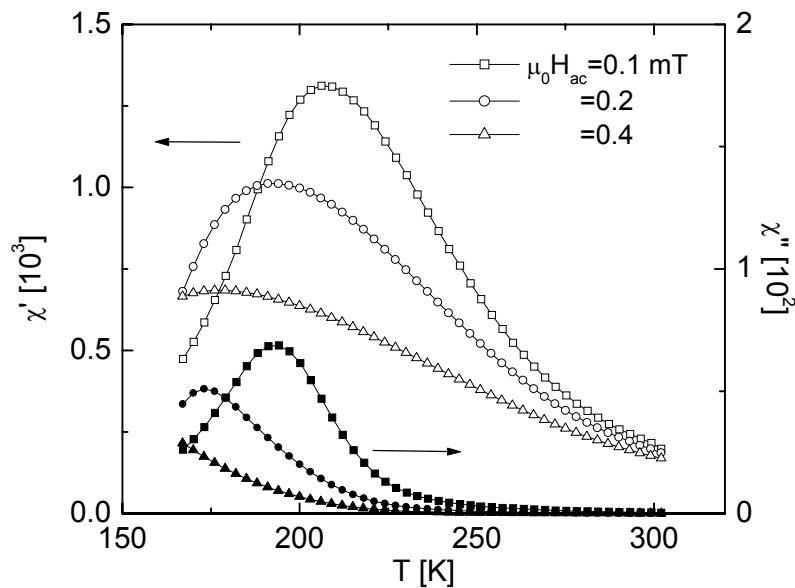


FIG. 5.33. χ' and χ'' vs. T taken at $f = 1$ Hz and different ac -amplitudes, $\mu_0 H_{ac}$, as indicated in the figure.

From Fig. 5.34(a), it is observed that the magnetic response is virtually linear in magnitude up to the highest ac -field amplitude, e.g. $\mu_0 H_{ac} = 0.4$ mT. This becomes evident when the ac -moment components m' (m'') measured at various values of $\mu_0 H_{ac}$ are plotted as χ' (χ'') with $\chi = m/\mu_0 H_{ac}$ as shown in Fig 5.34(b). Thus, the ac -susceptibility measurements in low enough fields $\mu_0 H_{ac} < 0.4$ mT allows studies of the inherent zero-field dynamics of the SSG.

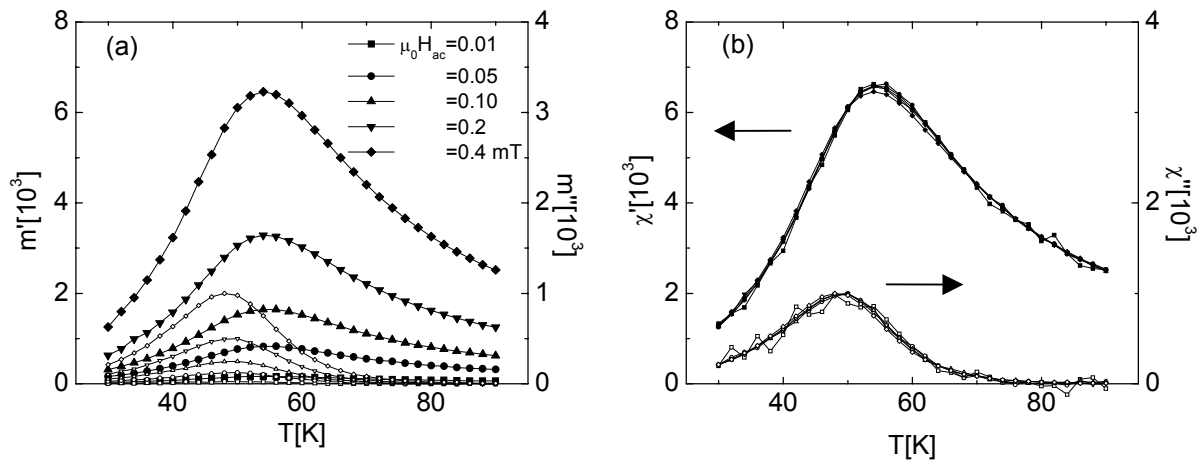


FIG. 5.34. (a) m' (solid symbols) and m'' (open symbols) vs. T measured at $f = 1$ Hz and different ac -field amplitudes $\mu_0 H_{ac}$ as indicated in the figure for the SSG sample $[\text{CoFe}(0.9\text{nm})/\text{Al}_2\text{O}_3(3\text{nm})]_{10}$. (b) χ' and χ'' vs. T .

The apparent distinction in the dynamic susceptibility of the two DMIMs, i.e., $t_n = 0.9$ and 1.3 nm is now clearly recognized. Obviously the above mentioned dynamic features of the SSG do no longer apply to the more concentrated DMIMs systems, since non-linearity has to be taken into account from the beginning. It can also be quite difficult to accurately determine the transition temperature from dynamic scaling analysis, since the divergence of the susceptibility is severely smeared due to strong non-linear field dependence. On the other hand, field, frequency, and temperature dependence of the ac-susceptibility and magnetization show certain signatures of a *superferromagnetic* (SFM) state [24,25,114] as will be discussed below. In remaining part of this section we will discuss the dc-field dependence of the ac-susceptibility and the noise in M vs. H isotherms in the DMIM system with $t_n = 1.3$ nm. In the next section we will discuss the

frequency and ac-amplitude dependence of the susceptibility in the DMIM system with $t_n = 1.4$ nm. Unlike the randomly disordered ground state of the SSG, the SFM ground state might exhibit “order due to disorder” [115]. Its exact nature is still to be explored both experimentally and theoretically. We tentatively consider the SFM state to be a consequence of dipolar coupling at closer packing of the magnetic nanoparticles. In addition, nonclassic interactions, e.g., super-exchange and Casimir interaction [19,20] cannot be excluded to be relevant as well.

The most interesting phenomenon is the occurrence of a double maximum structure in the *ac*-susceptibility when measured in a *dc*-bias field superimposed upon the *ac*-field. As shown in Fig. 5.35, $\chi'(T)$ and $\chi''(T)$ measured in a *dc*-bias field $\mu_0 H = 0.6$ mT exhibit polydispersivity at low temperatures and a dispersionless background at higher temperatures. Furthermore, it is noticed that the dispersionless part is unrelated to the loss function, χ'' . While the high temperature features can be considered as indications of ferromagnetic correlations between the superspins, the low temperature polydispersivity can be discussed within the framework of two scenarios. First, it appears almost indistinguishable from an ordinary spin glass profile and may characterize a transition of the SFM phase to a reentrant superspin glass (RSSG) phase. Second, the polydispersivity may characterize the response of the domain walls of the SFM domain state.

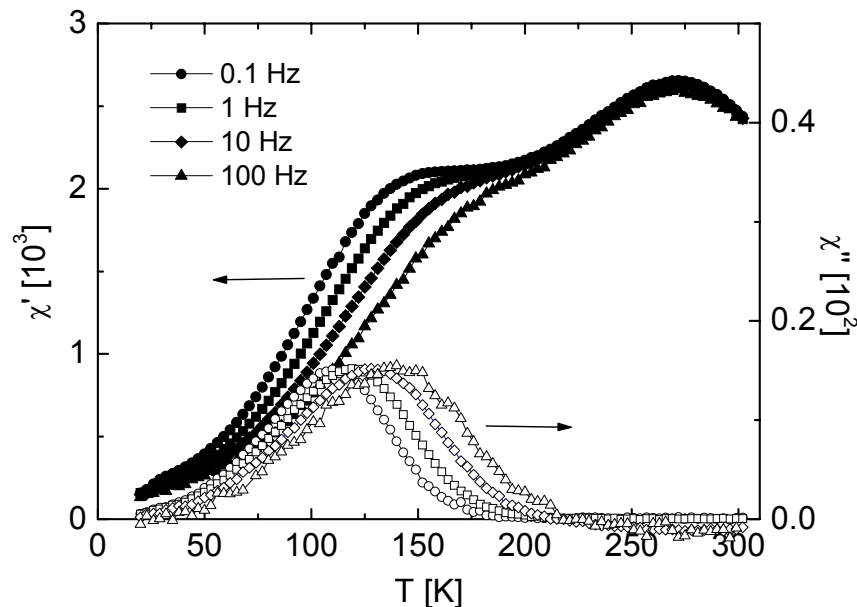


FIG. 5.35. χ' and χ'' vs. T measured at an *ac*-field amplitudes $\mu_0 H_{ac} = 0.4$ mT and frequencies f as indicated in the figure of the SSG $[\text{CoFe}(1.3\text{nm})/\text{Al}_2\text{O}_3(3\text{nm})]_{10}$.

To further characterize the SFM state we compare the *ac*-susceptibility measured in a zero-field condition to that in a *dc*-bias field $\mu_0 H = 0.04 \text{ mT}$. The data obtained at an *ac*-amplitude $\mu_0 H_{ac} = 0.05 \text{ mT}$ and frequencies in the range $0.01 \leq f \leq 10 \text{ Hz}$ are presented in Fig. 5.36. Apart from large smearing effects, the evolution of two maxima in χ' due to the bias field is clearly observed. Furthermore, in contrast to the result shown in Fig. 5.35, the polydispersive contribution in Fig. 5.36 is prevailing over the dispersionless background when the bias field is relatively weak, e.g., 0.04 mT in Fig. 5.36 compared to 0.6 mT in Fig. 5.35. It hints at a strong influence of the bias field on the ordering process.

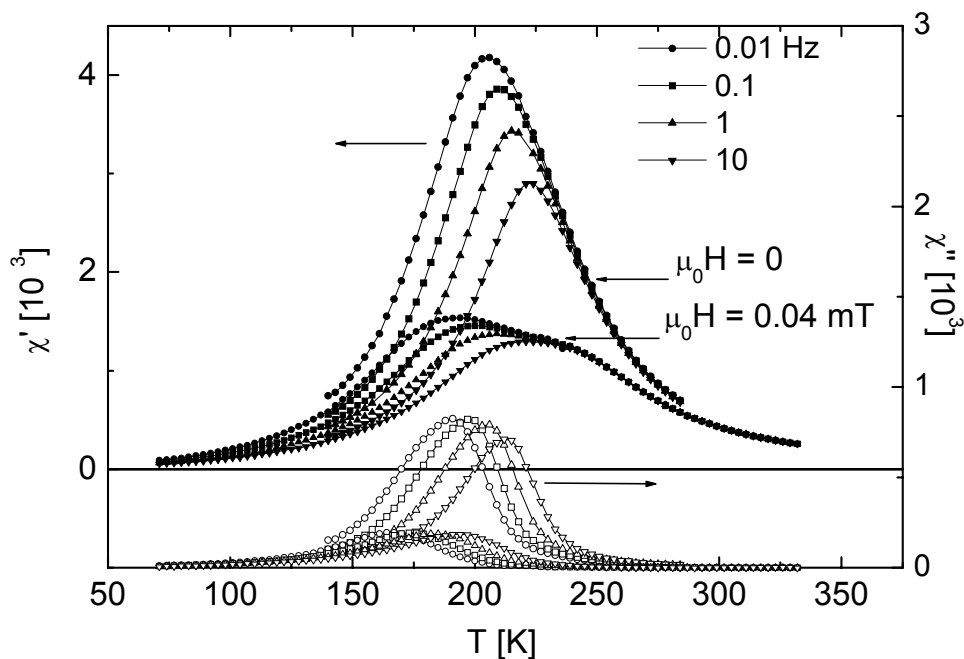


FIG. 5.36. χ' and χ'' vs. T measured at various frequencies f as indicated in the figure and two different *dc*-fields $\mu_0 H = 0$ and 0.04 mT superimposed on an *ac*-field amplitude $\mu_0 H_{ac} = 0.05 \text{ mT}$.

Figure 5.37 shows $\chi'(T)$ and $\chi''(T)$ in different *dc*-fields, $\mu_0 H = 0, 0.04, 0.2,$ and 0.6 mT , taken after zero-field cooling (ZFC) from $T = 300 \text{ K}$. The *ac*-frequency, $f = 10 \text{ Hz}$, and the *ac*-field amplitude, $\mu_0 H_{ac} = 0.05 \text{ mT}$, are kept constant. In finite *dc*-field two observations are made. First, the dispersive peak at T_m shifts to lower temperatures (broken arrows). In view of the first scenario proposed above, it corresponds to findings on other spin glass systems. The field dependence of a glass transition temperature is

expected to follow the so-called Almeida-Thouless line [105]. Second, the high-temperature peak frequency independent peak of $\chi'(T)$, called the SFM transition temperature T_{SFM} (solid arrows) shifts to higher temperatures with increasing bias field. The field dependence of T_{SFM} is shown in Fig. 5.38 (b). The extrapolated value is $T_{\text{SFM}}(H \rightarrow 0) \approx (230 \pm 5)$ K. The field induced shift of T_{SFM} may be tentatively attributed to two origins. First, the SFM ordering temperature may substantially be enhanced by virtue of the aligning field, when considering a non-collinear domain-like ground state. Second, when taking into account tunneling exchange interaction, it has been shown [116] that the exchange constant increasing at increasing field. Interestingly the imaginary part, $\chi''(T)$, becomes strikingly flattened with increasing dc field and shows no additional feature at T_{SFM} . This proves, together with the frequency independence of the SFM peak, that this peak cannot simply be attributed to superparamagnetic blocking or spin glass freezing.

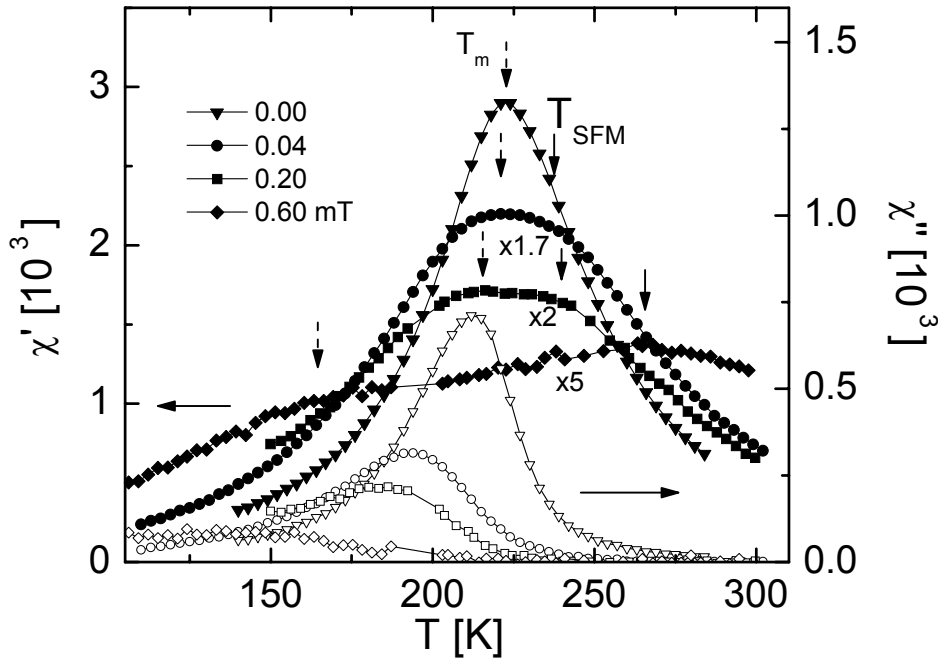


FIG. 5.37. $\chi'(T)$ and $\chi''(T)$ of the $[\text{CoFe}(1.3\text{nm})/\text{Al}_2\text{O}_3(3\text{nm})]_{10}$ sample in different dc -biasing fields, $\mu_0 H = 0, 0.04, 0.2,$ and 0.6 mT (± 0.03 mT) at constant ac -frequency $f = 10$ Hz and ac -amplitude $\mu_0 H_{\text{ac}} = 0.05$ mT. $\chi'(T)$ and $\chi''(T)$ for fields $\mu_0 H > 0$ were multiplied by factors of 1.7, 2 and 5, respectively. The vertical arrows mark the positions of the two peaks, T_m (broken) and T_{SFM} (solid), in the χ' data.

In order to study the SFM transition more thoroughly we measured magnetization isotherms within the field interval, $-2.5 \leq \mu_0 H \leq 2.5$ mT, in steps of 0.005 mT near to the expected transition temperature, $T_{\text{SFM}}(\mu_0 H = 0)$ (Fig. 5.38 (a)). At $T = 230$ K one clearly observes strong fluctuations near $\mu_0 H = 0$. The origin of these fluctuations is *not* the typical noise due to a vanishing signal at $M \approx 0$, since the measurement, e.g., at $T = 250$ K does not show this feature. The fluctuations can be studied quantitatively by calculating the integral noise, $\delta = \frac{1}{\Delta H} \int (M - M_{sm})^2 dH$, for several curves, $220 \text{ K} \leq T \leq 260 \text{ K}$, where $M_{sm} = M_{sm}(H)$ is the smoothed magnetization curve. The result is shown in Fig. 5.38 (c). One finds a relatively sharp peak at $T \approx (230 \pm 2)$ K from two independent series of measurements. This corresponds perfectly to the value found by extrapolating $T_{\text{SFM}}(H)$ to $\mu_0 H = 0$ (Fig. 5.38 (b)). Remarkably the strong fluctuations around T_{SFM} (Fig. 5.38 (a)) occur on a time scale of several seconds, considering the time of about $\tau \approx 10$ s for obtaining one data point. This hints at critical slowing down near the SFM phase transition, which seems to be enhanced due to the superspin nature ($\mu \approx 5000 \mu_B$). Obviously the SFM transition occurs in zero-field at $T_{\text{SFM}} \approx 230$ K, where the system orders like a soft ferromagnet forming SFM correlations [24,25] of closely packed granules. The extent and stability of the network can be controlled by the dc field. Here we propose that the observed noise reflects the time dependent stabilization of the underlying SFM domain state which is subject to slow relaxation due to random domain wall pinning [25] (see also section 5.3.2).

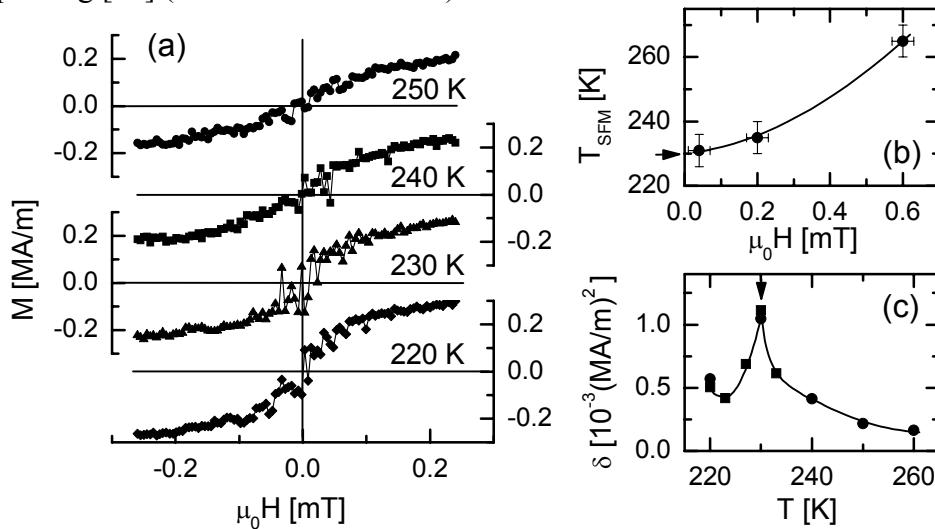


FIG. 5.38. (a) Magnetization vs. *dc* field at different temperatures, $T = 220, 230, 240$ and 250 K. (b) Peak positions, T_{SFM} , from Fig. 5.37. The arrow marks the extrapolated value, $T_{\text{SFM}}(H \rightarrow 0) \approx 230$ K. (c) Integrated square noise, $\delta(T)$, from two independent series of $M(H)$ isotherms (solid circles and squares). Solid lines are guides to the eye.

5.3.2. The DMIM system $[\text{Co}_{80}\text{Fe}_{20}(1.4\text{nm})/\text{Al}_2\text{O}_3(3\text{nm})]_{10}$

Figure 5.39 shows the temperature variation of thermoremanent magnetization the DMIM system $[\text{Co}_{80}\text{Fe}_{20}(1.4\text{nm})/\text{Al}_2\text{O}_3(3\text{nm})]_{10}$. The data are collected after cooling the system from $T = 400$ K in a magnetic field $\mu_0 H = 0.45$ mT to $T = 5$ K and switching off the field. It is observed that the magnetization decays linearly at $T > 250$ K, where a linear extrapolation to $M = 0$ yields a critical temperature $T_c \approx 410$ K.

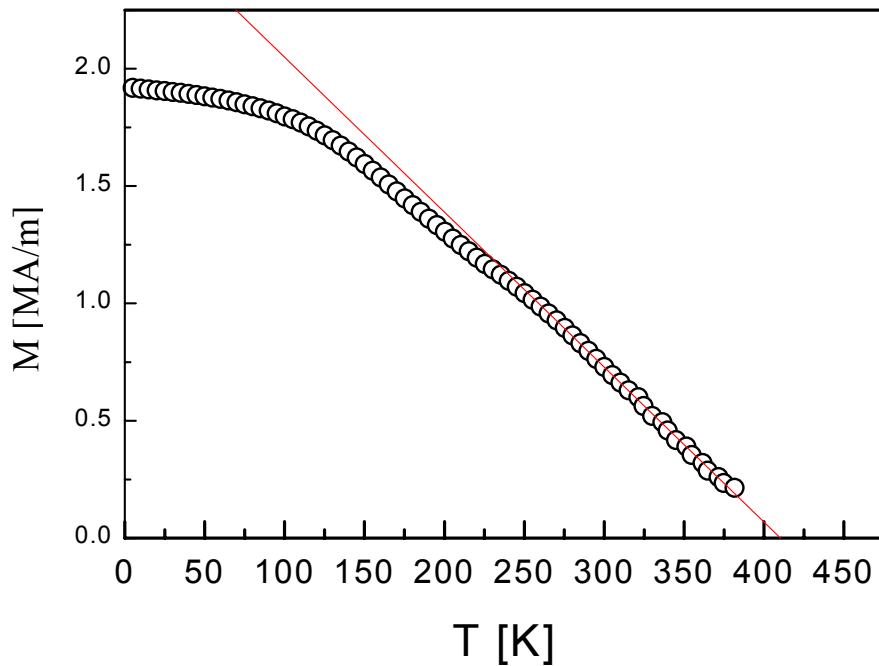


FIG. 5.39. Temperature dependence of the field-cooled magnetization of the DMIM system $[\text{Co}_{80}\text{Fe}_{20}(1.4\text{nm})/\text{Al}_2\text{O}_3(3\text{nm})]_{10}$. The straight line is a linear fit.

Figure 5.40 shows in- and out-of phase components, χ' and χ'' , respectively, vs. T of the complex susceptibility, $\chi = \chi' - i\chi''$, at two different ac -field amplitudes $\mu_0 H_{ac} = 0.05$ mT (a) and 0.2 mT (b). The data were obtained after carefully demagnetizing the sample at $T \approx 400$ K and then zero-field-cooling from room temperature. Comparing χ' and χ'' at the two ac -amplitudes, it is observed that they exhibit strong non-linearity. Their downward shift on the temperature scale and peak depression upon increasing $\mu_0 H_{ac}$ are rather similar to the corresponding curves of the DMIM system with $t_n = 1.3$ nm (Fig. 5.33). An increase of $\mu_0 H_{ac}$ by a factor of 4 causes the peaks of $\chi(\chi')$ vs. T to shift to lower T by 30(50) K and to shrink by factors of 5(3).

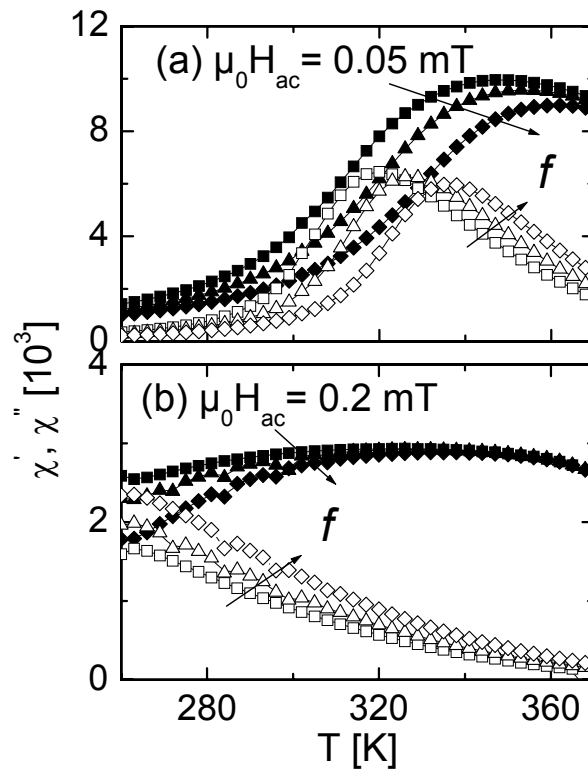


FIG. 5.40. χ' (solid symbols) and χ'' (open symbols) vs T of $[\text{Co}_{80}\text{Fe}_{20}(1.4\text{nm})/\text{Al}_2\text{O}_3(3\text{nm})]_{10}$ taken with ac -amplitudes $\mu_0 H_{ac} = 0.05$ (a) and 0.2mT (b) at frequencies $f = 0.01, 0.1,$ and 1 Hz. The arrow directions indicate increasing frequency.

The unusual appearance of the SFM polydispersity is most clearly recognized in the Cole-Cole diagrams, χ'' vs. χ' [25] as shown in Fig. 5.41 for $T = 380$ (1), 350 (2), 320 (3), and 260 K (4), with $\mu_0 H = 0.5$ [(Fig. 5.41(a))] and 0.05 mT [Fig. 5.41(b)]. At highest frequencies, $f \rightarrow 1$ kHz (i.e., $\chi' \rightarrow 0$), the diagrams start either with proportionalities, $\chi' \propto \chi''$, or with horizontal spectrum, $\chi'' = \text{constant}$ [Fig. 5.41(a) and (b); broken lines]. At increasing χ' the slope $d\chi''/d\chi'$ first increases and - after passing a point of inflexion and a peak - the diagrams finally convert into classic Cole-Cole semi-circles as $f \rightarrow 10\text{mHz}$ (broken lines fitted to curves 1 and 2), thus revealing monodispersivity.

In accordance with the conjectured SFM superspin ordering scheme with an inherent domain structure the salient features of the ac -susceptibility response have been attributed to domain wall dynamics under the constraint of random pinning forces [116].

Within this model, which was recently also treated theoretically, the above mentioned spectral behavior of the SFM system can be classified into four regimes: (i) relaxation regime, where $\chi'' = \text{constant}$, (ii) irreversible creep regime, where $\chi'' \propto \chi'$, (iii) easy slide or viscous regime, where $\chi'' = \tan(\beta\pi/2)(\chi' - \chi_\infty)$ with β being the polydispersive exponent, and (iv) switching regime, where Debye-type linear response of the susceptibility, $\chi_{ac} = \chi_\infty / (1 + i\omega\tau)$ is observed.

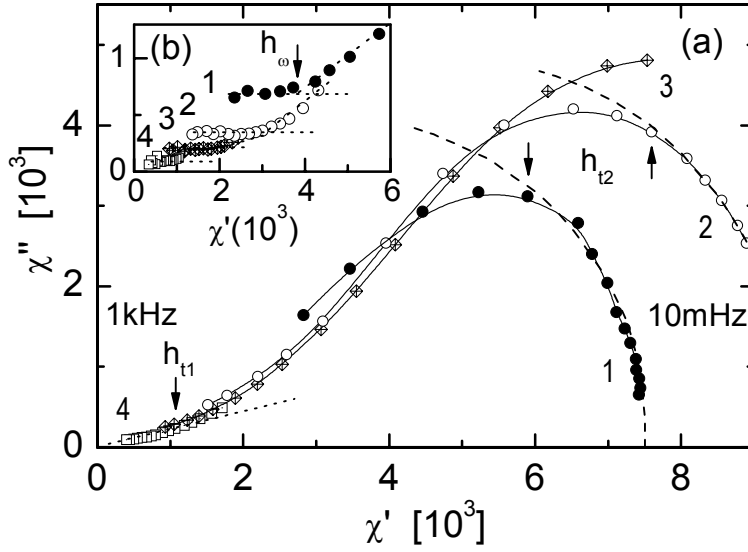


FIG. 5.41. Susceptibility components χ'' vs. χ' measured at ac -amplitudes $\mu_0 H_{ac} = 0.05$ (a) and 0.55 mT (b) at $10\text{mHz} \leq f \leq 1$ kHz (data points from right to left, connected by interpolating solid lines) at $T = 380$ (1), 350 (2), 320 (3) and 260 K (4). Phase transition features (see Ref. 25) are marked by arrows.

In the relaxation regime the spectrum has the appearance of “white noise”. It corresponds to a constant power spectrum (via the fluctuation dissipation theorem) and is compatible to a power law dependence $\chi' \propto \omega^{-\beta}$ as confirmed experimentally [117]. This behavior is typical of the reversible relaxation of pinned domain wall segments with quasicontinuous distribution of Debye-type spectra [118].

The creep and the sliding regime can be understood within the framework of a phenomenological model [25] as follows. Let us consider a simple picture of up and down oriented stripe domains with initial uniform width D and magnetization M_s as shown in

Fig. 5.42. A displacement of the domain wall by a harmonic excitation $H(t) = H_0 \exp(i \omega t)$ along the coordinate $x(t)$ will yield a time dependent magnetization,

$$M(t) = (2M_S / D)x(t) \quad (5.6).$$

The rate of the domain wall motion can be written as

$$\dot{M}(t) = (2M_S / D)\mu_w H(t), \quad (5.7)$$

where μ_w is the wall mobility and is related to the wall velocity by $dx/dt = \mu_w H(t)$. Eq. (5.7) can be written as

$$\dot{M}(t) = (2\mu_w M_S / D + i\omega\chi_\infty)H_0 \exp(i\omega t), \quad (5.8)$$

where the second term refers to the “instantaneous” reversible domain wall response occurring on shorter time scales and $M_\infty = \chi_\infty H(t)$ describes a dispersionless background.

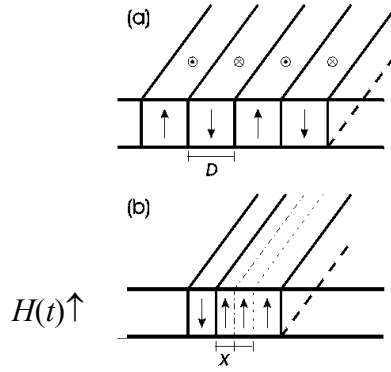


FIG. 5.42. (a) Schematic drawing of up and down stripe domains of width D . (b) Displacement of domain wall by an excitation $H(t)$.

Taking the time integral of Eq. (5.8), one obtains

$$M(t) = \left(\frac{2\mu_w M_S}{i\omega D} + \chi_\infty \right) H_0 \exp(i\omega t) \equiv \left(\frac{\chi_w}{i\omega\tau_w} + \chi_\infty \right) H_0 \exp(i\omega t), \quad (5.9)$$

where $\chi_w / \tau_w \equiv 2\mu_w M_S / \mu_0 D$ and the complex susceptibility

$$\chi^* = \chi' - i\chi'' = \chi_\infty + \frac{\chi_w}{i\omega\tau_w}. \quad (5.10)$$

Owing to the distribution of different domain widths, viz. D values, one expects polydispersivity, which is mimicked by a correlation exponent $\beta < 1$,

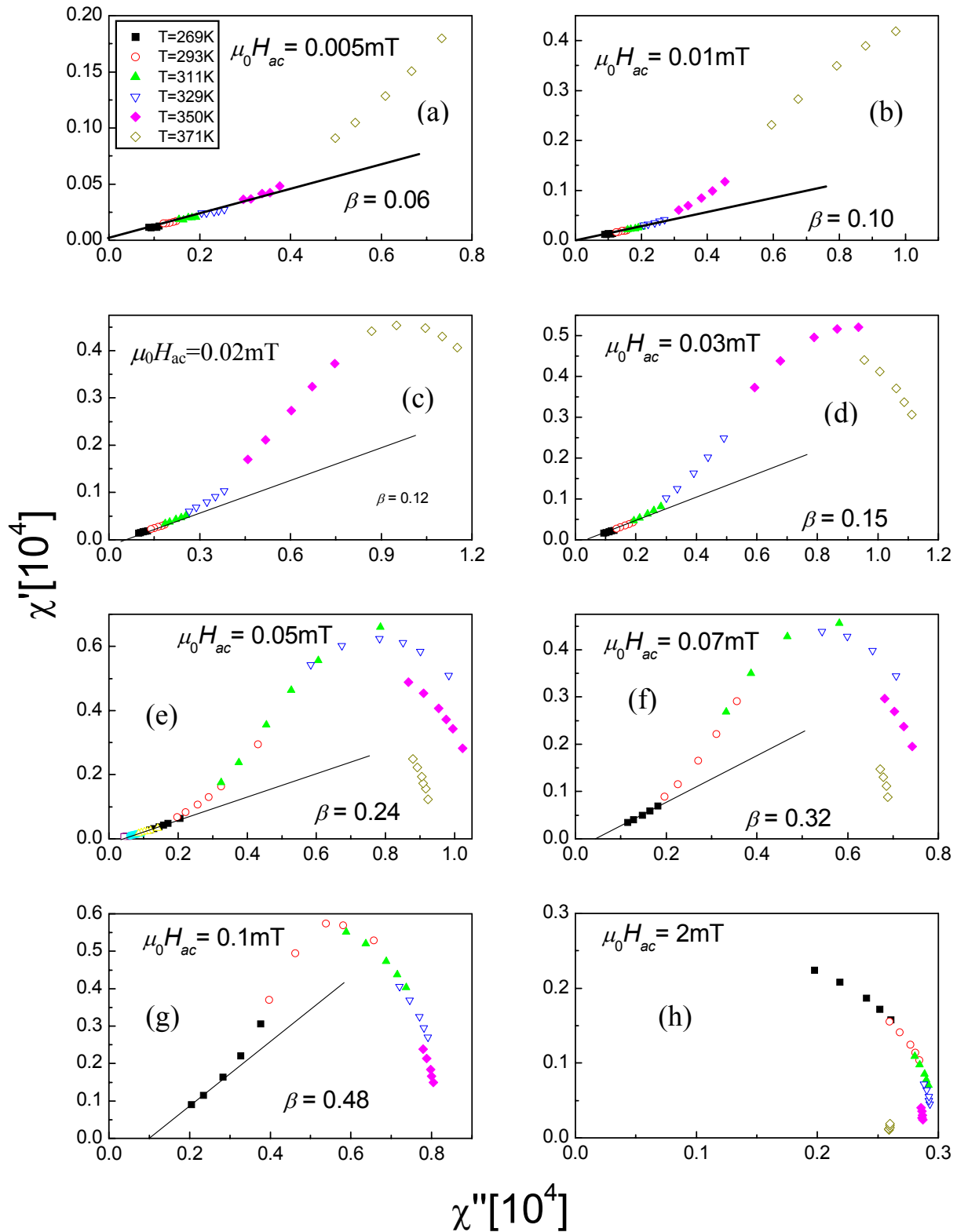


FIG. 5.43. Cole-Cole plots, χ'' vs. χ' , measured at ac -amplitudes, $\mu_0 H_{ac}$, as indicated in each plot and frequencies $10 \text{ mHz} \leq f \leq 1 \text{ kHz}$ at temperatures $T = 369 - 371$. The straight lines are fit to $\chi'' = \tan(\pi\beta/2)(\chi' - \chi_\infty)$.

$$\chi^* - \chi_\infty = \frac{\chi_\infty}{(i\omega\tau_{eff})^\beta}. \quad (5.11)$$

Multiplying Eq. (5.11) with its complex conjugate and equating the real and imaginary parts, one obtains

$$\chi' = \chi_\infty (1 + \cos(\beta\pi/2)) / (\omega\tau_{eff})^\beta \quad (5.12)$$

and

$$\chi'' = \chi_\infty \sin(\beta\pi/2) / (\omega\tau_{eff})^\beta \quad (5.14)$$

It should be noted that

$$\chi'' / (\chi' - \chi_\infty) = \tan(\beta\pi/2) \quad (5.15)$$

is independent of ω and T .

As shown in Fig 5.43, fits of $\chi'' = \tan(\pi\beta/2)(\chi' - \chi_\infty)$ to χ' vs. χ'' data show that the value of β increases with increasing $\mu_0 H_{ac}$. Furthermore, it is observed that upon decreasing ω at a given T and $\mu_0 H$, the linearity does no longer hold for above a threshold value, i.e., h_{t1} in Fig. 5.41 (a). Tentatively, it is assumed that the sliding regime is entered above this depinning threshold, where χ'' is expected to rise very steeply.

Complete switching [Fig. 5.43 (h)] experienced by ac-susceptibility corresponds to Avrami-Fatuzzo-type nucleation and growth processes [119] approximately obeying first-order rate equations

$$\frac{dM}{dt} = \tau^{-1} [\mp M_s - M(t)], \quad (5.16)$$

with solutions $M(t) = \mp M_s [1 - 2 \exp(-t/\tau)]$, where alternative signs hold for consecutive half periods. M_s and τ are the saturation magnetization and an averaged relaxation time, respectively. The corresponding susceptibility in the linear response regime is Debye-type, $\chi^* = \chi_\infty / (1+i\omega\tau)$, and yields a perfect Cole-Cole semicircle, χ'' vs χ' . Hence, the broken circles fitted to curves 1 and 2 in Fig. 5.41 (a) refer to those frequencies, at which the domain wall proceeds from one sample boundary to the other in the dynamic single domain wall model [120].

5.4. Conclusion

In this Chapter, we have demonstrated that the magnetic properties of DMIMs $[\text{Co}_{80}\text{Fe}_{20}(t_n)/\text{Al}_2\text{O}_3(3\text{nm})]_{10}$ strongly depend on the nominal thickness t_n of the CoFe layer. As described in section 5.2, at $t_n = 0.9$ nm a transition occurs from superparamagnetic to superspin glass state. Very probably the occurrence of this transition is a consequence of the pertinent disorder (random site and random anisotropy) and frustration (due to long-range and anisotropic character of dipole-dipole interaction). When increasing the nominal thickness t_n , a crossover to a superferromagnetic state is believed to occur at $t_n \geq 1.05$ nm [24]. The nature of the superferromagnetic state has been investigated in samples with $t_n = 1.3$ and 1.4 nm. The features of the superferromagnetic state have been evidenced by the field dependence of the ac -susceptibility in the $t_n = 1.3$ nm system and by a Cole-Cole analysis of the ac -susceptibility in the $t_n = 1.4$ nm system. The magnetic phase diagram of the DMIM systems is shown in Fig. 5.44.

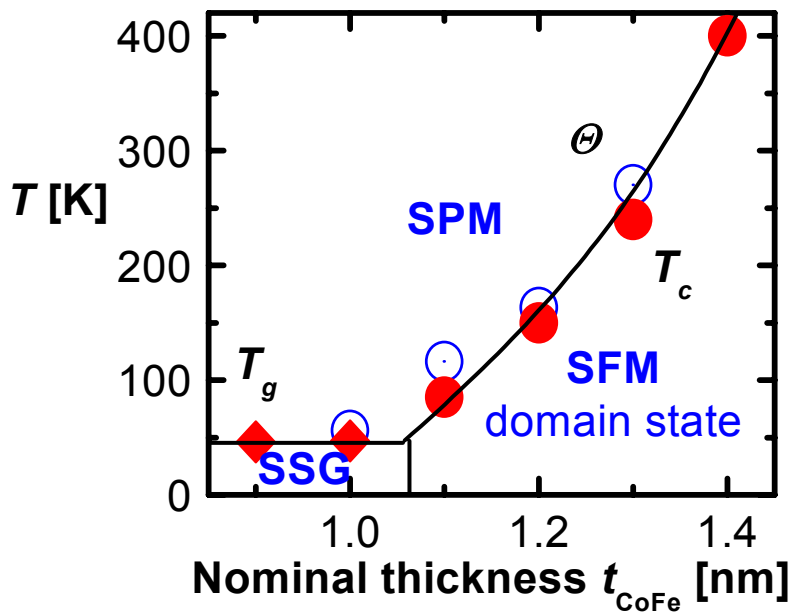


FIG. 5.44. Magnetic phase diagram of CoFe/Al₂O₃ DMIMs vs. nominal CoFe thickness t_n (shown in the figure as t_{CoFe}). T_g is the glass transition temperature (diamonds), θ the Curie temperature (dot centered circles) and T_c the critical temperature for the superferromagnetic transition (solid circles).

Chapter 6

Properties of a granular FeCl₂-Fe heterostructure

6.1. Introduction

So far we were concerned with the physics of FM nanoparticles embedded in an insulating diamagnetic matrix. In these systems, the interaction of the nanoparticles with the host matrix was neglected. In contrast, the nanoparticle-matrix interaction becomes significant when the diamagnetic matrix is replaced, e.g. by an antiferromagnetic (AF) one. Indeed, the first study of fine Co particles embedded in their native oxide led to the discovery of unidirectional anisotropy which gives rise to an exchange bias (EB) effect of the hysteresis loop due to exchange coupling at the FM-AF interface [82]. The phenomenon was later on observed in many other FM-AF fine particle systems and in continuous films consisting of sandwiched AF and FM thin layers [121]. Recent experiments have confirmed that the spin alignment of FM spins in these exchange-coupled systems is determined by the direction of the excess spins in the underlying AF layer giving rise to pinning of the ferromagnet and, hence, to exchange bias [122].

On the other hand, also the retroactivity of the FM nanoparticles onto the AF matrix may be of interest. Most spectacular effects are expected, if the AF intra-matrix exchange is weak compared to its interaction with the embedded FM nanoparticles. It will be due to the combined effects of exchange coupling at the particle-matrix interface and of the Zeemann coupling of the FM dipolar stray fields with the AF matrix.

This chapter will report on the experimental investigation of a granular FeCl₂-Fe heterostructure where related effects are most evidently observed [123,124]. As discussed in Chapter 4, FeCl₂ is an Ising-type AF system whose inter-layer AF exchange coupling ($J/k_B = -0.18$ K) is approximately twenty times weaker than the intra-layer FM exchange coupling between Fe²⁺ ions ($J_1/k_B = 3.9$ K). Apart from direct exchange coupling at the interface of the Fe granules and the nearest neighbor Fe²⁺-ions of FeCl₂ matrix, the dipolar stray-fields of the granules will play a key role in determining the magnetic properties of the system. Evidence of exchange coupling also emerges from the

observation of a shift of the field-cooled (FC) hysteresis loop below the Néel temperature of FeCl_2 matrix. It will be shown that under the combined effects of these two mechanisms, giant metamagnetic moments containing Fe granules as nucleation cores are observed. Moreover, the giant moment clusters can be shown to grow at the expense of the AF regions upon repeated field-cooling cycles. Temperature and frequency dependent *ac*-susceptibility measurements corroborate the above mechanism and hint at the presence of a polydispersive surface layer attached to the giant moment clusters.

6.2. Structural properties

Structural characterization of the FeCl_2 -Fe granular film was carried out by *ex situ* X-ray diffraction (XRD) (Philips PW1730) using $\text{Cu-K}\alpha$ radiation ($\lambda = 0.15418$ nm). As described in Chapter 4 the film was grown on a sapphire ($11\bar{2}0$) substrate. Fig. 1 shows a comparison of the XRD patterns of the FeCl_2 -Fe film to that of the substrate. Analysis of the XRD data by using the rhombohedral unit cell parameters of FeCl_2 reveals that (112) planes of FeCl_2 coincide with ($11\bar{2}0$) planes of the substrate. Indeed, the presence of narrow and high (112) and (224) FeCl_2 lines at the Bragg angles $2\theta = 37.83^\circ$ and 80.85° supports (112) textured growth. Simultaneously, (112) and (224) FeCl_2 lines originating from $\text{Cu-K}\beta$ radiation are also observed at $2\theta = 34^\circ$ and 71.4° in the film diffractogram. Furthermore, some tendency ($\approx 1\%$) towards (111) orientation of FeCl_2 is observed. The analysis suggests polycrystallinity of FeCl_2 . Using Scherrer's formula [76],

$$D = \frac{0.9\lambda}{\beta \cos \theta}, \quad (6.1)$$

where λ is the wavelength of $\text{Cu-K}\alpha$ radiation, β the full width at half maximum intensity of the peak, and θ the diffraction angle, the average crystalline size D was found to be $D_{\text{FeCl}_2} \approx 80$ nm.

Analysis of the spectrum gives only a minor indication of the presence of oriented Fe granules by a Bragg peak at $2\theta = 66^\circ$ referring to (300) planes. A rough estimate from Scherrer's formula yields $D_{\text{Fe}(300)} = 10$ nm ($\beta = 2.5^\circ$) immediately after the first warming up to room temperature (virgin sample). Their presence has been evidenced more convincingly from the magnetization data as will be shown later.

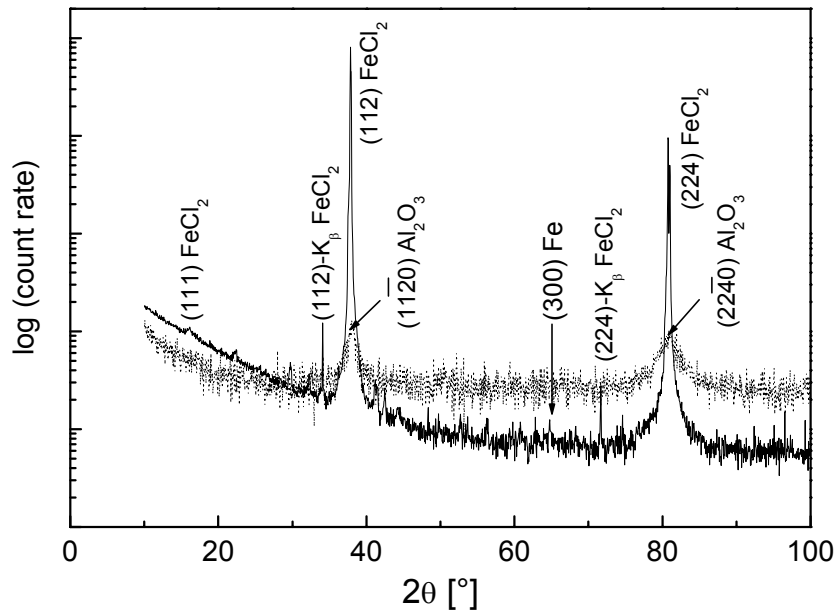


FIG. 6.1 Comparison of the room temperature XRD patterns of a FeCl₂-Fe sample (solid line) to that of the sapphire substrate (dotted line) indicating some prominent Bragg peaks.

6.3. Magnetic properties

The magnetic properties of the granular system were investigated by the use of SQUID magnetometry and *ac*-susceptometry (MPMS-5S, Quantum Design). Figure 6.2(a) shows the in- and out-of-phase components, χ' and χ'' , respectively, of the *ac*-susceptibility measured on the virgin sample at a frequency $f = 20$ Hz and an *ac*-amplitude $\mu_0 H_{ac} = 0.4$ mT. While no evidence of any AF features is present in χ' , a broad maximum of χ'' around the anticipated Néel temperature gives a clear indication of the presence of FeCl₂ in the film. Similarly, a dc-magnetization measurement as shown in Fig. 6.2(b) involving an external magnetic field $\mu_0 H = 20$ mT confirms the presence of FeCl₂ with a sharp peak at $T_N \approx 22$ K and a rapid drop by $\approx 50\%$ with a minimum at $T \approx 12$ K. It should be noticed that T_N of our granular film is slightly below the bulk value of 23.7 K. Most remarkably, however, is a steep increase at low temperatures, $T < 10$ K. It reminds of paramagnetic loose spins often encountered in disordered antiferromagnets, but probably refers to an

extra magnetization due to the Fe nanoparticles. Their role becomes clearer when considering the heterostructure after aging at room temperature during more than 3 days.

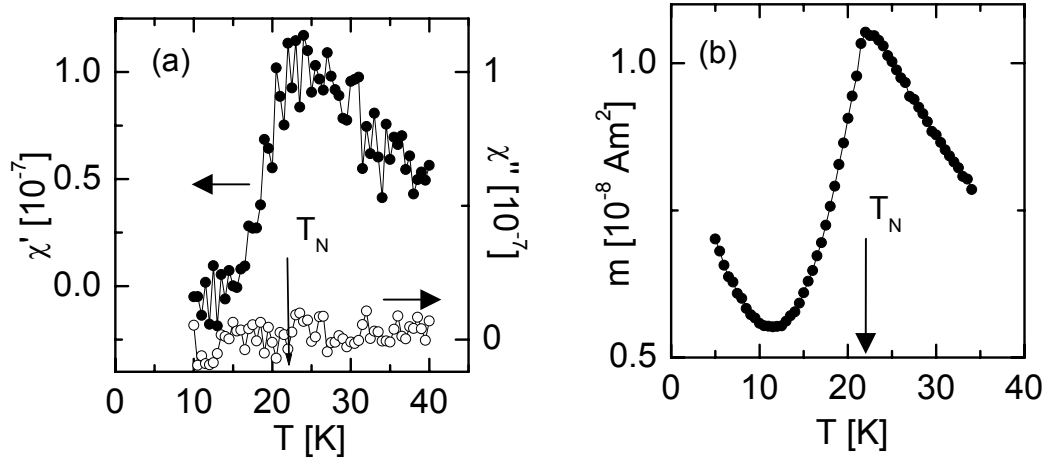


FIG. 6.2. (a) ZFC ac-susceptibility vs. temperature T at an ac-amplitude $\mu_0 H = 0.4$ mT and frequency $f = 20$ Hz after few hours of exposure to room temperature. (b) ZFC magnetization vs. T involving an external field $\mu_0 H = 20$ mT after few hours of exposure to room temperature. The arrows indicate the Néel temperature T_N .

In order to evidence the presence of the Fe particles in the “aged sample” we utilize the criterion of irreversibility between ZFC-FH and FC magnetizations, $m^{\text{ZFC-FH}}$ and m^{FC} , respectively, at the blocking temperature T_b . We identified it from the $m^{\text{ZFC-FH}}$ vs. m^{FC} irreversibility occurring at $T_b \approx 320$ K as shown in Fig. 6.3. Clearly, this high value is incompatible with the XRD analysis on the virgin sample, since it corresponds to particles of diameter $D_{\text{Fe}} = 16$ nm as calculated from the Arrhenius-Néel-Brown blocking ansatz

[12,13], $\tau = \tau_0 \exp\left(\frac{KV}{k_B T}\right)$, when associating an observation time of 100s to our

measurement. Here we have used $\tau_0 = 10^{-9}$ s and the value of the anisotropy constant $K = 5 \times 10^4$ Jm⁻³ for bulk Fe. Obviously, the result hints at coarse graining of the Fe granules in the early stage of our experiments which finally end up at $D_{\text{Fe}} = 16$ nm. It is important to mention that all measurements carried out afterwards and presented in rest of the chapter were reproducible.

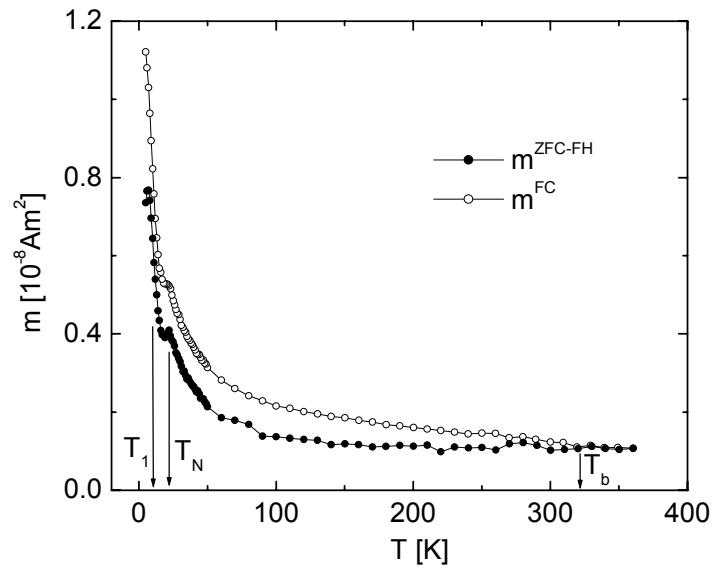


FIG: 6.3. $m^{\text{ZFC-FH}}$ and m^{FC} vs. T indicating the blocking temperature T_b , the Néel temperature T_N and the point of inflexion T_1 . The data are taken at an applied magnetic field $\mu_0 H = 10$ mT.

Furthermore, drastic changes in the properties of the aged sample are observed below $T < 15$ K. While the AF features, viz. a peak at the ordering temperature $T_N \approx 22$ K and a Curie-Weiss (CW)-type decrease at $T > T_N$ are retained, a pronounced peak at $T \approx 8$ K appears in $m^{\text{ZFC-FH}}$. This low temperature peak at $T \approx 8$ K arises due to the poor in-field alignment of randomly oriented blocked Fe moments which is partially lifted upon heating and gives rise to a decay at $T > 8$ K. Furthermore, a large enhancement of m^{FC} arises in the AF regime below $T = 15$ K. An accelerated increase of m^{FC} below the point of inflexion at $T_1 = 10$ K and saturation tendencies as $T \rightarrow 0$ (see below) seem to reflect metamagnetism of the FeCl_2 environment beyond the spin-flip transition [125], which is induced by the field-aligned Fe granules.

Measurements of $m^{\text{ZFC-FH}}$, m^{FC} , and m^{TRM} involving an external field $\mu_0 H = 10$ mT have been carried out under different starting conditions. The data shown in the main panel of Fig. 6.4 were obtained by starting in zero field at $T = 290$ K $< T_b$. In this case, the sample was in a premagnetized state, since the virgin sample was exposed to a magnetic field of 20 mT during a previous measurement shown in Fig. 6.2, after which these data

were recorded without exceeding T_b . A similar set of measurements, but after a careful demagnetization procedure at $T = 290$ K, is shown in Fig. 6.5. In the demagnetization procedure, the sample is subjected to saturation in a field of 2 T which is then reduced to zero in an alternated cycle (“saturation-reverse-zero”). This procedure produces random orientations of the Fe moments and is considered to be equivalent to ZFC from above T_b .

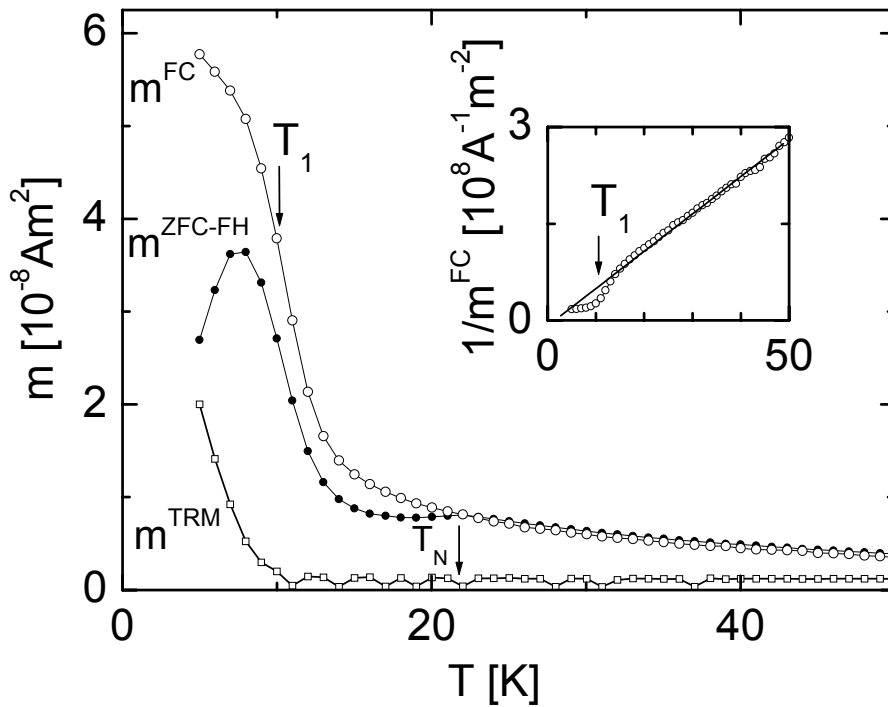


FIG. 6.4. $m^{\text{ZFC-FH}}$, m^{FC} , and m^{TRM} vs. T involving an external field $\mu_0 H = 10$ mT after ZFC from $T = 290$ K. The arrows indicate the corresponding Néel temperature, $T_N \approx 22$ K, and the point of inflexion, $T_1 \approx 10$ K, of m^{FC} . The inset shows $1/m^{\text{FC}}$ vs. T and Curie-Weiss-type fit (straight line).

It is remarked that m^{FC} in Fig. 6.4 shows no anomaly at the AF transition, which is more clearly seen when plotting $1/m^{\text{FC}}$ vs. T (inset to the figure). When fitted at $T > T_N$ to a CW-law, $m^{\text{FC}} = (C/(T - \theta_c))\mu_0 H$ (solid line), it yields $\theta_c = 2$ K. On the other hand, $1/m^{\text{FC}}$ vs. T data shown in the inset of Fig. 6.5 when fitted similarly (solid line) yields $\theta_c = -9$ K. Obviously in the FC process of Fig. 6.4 starting from a premagnetized state, the blocked Fe granules convert a larger surrounding into an FM one by virtue of enhanced dipolar field strength.

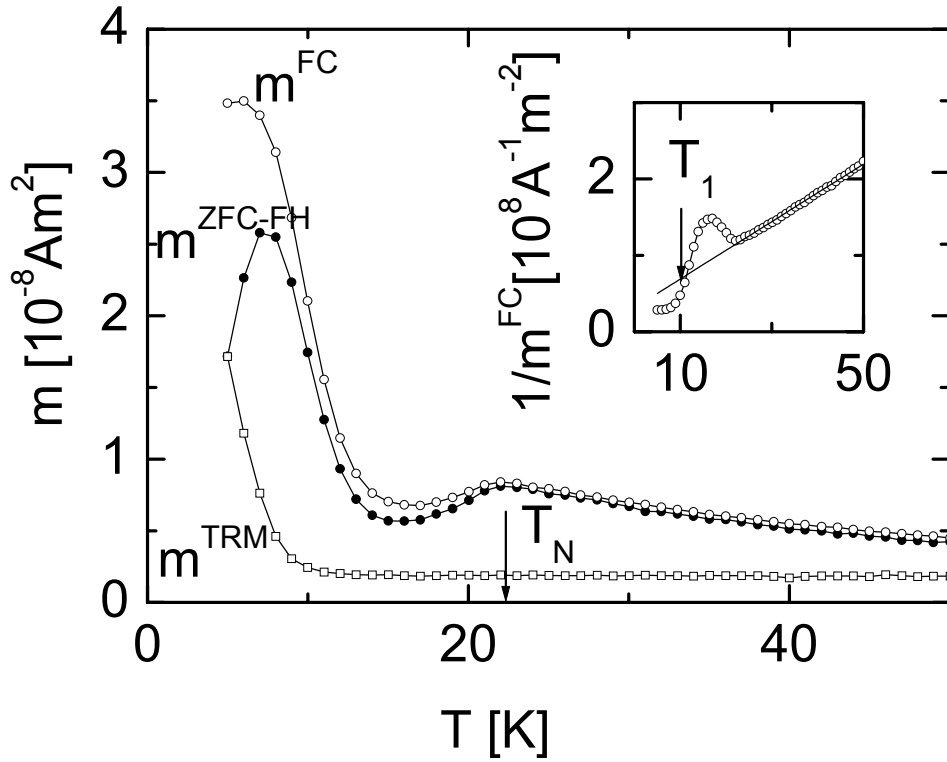


FIG. 6.5. $m^{\text{ZFC-FH}}$, m^{FC} , and m^{TRM} vs. T involving an external field $\mu_0 H = 10$ mT after a demagnetization procedure at $T = 290$ K. The inset shows $1/m^{\text{FC}}$ vs. T and Curie-Weiss-type fit (straight line).

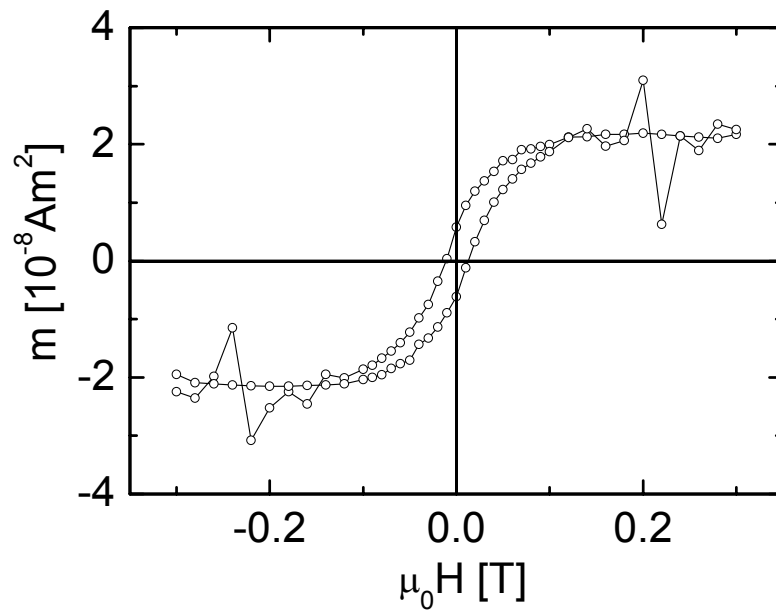


FIG. 6.6. m vs. $\mu_0 H$ loop at $T = 50$ K.

Comparison of $m^{\text{FC}}(T = 5 \text{ K})$ with the saturation moment of the magnetization hysteresis at $T = 50 \text{ K} > T_N$ (Fig. 6.6) shows that the total moment of the Fe granules is smaller approximately by a factor of three (Fig. 6.4) or two (Fig. 6.5) in order to explain its magnitude. These factors grow up to twelve (Fig. 6.4) and seven (Fig. 6.5), respectively, when comparing the remanence of the Fe granules (Fig. 6.6) retained in the weak-field FC process with the low- T moments. Their origin, obviously, hints at an enhancement of the FM polarization by virtue of the AF matrix. Tentatively, we suggest the enhancement of the FM polarization within a model of “dressed” Fe granules [124]. A polarization cloud is proposed to originate from FM exchange interaction between the spins of the field aligned Fe granules and the effective $S = 1$ spins of the Fe^{2+} -ions of the AF- FeCl_2 matrix. Since in FeCl_2 the inter-layer AF coupling ($J'/k_B = -0.18 \text{ K}$) between Fe^{2+} ions is approximately twenty times weaker than the intra-layer FM coupling ($J_1/k_B = 3.9 \text{ K}$) times, a direct exchange mechanism is suggested to be a relevant and reasonable assumption. In addition, the Fe-granules behave like magnetic dipoles. Considering the Fe granule as a uniformly magnetized sphere of radius r , the strength of the dipolar field at a point along the polar axis at a distance r' from its center is given by [5,7]

$$H = \frac{1}{4\pi\mu_0} \frac{2\mu}{r'^3} = \frac{1}{4\pi\mu_0} \frac{2M_s V}{r'^3} = \frac{2}{3} \frac{1}{\mu_0} \frac{M_s}{\left(\frac{r'}{r}\right)^3}, \quad (6.2)$$

where $\mu = M_s V$ is the magnetic moment of the Fe granule, M_s the bulk saturation magnetization, and V the volume of the granule. Using $M_s = 2.15 \text{ T}$ [7], and $D_{\text{Fe}} = 16 \text{ nm}$ the strength of the dipolar field at the pole ($r = r'$) will be 1.42 T. Thus, the stray field in the vicinity of the poles exceeds the spin-flip field which is $\mu_0 H_{\text{SF}} = 1.06 \text{ T}$ at $T = 4.2 \text{ K}$ [125]. Moreover, at the poles the stray-field is nearly parallel with respect to the magnetization of a given Fe granule. Hence, taking into account the preferential alignment of the granules along the freezing field, one expects a net FM polarization of the FeCl_2 matrix.

In Fig. 6.5, it is observed that m^{TRM} obeys the well known rule of Stoner and Wohlfarth [11] that the remanent magnetization becomes $m^{\text{TRM}}(T = 5 \text{ K}) = m_s/2$, where $m_s = m^{\text{FC}}(T = 5 \text{ K})$ is the saturation value. Obviously also the “dressed” moments reorient onto the field-selected hemisphere in the same way as the bare SW particles are used to do [11]. Furthermore, m^{TRM} in both Figs. 6.4 and 6.5 decays rapidly to an almost constant value at $T > T_1$, referring to the remanence of the bare Fe nanoparticles. Obviously the lacking alignment of the Fe moments causes a destabilization of the metamagnetic

coating at temperatures way below T_N . This is primarily due to the strong dependence of the spin-flip transition on the field orientation.

Further understanding on the stabilization of “dressed” moments can be extracted from two very useful quantities: $l = dm^{\text{TRM}}/dT$ and $k = d\Delta m/dT$, where $\Delta m = m^{\text{ZFC-FH}} - m^{\text{FC}}$. Both l and k exhibit almost similar trends with temperature as displayed in Fig. 6.7. When the temperature variations of Δm is compared to that of m^{TRM} (inset to Fig. 6.7) it is found that they exhibit almost identical behavior at $T < T_1$. Linear extrapolations of the low temperature parts of l and k with the T -axis yield points of intersections close to T_1 . Since Δm is a measure of the contribution of the polarized AF matrix and m^{TRM} achieves a constant value at $T > T_1$, these features indicate that the AF matrix stabilizes the “dressed” moments at $T < T_1$, where the dipolar field exceeds the spin-flip field of the AF matrix. Thermal disorder above T_1 randomizes the FM polarization and m^{TRM} attains the constant value of bare Fe granules.

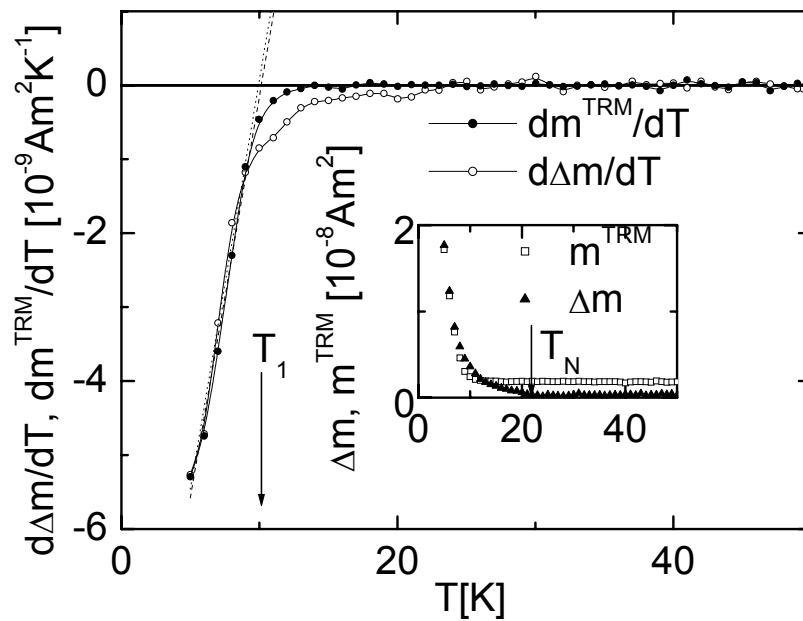


FIG. 6.7. dm^{TRM}/dT and $d\Delta m/dT$ vs. T , where $m = m^{\text{FC}} - m^{\text{ZFC-FH}}$. The inset shows Δm and m^{TRM} vs. T .

Subsequent FC magnetization cycles further corroborate the above conjectured growth of the FM granules. To this end we measured m^{FC} in iterative cooling and heating cycles at constant $\mu_0 H = 10$ mT within $5 \leq T \leq 290$ K as shown in Fig. 6.8. It is seen that

the FC-magnetization is reproducible down to $T = 20$ K, below which it shows an abrupt increase. In subsequent cycles the slope increases until the magnetization at $T = 5$ K approaches a constant value after the fourth cycle. Since the strength of the stray-field is proportional to the magnetic moment of the granule, the growth of granules is accompanied by increasing the stray-fields. On the other hand, a cut-off radius of the granules is finally determined by thermal disorder.

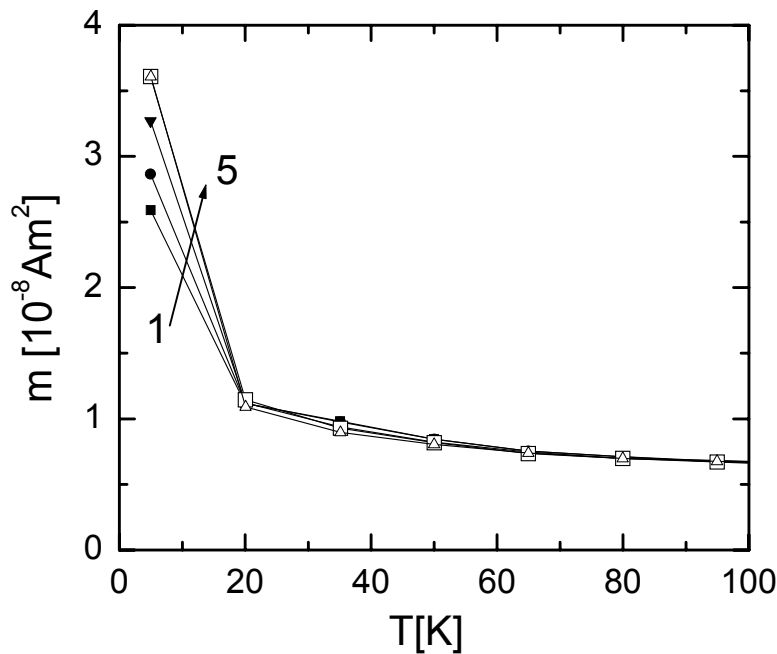


FIG. 6.8. m^{FC} vs. T in iterative cooling and heating cycles keeping the applied field constant at $\mu_0 H = 10$ mT. The arrow indicates the sequence of cycles.

Figure 6.9 presents the magnetic moment m vs. $\mu_0 H$ loops measured at $T = 50$, 15, and 5 K, i.e., above and below the Néel temperature, in the field range $-0.3 \leq \mu_0 H \leq 0.3$ T after ZFC from $T = 350$ K $> T_b$. At $T = 50$ K the finite remanence and coercivity are reminiscent of the hysteretic behavior of blocked Fe granules which are unaffected by the paramagnetic FeCl₂ matrix. At $T < T_N$ the magnitude of the magnetization increases by one order of magnitude, although the applied fields are insufficient to cause a spin-flip

transition of the FeCl_2 matrix ($\mu_0 H_{\text{SF}} = 1.06$ T). This underlines the conjectured growth of dressed granules by virtue of the exchange and dipolar interaction with the AF matrix.

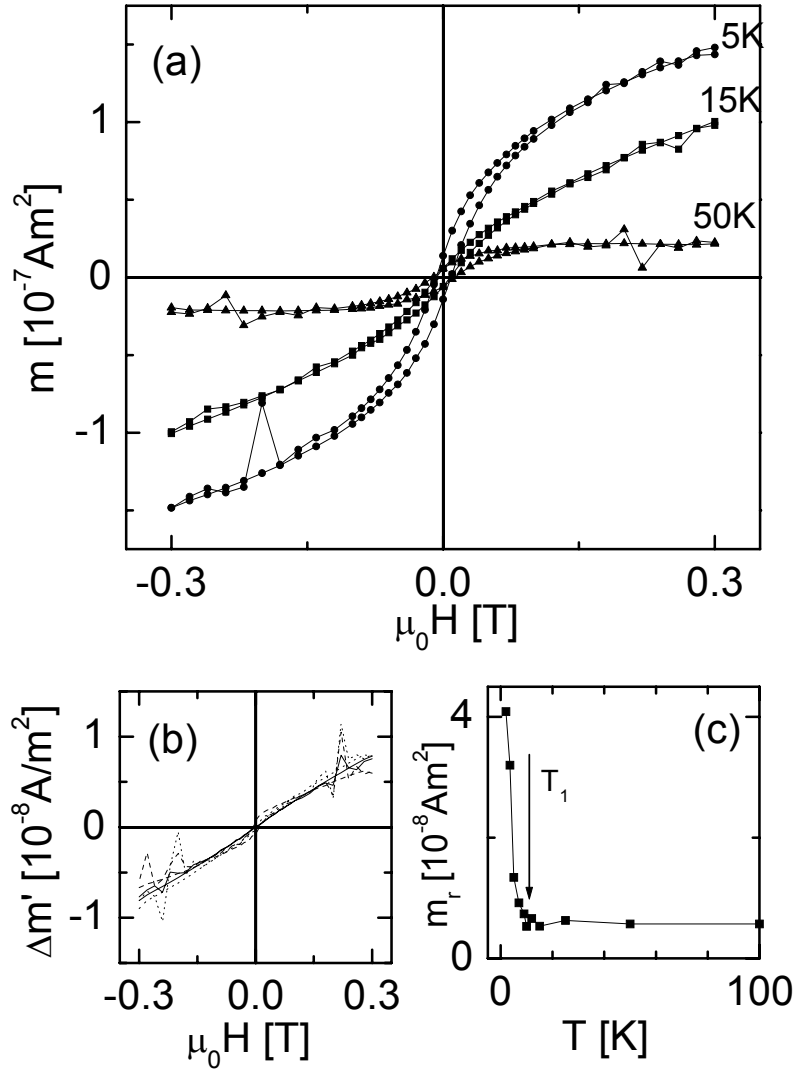


FIG. 6.9. m vs. $\mu_0 H$ loops at some selected temperatures. The lower inset shows the remanent magnetization m_r vs. T and T_1 by an arrow. The upper inset shows $\Delta m'$ vs. applied magnetic field at the same temperatures as m vs. $\mu_0 H$ loops shown in the main panel.

It is remarked that there is a qualitative difference between the loops above and below T_1 , where Fe granules become “dressed”. In the upper inset, we show the difference between the magnetic moment at low temperatures and the scaled reference curve $m(H, T = 50\text{K})$, $\Delta m' = m(H, T) - \lambda(T) m(H, T = 50\text{K})$. $\lambda(T)$ is a variable which is a

measure of the effective moment of the “dressed” Fe granule. When choosing $\lambda = 1, 2.2,$ and 3 at $T = 15, 10,$ and 5 K, respectively, a unique linear curve $\Delta m'(H)$ is obtained, which does not depend on the temperature [Fig. 6.9(b)]. This indicates that $\Delta m(H)$ originates from the perpendicular susceptibility χ_{\perp} of the AF matrix because the parallel susceptibility χ_{\parallel} is much smaller than χ_{\perp} far below T_N . On the other hand the increase of λ clearly reinforces the model assumption of the “dressed” Fe granules, which are estimated to grow in size by about 40% when cooling from $T = 15$ K to 5 K. In accordance with observed increase of λ the temperature variation of the remanent magnetization, m_r , shown in Fig. 6.9(c) reveals a steep rise below T_1 .

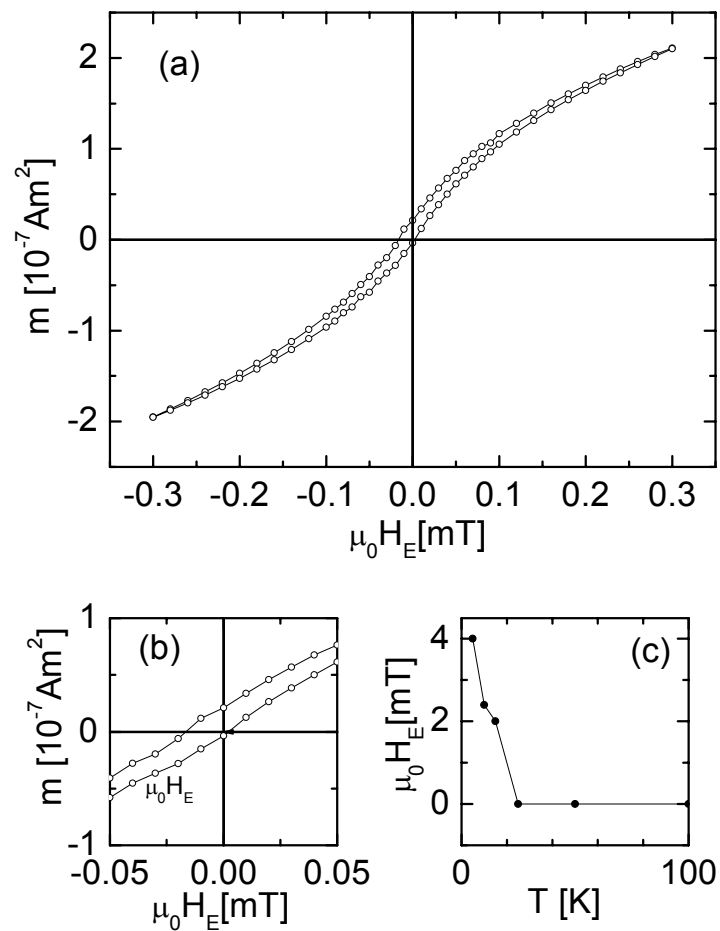


FIG. 6.10. (a) m vs. $\mu_0 H$ loop at $T = 5$ K after cooling in a field of $\mu_0 H = 0.1$ T. (b) Magnified portion of the loop with the exchange bias field $\mu_0 H_E$ indicated by an arrow. (c) $\mu_0 H_E$ vs. T .

Figure 6.10 shows the m vs. $\mu_0 H$ loop at $T = 5$ K after cooling the sample from $T = 350$ K in a field of $\mu_0 H = 0.1$ T. The shift along the field axis by $\mu_0 H_E = -4$ mT [Fig. 6.10 (b)] is the fingerprint of exchange bias (EB) due to exchange coupling at the FM-AF interface. During field-cooling, an excess moment is stored in the disorderly frozen-in AF domains at the interface to the single-domained FM core (see below). When the field is removed, the FM core experiences the field generated by the frozen-in interface moment in the direction of the previously applied field, thus generating the loop shift. Earlier observations have reported significant EB effects in ferrimagnetic Fe_2O_3 [126] and nanoscale granular Fe/FeO systems [127] due to strong exchange anisotropy which has been claimed in all these cases to originate at the interface of a possible FM core and a frozen-in surface spin-glasslike layer similar to the present one. Figure 6.10 (c) shows the temperature dependence of the exchange bias field $\mu_0 H_E$. As expected the blocking temperature of $\mu_0 H_E$ does not exceed the Néel temperature of the AF matrix.

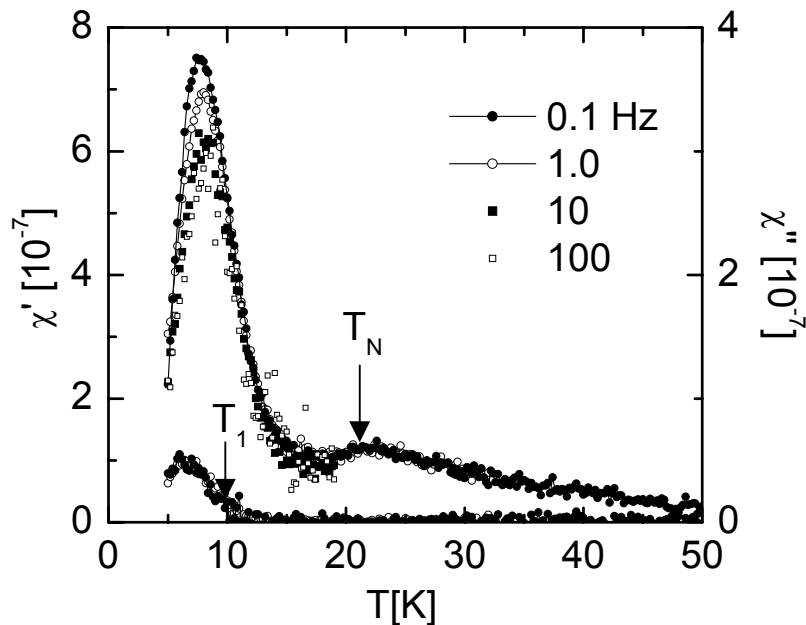


FIG. 6.11. Temperature variation of ac-susceptibility at $\mu_0 H_{ac} = 0.4$ mT and $0.1 \leq f \leq 100$ Hz.

In order to clarify the nature of the low temperature properties, ac-susceptibility measurements were performed following a demagnetization procedure at $T = 290$ K. An

ac-amplitude of $\mu_0 H_{ac} = 0.4$ mT and frequencies in the range $0.1 \leq f \leq 100$ Hz were employed. In Fig. 6.11, temperature variation of the real part, χ' , of ac-susceptibility data show two distinct peaks in much the same way as $m^{\text{ZFC-FH}}$ vs. T in Fig. 6.5. The frequency independent peak at $T_N \approx 22$ K characterizes the AF feature. The pronounced lower temperature peak, again, clearly signifies local FM transformation of the AF environment. Its frequency dependence and a concomitant appearance of an imaginary component, χ'' , at $T_1 \approx 10$ K hint at a very slow dynamics in the system. On this basis, the lower temperature state, i.e. at $T < T_1$, of our FM-AF system can be pictured as constituted by an ensemble of two different components. The first, a FM one, obviously consists of giant metamagnetic moments with blocked Fe-cores, while the second one is probably a disorderly frozen surface spin layer around each “dressed” granule. Since the blocking of the Fe moments occurs at very high temperature, $T = 320$ K, the “dressed” granule can virtually be considered as a moment distribution with ellipsoidal shape, elongated along the local anisotropy axis ($\mu_0 H = 0$) or along the field ($\mu_0 H \neq 0$), whereas the relaxation processes are associated with frozen-in surface spin layers. Recalling the aforementioned exchange mechanism of “dressed” granules, the slow dynamics of the mobile surface spins is tentatively attributed to the occurrence of AF domains with excess wall magnetization similarly as observed on a planar FeCl₂/CoPt heterostructure with a rough interface [128].

6.4. Conclusion

In summary, we have studied the structural and magnetic properties of Fe granules embedded in a FeCl₂ matrix and have shown that significant variations of their properties occur below the AF ordering temperature due the presence of strong particle-matrix interaction. We have demonstrated that giant moments of “dressed” Fe granules are formed below T_N and that they grow in repeated field-cooled cycles. The observations can be explained by assuming both exchange and dipolar coupling between the granules and the matrix within a model of dressed granules.

Chapter 7

Summary and Outlook

The macroscopic behavior of nanostructured magnetic systems is determined by the structure, size, and morphology of the constituent materials and by the type and strength of magnetic coupling between them. In this work, the properties of two different magnetic systems have experimentally been investigated. The first system was prepared as a discontinuous-metal-insulator multilayer (DMIM) $[\text{Co}_{80}\text{Fe}_{20}(t_n)/\text{Al}_2\text{O}_3(3\text{ nm})]_{10}$. Structural studies performed on a bilayer system $\text{CoFe}(t_n=0.9\text{ nm})/\text{Al}_2\text{O}_3(3\text{ nm})$ reveals that the CoFe forms well-separated and quasi-spherical granules in the Al_2O_3 matrix. Comparison with the studies performed on a system with increasing $t_n = 1.3\text{ nm}$ shows that the size of the granules increases while the interparticle distance decreases with t_n . A systematic structural characterization within a range of t_n , e.g., $0.5 \leq t_n \leq 1.8\text{ nm}$ is further needed to gain complete knowledge of the growth kinetics as well as structural information of the nanoparticles.

The DMIMs investigated in this thesis can be considered to consist of an ensemble of ferromagnetic nanoparticles embedded in an insulating (diamagnetic) matrix. When investigating the magnetic properties the nanoparticle-matrix interaction has been neglected. It was found that the magnetic properties of the DMIMs strongly depend on t_n . Studies on a moderately dense nanoparticle system $[\text{Co}_{80}\text{Fe}_{20}(t_n)/\text{Al}_2\text{O}_3(3\text{ nm})]_{10}$ with $t_n = 0.9\text{ nm}$ have shown that the low temperature dynamics of the particle magnetic moments clearly deviates from Arrhenius-Néel-Brown-type behavior. On the contrary strong evidences have been found for a collective dynamics. This was attributed to a superspin glass phase. Most of the typical features of non-equilibrium collective dynamics were observed in this phase. It will be interesting to check, if such properties can be observed in the corresponding single-layered nanoparticle systems. They can be considered as 2D-like systems, where a vanishing glass transition temperature is expected. Similar studies on more diluted samples, e.g., $t_n = 0.5$ and 0.7 nm need to be carried out and the results have to be compared with the present ones. Within this framework the crossover behavior from single particle dynamics to a collective one can be studied.

Furthermore, studies on relatively dense nanoparticle DMIM systems with $t_n = 1.3$ and 1.4 nm reveal some characteristics of a superferromagnetic state. A systematic investigation has still to be accomplished in order to understand its exact nature and its very origin. This will be of some relevance for the development of nanoscaled magnetic storage devices on the basis of densely packed single domain particles. The occurrence of superferromagnetism then risks to disable, e.g., the individual addressing of magnetic dots in the future terabit storage devices, which are presently under consideration [63].

The second system consists of ferromagnetic Fe nanoparticles embedded in a soft antiferromagnetic FeCl_2 matrix. The system was prepared as a granular FeCl_2 -Fe heterostructure. In this case it was found that the nanoparticle-matrix interaction plays an important role in determining the magnetic behavior below the AF ordering temperature. Owing to weak intra-matrix antiferromagnetic exchange coupling as compared to the interaction at the nanoparticle-matrix interface giant moments are observed. As an outlook to future work it is worth mentioning that doping of an AF matrix with FM nanoparticles may also be used to tailor the transport properties, viz. to create devices with exchange-biased asymmetric tunnel magnetoresistance.

References

- [1] G. Prince and K. Hathaway, *Physics Today* **48** (4), 24 (1995).
- [2] F. J. Himpsel, J. E. Ortega, G. J. Mankey, and R. F. Willis, *Advances in Physics* **47**, 511 (1998).
- [3] P. Grünberg, *Physics Today* **54** (5), 31 (2001).
- [4] J. I. Martin, J. Nogues, Kai Liu, J. L. Vincent, and I. K. Schuller, *J. Magn. Magn. Mater.* **256**, 449 (2002).
- [5] B. D. Cullity, *Introduction to Magnetic Materials* (Addison-Wesley, Menlo Park, California, 1972).
- [6] A. Hubert and R. Schäfer, *Magnetic Domains* (Springer-Verlag, Berlin, 1998).
- [7] S. Chikazumi, *Physics of Ferromagnetism* (Oxford University Press, New York, 1999).
- [8] R. P. Cowburn, *Science* **287**, 1466 (2000).
- [9] P. Weiss, *J. de Phys. Rad.* **6**, 661 (1907).
- [10] D. Givord, Q. Lu, and M. F. Rosignol, in *Science and Technology of Nanostructured Materials*, Edited by G. C. Hadjipanayis and G. A. Prinz (Plenum, New York, 1991) p. 635.
- [11] E. C. Stoner and E. P. Wohlfarth, *Philos. Trans. London Ser. A* **240**, 599 (1948).
- [12] L. Néel, *Ann. Geophys.* **5**, 99 (1949).
- [13] W. F. Brown, Jr., *Phys. Rev.* **130**, 1677 (1963).
- [14] D. Hinzke, U. Nowak, and K. D. Usadel, in *Structure and Dynamics of Heterogeneous Systems*, Edited by P. Entel and D. E. Wolf (World Scientific, Singapore, 2000).
- [15] J. L. Dormann, D. Fiorani, and E. Tronc, *Adv. Chem. Phys.* **98**, 283 (1997).
- [16] A. Aharoni, *Introduction to the Theory of Ferromagnetism* (Oxford University Press, New York, 2000).
- [17] W. T. Coffey, Yu. P. Kalmykov, and J. T. Waldron, *The Langevin Equation* (World Scientific, Singapore, 1996).
- [18] M. R. Scheinfein, K. E. Schmidt, K. R. Heim, and G. G. Hembree, *Phys. Rev. Lett.* **76**, 1541 (1996).
- [19] P. Bruno, *Phys. Rev. Lett.* **88**, 240401 (2002).
- [20] R. V. Chamberlin, J. Hemberger, A. Loidl, K. D. Humfeld, D. Farrell, S. Yamamuro, Y. Ijiri, and S. A. Majetich, *Phys. Rev. B* **66**, 172403 (2002).

- [21] T. Jonsson, J. Mattsson, C. Djurberg, F. A. Khan, P. Nordblad, and P. Svedlindh, *Phys. Rev. Lett.* **75**, 4138 (1995).
- [22] H. Mamiya, I. Nakatani, and T. Furubayashi, *Phys. Rev. Lett.* **82**, 4332 (1999).
- [23] J. L. Dormann, R. Cherkaoui, L. Spinu, M. Noguès, F. Lucari, F. D’Orazio, D. Fiorani, A. Garcia, E. Tronc, and J. P. Jolivet, *J. Magn. Magn. Mater.* **187**, L139 (1998).
- [24] W. Kleemann, O. Petravic, Ch. Binek, G. N. Kakazei, Yu. G. Pogorelov, J. B. Sousa, S. Cardoso, and P. P. Freitas, *Phys. Rev. B* **63**, 134423 (2001).
- [25] X. Chen, O. Sichelshmidt, W. Kleemann, O. Petravic, Ch. Binek, J. B. Sousa, S. Cardoso, and P. P. Freitas, *Phys. Rev. Lett.* **89**, 137203 (2002).
- [26] P. Politi and M. G. Pini, *Phys. Rev. B* **66**, 214414 (2002).
- [27] S. Strikmann and E. P. Wohlfarth, *Phys. Lett. A* **85**, 467 (1981).
- [28] S. Mørup and E. Tronc, *Phys. Rev. Lett.* **72**, 3278 (1994).
- [29] S. Mørup, *Europhys. Lett.* **28**, 671 (1994).
- [30] O. Petravic, W. Kleemann, Ch. Binek, G. N. Kakazei, Yu. G. Pogorelov, J. B. Sousa, S. Cardoso, and P. P. Freitas, *Phase Transitions* **75**, 73 (2002).
- [31] S. Sahoo, O. Petravic, Ch. Binek, W. Kleemann, J. B. Sousa, S. Cardoso, and P. P. Freitas, *Phys. Rev. B* **65**, 134406 (2002).
- [32] D. Kechrakos and K. N. Trohidou, *Phys. Rev. B* **58**, 12169 (1998).
- [33] R. W. Chantrell, N. Walmsey, J. Gore, and M. Maylin, *Phys. Rev. B* **63**, 024410 (2000).
- [34] A. Lyberatos and E. P. Wohlfarth, *J. Magn. Magn. Mater.* **59**, L1 (1986).
- [35] M. El-Hilo, R. W. Chantrell, and O’Grady, *J. Appl. Phys.* **81**, 5582 (1997).
- [36] J. G. Zhu and H. N. Bertram, *J. Appl. Phys.* **63**, 3248 (1988).
- [37] M. Ulrich, J. Garcia-Otero, J. Rivas, and A. Bunde, *Phys. Rev. B* **67**, 024416 (2003).
- [38] J. O. Andersson, T. Jonsson and J. Mattsson, *Phys. Rev. B* **54**, 9912 (1996).
- [39] W. Heisenberg, *Z. Phys.* **49**, 619 (1928).
- [40] S. F. Edwards and P. W. Anderson, *J. Phys. F* **5**, 965 (1975).
- [41] K. Fisher and J. A. Hertz, in *Spin Glasses*, Edited by D. Edwards and D. Melville (Cambridge University Press, Cambridge 1991).
- [42] J. A. Mydosh, *Spin Glasses: An Experimental Introduction* (Taylor and Francis, London, 1993).

- [43] H. E. Stanley, *Introduction to Phase Transitions and Critical Phenomena* (Oxford University Press, New York, 1972).
- [44] S. K. Ma, *Modern Theory of Critical Phenomena* (Addison-Wesley Publishing, New York, 1976).
- [45] M. Suzuki, *Pro. Theor. Phys.* **58**, 1151 (1977).
- [46] K. Gunnarsson, P. Svedlindh, P. Nordblad, L. Lundgren, H. Aruga, and A. Ito, *Phys. Rev. Lett.* **61**, 75 (1988).
- [47] D. Sherrington and S. Kirkpatrick, *Phys. Rev. Lett.* **35**, 1792 (1975).
- [48] G. Parisi, *Phys. Rev. Lett.* **43**, 1754 (1979).
- [49] M. Mezard, G. Parisi, M. A. Virasoro, *Spin Glass Theory and Beyond*, in *Lecture Notes in Physics, Vol. 9* (World Scientific, Singapore, 1987).
- [50] D. S. Fisher and D. A. Huse, *Phys. Rev. Lett.* **56**, 1601 (1986).
- [51] D. S. Fisher and D. A. Huse, *Phys. Rev. B* **38**, 373 (1988); **38**, 386 (1988).
- [52] D. S. Fisher, G. M. Grinstein, and A. Khurana, *Physics Today* **41**, 56 (1988).
- [53] P. E. Jönsson, H. Yoshino, P. Nordblad, H. Aruga Katori, and A. Ito, *Phys. Rev. Lett.* **88**, 252704 (2002).
- [54] K. Jonason, E. Vincent, J. Hammann, J.-P. Bouchaud, and P. Nordblad, *Phys. Rev. Lett.* **81**, 3243 (1998).
- [55] A. J. Bray and M. A. Moore, *Phys. Rev. Lett.* **58**, 57 (1987).
- [56] M. F. Collins and J. B. Forsyth, *Phil. Mag.* **8**, 401 (1963).
- [57] D. I. Bardos, *J. Appl. Phys.* **40**, 1371 (1969).
- [58] Landolt-Börnstein, *New Series III/19a* (Springer, Berlin, 1987) p. 210.
- [59] J. Kortus, T. Baruah, M. R. Pederson, C. Ashman, and S. N. Khanna, *Appl. Phys. Lett.* **80**, 4193 (2002).
- [60] R. W. G. Wyckoff, *Crystal Structure* (R. E. Krieger Publishing Company, Malabar, 1982), p. 271.
- [61] R. J. Birgeneau, W. B. Yelon, E. Cohen, and J. Makovsky, *Phys. Rev. B* **5**, 2607 (1972).
- [62] Ch. Binek, *Dissertation*, Gerhard-Mercator-Universität Duisburg (1995).
- [63] S. Sun, C. B. Murray, D. Weller, L. Folks, and A. Moser, *Science* **287**, 17 (2000).
- [64] C. T. Black, C. B. Murray, R. L. Sandstrom, and S. Sun, *Science* **290**, 1131 (2000).
- [65] Ch. Morawe and H. Zabel, *J. Appl. Phys.* **77**, 1969 (1995).
- [66] S. Sankar, B. Dieny, and A. E. Berkowitz, *J. Appl. Phys.* **81**, 5512 (1997).
- [67] S. Sankar, A. E. Berkowitz, and D. J. Smith, *Appl. Phys. Lett.* **73**, 535 (1998).

- [68] J.-L. Maurice, J. Briático, J. Carrey, F. Petroff, L. F. Schelp, and A. Vaurès, *Phil. Mag. A* **97**, 2921 (1999).
- [69] G. N. Kakazei, Yu. G. Pogorelov, A. M. L. Lopes, J. B. Sousa, S. Cardoso, P. P. Freitas, M. M. Pereira de Azevedo, and E. Snoeck, *J. Appl. Phys.* **90**, 4044 (2001).
- [70] Z. Gai, B. Wu, J. P. Pierce, G. A. Farnan, D. Shu, M. Wang, Z. Zhang, and J. Shen, *Phys. Rev. Lett.* **89**, 235502 (2002).
- [71] R. P. Cowburn, D. K. Koltsov, A. O. Adeyeye, and M. E. Welland, *Europhys. Lett.* **48** (2), 221 (1999).
- [72] S. Cardoso, V. Gehanno, R. Ferreira, and P. P. Freitas, *IEEE Trans. Magn.*, **35** (5), 2952 (1999).
- [73] S. Sahoo, O. Petravic, W. Kleemann, S. Stappert, G. Dumpich, P. Nordblad, S. Cardoso, and P. P. Freitas, *Appl. Phys. Lett.* **82**, 4116 (2003).
- [74] W. Kleemann and B. Hendel, *J. Magn. Magn. Mater.* **31-34**, 581 (1983).
- [75] L. Reimer, *Transmission Electron Microscopy*, (*Springer Series in Optical Sciences, Vol. 34*), Ed. D. L. MacAdam, Springer-Verlag, Berlin (1984).
- [76] B. D. Cullity and S. R. Stock, *Elements of X-ray diffraction* (Prentice Hall, New Jersey, 2001).
- [77] W. Buckel, *Superconductivity: Fundamentals and Applications* VCH, Weinheim (1994).
- [78] J. E. C. Williams, *Superconductivity and its applications* (Pion Limited, London, 1970).
- [79] Hand book, SQUID magnetometer MPMS – 5S, Quantum Design, San Diego (1993).
- [80] J. Magnusson, C. Djurberg, P. Granberg, and P. Nordblad, *Rev. Sci. Instrum.* **68**, 3761 (1997).
- [81] Hand book, Ultra-Low Field Option, Quantum Design, San Diego (2002).
- [82] W. H. Meiklejohn and C. P. Bean, *Phys. Rev.* **105**, 904 (1956).
- [83] C. Djurberg, P. Svedlindh, P. Nordblad, M. F. Hansen, F. Bødker, and S. Mørup, *Phys. Rev. Lett.* **79**, 5154 (1997).
- [84] T. Jonsson, P. Svedlindh, and M. F. Hansen, *Phys. Rev. Lett.* **81**, 3976 (1998).
- [85] M. F. Hansen, P. E. Jönsson, P. Nordblad, and P. Svedlindh, *J. Phys.: Condens. Matter.* **14**, 4901 (2002).
- [86] H. Maletta and W. Felsch, *Phys. Rev. B* **20**, 1245 (1979).

- [87] P. Jönsson, M. F. Hansen, P. Svedlindh, and P. Nordblad, *J. Magn. Magn. Mater.* **226-230**, 1315 (2001).
- [88] K. Gunnarsson, P. Svedlindh, P. Nordblad, L. Lundgren, H. Aruga, and A. Ito, *Phys. Rev. B.* **43**, 8199 (1991).
- [89] K. Cole, and R. Cole, *J. Chem. Phys.* **9**, 341 (1941).
- [90] A. Jonscher, in *Dielectric relaxation in solids* (Chelsea Dielectrics Press, London, 1993).
- [91] O. Petravic, S. Sahoo, Ch. Binek, W. Kleemann, J. B. Sousa, S. Cardoso, and P. P. Freitas, *Phase Transitions* **77**, 367 (2003).
- [92] M. Hagiwara, *J. Magn. Magn. Mater.* **177-181**, 89 (1998).
- [93] L. Lundgren, P. Svedlindh, P. Nordblad, and O. Beckmann, *Phys. Rev. Lett.* **51**, 911 (1983).
- [94] S. Sahoo, O. Petravic, W. Kleemann, P. Nordblad, S. Cardoso, and P. P. Freitas, *Phys. Rev. B* **67**, 214422 (2003).
- [95] V. Dupuis, E. Vincent, J.-P. Bouchaud, J. Hammann, A. Ito, and H. A. Katori, *Phys. Rev. B* **64**, 174204 (2001).
- [96] R. Mathieu, P. E. Jönsson, P. Nordblad, H. A. Katori, and A. Ito, *Phys. Rev. B* **65**, 012411 (2001).
- [97] S. Sahoo, O. Petravic, W. Kleemann, P. Nordblad, S. Cardoso, and P. P. Freitas, *Proc. Int. Conf. Magn. ICM-2003, Rome, Italy*; *J. Magn. Magn. Mater.* (submitted).
- [98] L. Berthier and J.-P. Bouchaud, *Phys. Rev. B* **66**, 054404 (2002).
- [99] S. Sahoo, O. Petravic, Ch. Binek, W. Kleemann, J. B. Sousa, S. Cardoso, and P. P. Freitas, *J. Phys.: Condens. Matt.* **14**, 6729 (2002).
- [100] J. Hammann, M. Lederman, M. Ocio, R. Orbach, and E. Vincent, *Physica* **185 A** 278 (1992); E. Vincent, J.-P. Bouchaud, J. Hammann, and F. Lefloch, *Philos. Mag. B* **71**, 647 (1995).
- [101] P. Nordblad and P. Svedlindh in *Spin Glasses and Random Fields (Series on Directions in Condensed Matter Physics, Vol12)*, Edited by A P Young (World Scientific, Singapore, 1997) p 24.
- [102] F. Lefloch, J. Hammann, M. Ocio, and E. Vincent, *Europhys. Lett.* **18**, 647 (1992).
- [103] J. Mattsson, T. Jonsson, P. Nordblad, H. Aruga Katori, and A. Ito, *Phys. Rev. Lett.* **74**, 4305 (1995).
- [104] E. Marinari, G. Parisi, and F. Zuliani, *Phys. Rev. Lett.* **84**, 1056 (2000).

- [105] J. R. L. de Almeida and D. J. Thouless, *J. Phys.* **A11**, 983 (1978).
- [106] M. Gabay and G. Toulouse, *Phys. Rev. Lett.* **47**, 201 (1981).
- [107] G. G. Kenning, D. Chu, and R. Orbach, *Phys. Rev. Lett.* **66**, 2923 (1991).
- [108] D. Petit, L. Fruchter, and I. A. Campbell, *Phys. Rev. Lett.* **83**, 5130 (1999).
- [109] H. Aruga Katori and A. Ito, *J. Phys. Soc. Jpn.* **63**, 2122 (1994).
- [110] F. Krzakala, J. Houdayer, E. Marinari, O. C. Martin, and G. Parisi, *Phys. Rev. Lett.* **87**, 197204 (2001).
- [111] H. Kawamura and D. Imagawa, *Phys. Rev. Lett.* **87**, 207203 (2001).
- [112] H. Sompolinsky, *Phys. Rev. Lett.* **47**, 935 (1981).
- [113] K. Miyoshi, Y. Nishimura, K. Honda, K. Fujiwara, and J. Takeuchi, *J. Phys. Soc. Jpn.* **69** (11), 3517 (2000).
- [114] S. Sahoo, O. Sichelschmidt, O. Petravic, Ch. Binek, W. Kleemann, G. N. Kakazei, Yu. G. Pogorelov, J. B. Sousa, S. Cardoso, and P. P. Freitas, *J. Magn. Magn. Mater.* **240**, 433 (2002).
- [115] J. Villain, *Z. Phys. B* **33**, 31 (1979); C. L. Henley, *Phys. Rev. Lett.* **62**, 2056 (1989).
- [116] V. N. Kondratyev and H. O. Lutz, *Phys. Rev. Lett.* **81**, 4508 (1998).
- [117] O. Sichelschmidt, *Diplomarbeit*, Gerhard-Mercator-Universität Duisburg (2002).
- [118] T. Nattermann, Y. Shapir, and I. Vilfan, *Phys. Rev. B* **42**, 8577 (1990).
- [119] M. Avrami, *J. Chem. Phys.* **7**, 1103 (1939); E. Fatuzzo, *Phys. Rev.* **127**, 1999 (1962).
- [120] T. Nattermann, V. Pokrovsky, and V. M. Vinokur, *Phys. Rev. Lett.* **87**, 197005 (2001)
- [121] J. Nogués and I. K. Schuller, *J. Magn. Magn. Mater.* **180**, 100 (1999).
- [122] F. Nolting, A. Scholl, J. Stohr, J. W. Seo, J. Fompeyrine, H. Siegwart, J.-P. Locquet, S. Anders, J. Luning, E. E. Fullerton, M. F. Toney, M. R. Scheinfein, and H. A. Padmore, *Nature* **405**, 767 (2000).
- [123] S. Sahoo, Ch. Binek, and W. Kleemann, *Phase Transitions*, (submitted).
- [124] S. Sahoo, Ch. Binek, and W. Kleemann, *Phys. Rev. B*, (submitted).
- [125] I. S. Jacobs and P. E. Lawrence, *Phys. Rev.* **164**, 866 (1963).
- [126] B. Martinez, X. Obradors, Ll. Balcells, A. Rouanet, and C. Monty, *Phys. Rev. Lett.* **80**, 181 (1998).
- [127] L. Del Bianco, D. Fiorani, A. M. Testa, Bonetti, L. Savini, and S. Signoretti, *Phys. Rev. B* **66**, 174418 (2002).
- [128] Ch. Binek, A. Hochstrat, and W. Kleemann, *Phys. Stat. Sol. (a)* **189**, 575 (2002).

Acknowledgments

It is my unique pleasure to thank my thesis advisor Prof. Dr. Wolfgang Kleemann for his extensive guidance, continuous encouragement and support throughout this work. I appreciate all the hours spent in stimulating discussions and his valuable suggestions and advice.

I am grateful to the selection committee for accepting me as a PhD student to the Graduiertenkolleg "Struktur and Dynamik Heterogener Systeme" DFG – GK 277. I am grateful for the financial support.

I would like to thank all members of the research group of Prof. Kleemann and in particular Priv.-Doz. Dr. Christian Binek, Dr. Oleg Petravic, Dipl.-Ing. Manfred Aderholz, Dr. Xi Chen, Dipl.-Phys. Andreas Hochstrat for distinct helpfulness and for creating an enjoyable working atmosphere.

I am indebted to Prof. João Bessa Sousa at IFIMUP, Universidade de Porto, Portugal for inviting me to join a German-Portuguese research project (DAAD-CRUP) on discontinuous magnetic multilayers and to Prof. Paulo Freitas and Dr. Susana Cardoso Freitas at INESC, Lisbon, Portugal for fruitful collaboration and sample preparation. Financial support of a visit to INESC, Lisbon, is gratefully acknowledge.

I would like to thank Prof. Per Nordblad at Uppsala University, Sweden for his supervision and fruitful collaboration and his group for the inspiring and pleasant time at Uppsala.

I would also like to thank Dipl.-Phys. Sonja Stappert and Prof. Günter Dumpich from the Experimentalphysik of our university for collaboration and in particular for the transmission electron microscopy.

I am grateful to Prof. Surjyo N. Behera, Vice-Chancellor, Berhampur University, Orissa, India for inspiring and recommending me to carry my research in Germany.

I am in debt to my family and relatives for their kind patience. I thank my wife for her love and support.